POLYPUBLIE

Experimental Protocols for Polymeric Binder Selection in the Binder Jetting of Metallic Particles in Three-Dimensional Printing

Sergio Ivan Yanez Sanchez

Document en libre accès dans PolyPublie
Open Access document in PolyPublie

Date	2021
Type	Mémoire ou thèse / Dissertation or Thesis Mémoire de maîtrise/Master's thesis
URL de PolyPublie PolyPublie URL	https://publications.polymtl.ca/6296/
Conditions d'utilisation Terms of use	© Tous droits réservés / All rights reserved
Référence Citation	Yanez Sanchez, S. I. (2021). Experimental Protocols for Polymeric Binder Selection in the Binder Jetting of Metallic Particles in Three-Dimensional Printing [Mémoire de maîtrise, Polytechnique Montréal]. PolyPublie. https://publications.polymtl.ca/6296/

Détails de la thèse
Thesis details

Directeurs de recherche Advisors	Daniel Therriault, Basil D. Favis, & Jason Robert Tavares
Programme Program	Génie chimique

Ce fichier a été téléchargé à partir de PolyPublie, le dépôt institutionnel de Polytechnique Montréal
This file has been downloaded from PolyPublie, the institutional repository of Polytechnique Montréal
https://publications.polymtl.ca

POLYTECHNIQUE MONTRÉAL

affiliée à l'Université de Montréal

Experimental Protocols for Polymeric Binder Selection in the Binder Jetting of Metallic Particles in Three-Dimensional Printing

SERGIO IVAN YANEZ SANCHEZ

Département de génie chimique

Mémoire présenté en vue de l'obtention du diplôme de *Maîtrise ès sciences appliquées*

Génie chimique

Avril 2021

© Sergio Ivan Yanez Sanchez, 2021.

POLYTECHNIQUE MONTRÉAL

affiliée à l'Université de Montréal

Ce mémoire intitulé :

Experimental Protocols for Polymeric Binder Selection in the Binder Jetting of Metallic Particles in Three-Dimensional Printing

présenté par **Sergio Ivan YANEZ SANCHEZ**

en vue de l'obtention du diplôme de *Maîtrise ès sciences appliquées*

a été dûment accepté par le jury d'examen constitué de :

Marie-Claude HEUZEY, présidente
Jason Robert TAVARES, membre et directeur de recherche
Basil FAVIS, membre et codirecteur de recherche
Daniel THERRIAULT, membre et codirecteur de recherche
Nick VIRGILIO, membre

DEDICATION

To my beloved family

ACKNOWLEDGEMENTS

First and foremost, I would like to express my gratitude to my director, Prof. Jason R. Tavares, and co-directors, Prof. Basil D. Favis and Prof. Daniel Therriault, for their continuous academic and moral support. I'm deeply grateful for their endless guidance, encouragement, and teachings.

I also wish to extend my gratitude to my teammates Alice Goffin, David Schlachter, Erik Daigle Dr. Somayeh Hosseini Rad and Dr. Martin Lennox for their valuable contributions to the project. Without them, this project wouldn't have been as enjoyable. Special thanks to Dr. Somayeh Hosseini Rad and Dr. Martin Lennox for their expert and exceptional advices. I would also like to extend a special acknowledgement to our industrial partners' representative, Noemie Laquerre, for her availability and her insightful suggestions.

I acknowledge Sautech, Kinova, NSERC, PRIMAQuébec, Polytechnique Montreal (UPIR undergraduate research grants) and CREPEC for their financial support. The realisation of this project was only possible thanks to their contributions.

I consider myself very fortunate to have counted with the help of all the amazing technical staff and research associates of the Department of Chemical Engineering of Polytechnique Montreal. Thanks to Martine Lamarche, Gino Robin, Sebastien Chénard, Matthieu Gauthier, and Wendell Raphaël for their availability and support.

Fortunately, the members of the PhotoSEL group are very united. Both present and past members, provided a pleasant environment in which I enjoyed working. Thank you all for your friendship.

Last but not least, I would like to thank my entire family for their endless love, encouragement and support. Specially, I thank my grandparents, Maria Victoria Martinez Carbajal, Rosario Campos Perez, Emiliano Salvador Sanchez Rodriguez and Jose Loreto Martinez Carbajal, for being a source of inspiration. I thank my parents, Xiomara Sanchez Martinez and Sergio Constantino Yanez Campos, for their unconditional support and for instilling in me the love for science. Finally, I thank my beloved Natacha Elisabeth Baez Ubal who stood by me during all my studies and has always believed in me.

RÉSUMÉ

L'impression par jets de liant est une technique avancée de fabrication à base de poudres où un lit de poudre, puis un liant polymérique sont déposées de manière alternée jusqu'à ce qu'une pièce à trois dimensions soit formée. La pièce résultante est appelée un corps vert. Elle est composée de particules de poudre tenues ensemble par le liant. Pour obtenir une pièce purement métallique, la pièce doit être traitée thermiquement pour pyrolyser le polymère et fritter les particules de poudre. C'est l'une des techniques d'impression 3D de métaux les plus prometteuses. Cependant, la sélection des liants est souvent abordée par essai-erreur, ce qui mène à des corps verts avec une faible résistance, cause des pertes grandes de production et décroit la capacité du processus d'impression de produire des détails délicats.

Cette problématique a motivé l'étude des interactions polymère-polymère et métal-polymère donnant de la résistance aux corps verts avec l'objectif d'établir des nouvelles lignes directrices pour la sélection de nouveaux liants. Ce projet a mené au développement d'une méthode pour produire des données fiables et quantitatives de la résistance de corps verts préparés avec différents liants polymériques. Le métal d'intérêt dans cette étude est l'acier inoxydable 316L (SS 316L). L'alcool polyvinylique (PVA), l'acide polyacrylique (PAA) et le polyvinylpyrrolidone (PVP) ont été choisis pour étudier les interactions donnant de la résistance aux corps verts, comme ils contiennent différents groupes fonctionnels capables de subir des réactions contrastantes ave la surface du métal. Également, leurs propriétés mécaniques sont distinctes et ils éprouvent différentes interactions en solution.

Des échantillons de polymère pur et des corps verts avec des concentration différentes de liant ont également été préparés. Le contenu de liant dans les corps verts a été caractérisé avec le facteur de remplissage Φ, défini comme la fraction de volume poreux occupé par le liant sec. Des images MEB d'échantillons fracturés ont montré différentes distributions de liant dans les pièces, dépendamment du polymère. Les différents comportements des liants ont été expliqués en se basant sur les propriétés physicochimiques et sur les interactions à l'intérieur du liant et avec la surface métallique. Finalement, les effets du poids moléculaire (M_w), du pH et des additifs (encre commerciale et agent de réticulation) sur la résistance ont été étudiés.

L’analyse du comportement des trois liants ont permis de proposer une courbe modèle de la résistance des corps verts vs Φ. Également, des nouveaux critères de sélection ont été élucidés et un algorithme de sélection d’ingrédients de liant a été proposé. L’algorithme peut être utilisé pour développer des nouveaux liants écologiques et haute-performance pour les méthodes d’impression 3D de métaux utilisant des liants telles que les jets de liant.

ABSTRACT

Binder-jet printing is an advanced manufacturing technique where the alternating deposition of a metal powder bed, then printing of a polymeric binder are repeated until a three-dimensional part is formed. The resulting piece is called green body. It is composed of powder particles held together by the binder. To obtain a pure metallic part, the piece must be treated thermally to pyrolyze the polymer and to sinter the powder particles. It is one of the most promising metal 3D printing techniques. However, the selection of binders is often approached by trial and error, which leads to poor green bodies strength, causes high production loses and decreases the printing process capacity to produce delicate features.

This problematic motivated the study of the polymer-polymer and metal-polymer interactions giving strength to green bodies with the objective of stablishing new binder selection guidelines. This project led to the development of an out-of-printer method to produce reliable and quantitative data of the strength of green bodies prepared with different polymeric binders. The metal of interest in this study is stainless steel 316L (SS 316L). Polyvinyl alcohol (PVA), polyacrylic acid (PAA) and polyvinylpyrrolidone (PVP) were selected to study the interactions giving strength to green bodies, as they contain different polar functional groups capable of undergoing contrasting reactions with the metal surface. Also, their mechanical properties are distinct, and they experience different interactions in solution.

Pure polymer samples and green bodies with varying binder concentrations were prepared. The binder content in the green bodies was characterized with the fill factor Φ, wich is defined as the pore volume fraction occupied by the dried binder. SEM images of fractured samples showed different binder distributions in the pieces, depending on the polymer. The different binder behaviors were explained based on physicochemical properties and interactions within the binder and with the metal surface. Finally, the effects of the molecular weight (M_w), pH and additives (commercial ink and crosslinking agent) on strength were studied

The analysis of the behavior of the three binders allowed to propose a model curve of green strength vs Φ. Additionally, new binder selection criteria were elucidated, and a binder ingredient selection algorithm was proposed. The algorithm can be used to develop new, ecofriendly, and high-performance binders for binder-based metal 3D printing methods such as binder jetting.

TABLE OF CONTENTS

DEDICATION III

ACKNOWLEDGEMENTS IV

RÉSUMÉ V

ABSTRACT VII

TABLE OF CONTENTS VIII

LIST OF TABLES XI

LIST OF FIGURES XII

LIST OF SYMBOLS AND ABBREVIATIONS XVII

LIST OF APPENDICES XXI

CHAPTER 1 INTRODUCTION 1

1.1 Context 1

1.1.1 Additive manufacturing and traditional manufacturing 1

1.1.2 Binder jetting (BJ) 3

1.2 Problematic and objective 5

CHAPTER 2 LITERATURE REVIEW 7

2.1 Binder 7

2.1.1 Printhead considerations 7

2.1.2 Types of binders 10

2.1.3 Binding materials 11

2.1.4 Solvents and additives 15

2.1.5 Binder penetration mechanism 17

2.1.6 Saturation ratio and binder drying 19

2.2 Green strength 20

2.2.1 Summary of printing parameters' effect on green strength....20
2.2.2 Interparticle bonds....21
2.2.3 Mechanical tests....24
2.2.4 Strength of green bodies in the literature....26
2.3 Binder selection....29
2.3.1 Ink formulation algorithms....29
2.3.2 Other selection criteria....32
2.4 Metallic surface....33
2.4.1 Polymer metal interface....34
2.4.2 Properties of stainless steel 316L....35
2.5 Polymer properties....37
2.5.1 Concentration regimes in polymer solutions....37
2.5.2 Solubility parameter....40
2.5.3 Polymer mechanical properties....40
2.5.4 PVA PVP PAA properties....41
CHAPTER 3 OBJECTIVES, MATERIALS AND METHODS....46
3.1 Objectives....46
3.2 Materials and Methods....46
3.2.1 Materials....46
3.2.2 Binder preparation and characterization....48
3.2.3 Sample formation....49
3.2.4 Mass and dimensions....51
3.2.5 Mechanical test....52
3.2.6 SEM....53

3.2.7 Binder distribution....54
CHAPTER 4 KEY RESULTS AND DISCUSSION....56
4.1 Binder concentration and mechanical properties....56
4.1.1 PVA....56
4.1.2 PAA and PVP....64
4.2 Effect of molecular weight....68
4.3 Effect of pH....69
4.4 Effect of ink....70
4.5 Proposed binder selection algorithm....74
4.6 General discussion....77
CHAPTER 5 CONCLUSION AND RECOMMANDATIONS....82
5.1 Summary of key findings....82
5.2 Limits encountered and future work....84
REFERENCES....86
APPENDICES....101

LIST OF TABLES

Table 2.1 Powder - organic binder systems in the literature. 11

Table 2.2 Examples of the principal ink ingredients. These ingredients can be used for all the inkjet printing technologies [78]. 16

Table 2.3 Summary of binders and green strengths in the literature. CT stands for compression test, DCT, for diametral compression test and FT, for flexural test. 26

Table 2.4 SS 316L composition according to ASTM A240/A240M standard 35

Table 2.5 Isoelectric points (pI) of the metal oxides present at the SS 316L surface. 37

Table 3.1 Composition of the SS 316L powder (see also appendix B) 47

Table 3.2 Summary of polymers and additives' use and their concentrations range in solution... 48

Table 3.3 Summary of Cb, Cg and paste compositions. 52

Table 4.1 Physicochemical properties of the 3 binders used to prepare 0.69 wt. % (Cg) samples. 66

Table 4.2 Physical properties of the PVA binder solution with and without ink (1-15 wt. % addition). 71

Table A.1 Summary of characteristics of the 7 AM families..... 108

Table A.2 Main applications of the 7 AM families..... 109

LIST OF FIGURES

Figure 1.1 BJ system schematic. 4

Figure 1.2 Debinding and sintering process. a) green body; b) Heat treatment at low temperature (400 °C - 600 °C) to obtain a brown body; c) Heat treatment at elevated temperatures (900 °C - 1400 °C) to sinter the piece; d) final piece. 4

Figure 1.3 Project overview. The work of this thesis is part of a broader project that is composed of three master's thesis and the help of an industrial partner. Package 1 is the focus of this project while packages 2, 3 and 4 were pursued by my colleagues. 6

Figure 2.1 Primitive overlapping to form green bodies [25]....7

Figure 2.2 Printable region based on dimensionless numbers Weber number, Reynolds number, and Z number (adapted from [27]). 8

Figure 2.3 Binder types adapted from NSERC CRD grant application by Tavares et al. 10

Figure 2.4 Primitive formation mechanism....18

Figure 2.5 Liquid pendular bridge formation [80]. 18

Figure 2.6 Binder distribution types. a) nonwetting binder, b) wetting binder, wetting binder with a high viscosity [88]. 22

Figure 2.7 Pendular bond geometry model [88]. 23

Figure 2.8 Types of failure of interparticle bridges [36]. a) Adhesive failure. b) Cohesive failure 24

Figure 2.9 Typical stress vs strain curve of a green compression test. Region A: particle rearrangement and binder shear; region B: binder shear and decohesion; region C: initiation of cracks [60]....25

Figure 2.10 Ink formulation algorithm proposed by Uthela et al [32]. 30

Figure 2.11 Ink formulation algorithm proposed by Tam et al. (adapted from [27]). 31

Figure 2.12 Surface charge of different metal oxides as a function of their isoelectric point [102]. 33

Figure 2.13 Schematics of the polymer-metal surface [100]. 34

Figure 2.14 Radius of gyration in the bead-stick model [77].....38

Figure 2.15 Conformation of a highly entangled polymer solution [77]. 39

Figure 2.16 a) Modulus regimes as a function of temperature. b) Typical stress - strain plots for different types of failure: brittle (A); brittle-ductile (B); ductile-brittle (C); ductile (D); and rubber (E) [127].....40

Figure 2.17 Polymer mechanical strength dependence on molecular weight [128]. 41

Figure 2.18 Molecular structure of PVP, PVA and PAA.....41

Figure 2.19 Structure of partially hydrolyzed polyvinyl acetate [132]. 42

Figure 2.20 Binding mechanisms of the carboxyl group on metal surfaces [155].....45

Figure 3.1 BSE SEM images of the SS316L powder. 47

Figure 3.2 Green body preparation schematic: a) paste preparation, b) mould assembly and c) sample preparation. 50

Figure 3.3 Green body strength analysis by compression test ($N \geq 3$): a) mechanical test schematic, b) data analysis schematic, c) green body before compression and d) green body after compression.....53

Figure 3.4 Bond length measurement with ImageJ. The white arrows point at spaces that are probably . The yellow arrow point at the limits of the binder bridge distinguishable with the eye. 54

Figure 3.5 Binder distribution on a green body with respect to the height of the piece ($Cg = 0.69$ wt. %). The three images come from different broken parts of the same sample.....55

Figure 4.1 0.2 % yield strength of PVA green bodies as a function of Cg. Errors are 95% C. I..56

Figure 4.2 Schematic of the cylindrical beam model.....57

Figure 4.3 Model curve of the maximum bond strength as a function of bond radius for a single bond according to equation 4.2 for two different binder strengths. 58

Figure 4.4: BSE SEM images of fractured PVA green bodies with different Cg values: a) 0.33 wt. %, b) 0.69 wt. % and c) 1.39 wt. % . Yellow arrows point at the slim binder lines coming out of the annular mark. Red arrows point at places where the polymer failed cohesively. White arrows point at interparticle necking regions. 59

Figure 4.5 Binder drying mechanisms and final bridges. The blue binder is liquid, and the green binder is solid after evaporation. a) Initial state (100 % SR). b-c-g-h) Binder drying, reduction of the SR. d-f-i) Types of interparticle bridges. e) Strong interparticle network (preferred). j) Weak interparticle network (not preferred): due to the binder distribution, more binder is needed to form interparticle bridges.....60

Figure 4.6 0.2 % yield strength of PVA green bodies as a function of the fill factor. Errors are 95% C. I. 61

Figure 4.7 Relative density of PVA green bodies as a function of Cg. Errors are 95% C. I. 62

Figure 4.8 Strength as a function of the fill factor model curve. Region A: induction period where no interparticle bridges have formed; Region B: interparticle bridge network formation and bond coarsening; Region C: tail off to pure polymer properties.....63

Figure 4.9 0.2 % yield strength of green bodies made with PVA, PVP and PAA binders with respect to the fill factor. Errors are 95% C. I. 65

Figure 4.10 BSE SEM images of PVA, PVP and PAA green bodies with two different Cgvalues: 0.69 wt. % in the top and 1.39 wt. % in the bottom. Red arrows point at places where the polymer failed cohesively. 67

Figure 4.11 0.2 % yield strength of PVP green bodies as a function of the molecular weight. Errors are 95 % C. I. 69

Figure 4.12 0.2 % yield strength of PAA green bodies as a function of the binder's pH ($Cb = 5$ wt. %). Errors are 95 % C. I. 70

Figure 4.13 0.2 % yield strength of green bodies made with PVA, PVP and PAA binders as a function of the fill factor for samples a) with and b) without ink (1-15 wt. % of the binder solution). Errors are 95% C. I. 72

Figure 4.14 BSE SEM images of fractured PVA, PVP and PAA green bodies with a Cg value of 0.33 wt. % with and without ink. 73

Figure 4.15 0.2 % yield strength of green bodies made with PVA + ink binder as a function of crosslinker concentration in the binder solution. Errors are 95 % C. I. 74

Figure 4.16 Binder selection algorithm. Squares represent process steps, diamonds, conditions, and parallelograms, testing operations. Diamonds inside one box need to be all respected. The circled steps are the ones proposed based on the findings of this work. 75

Figure A.1 Metallic AM families 101

Figure A.2 Vat photopolymerization system schematic. 102

Figure A.3 Material extrusion system schematic. 103

Figure A.4 Material jetting system schematic. 104

Figure A.5 Sheet lamination system schematic. 105

Figure A.6 Directed energy deposition: a) system schematic; b) multi-axis system schematic (adapted from [199]). 106

Figure A.7 Powder bed fusion system schematic. 107

Figure A.8 Schematic representation of a) a doctor blade and b) a roller [210] 112

Figure A.9 Powder deposition mechanism with a hopper [211]. 112

Figure B.1 Certificate of analysis of the 316L powder. 114

Figure C.1 SEM and EDX images of a saturated PVA green body. 115

Figure C.2 Ilastik and ImageJ image treatment steps for the SEM images of green bodies. 115

Figure C.3 Binder area pixel counting. Top: BSE SEM images of PVA green bodies with different concentrations (dry binder mass/green body mass). Bottom: binder pixel segregation results from Ilastik. 116

Figure D.1 Low magnification SEM BSE image of a 0.68 wt. % (dry binder mass/green body mass) PVA green body. 117

Figure E.1 BSE SEM images of green bodies made with different PVP 5 wt. % binders with different molecular weights. 118

Figure F.1 BSE SEM images of PVA green bodies with ink and increasing fill factor. The concentrations indicated in the top of the images are dry binder mass/green body mass ratios. 119

Figure G.1 0.2 % yield strength of PVA green bodies for two hydrolysis percentages. 120

LIST OF SYMBOLS AND ABBREVIATIONS

α	Nozzle radius
A_{green}	Cross-section area
AM	Additive manufacturing
b	monomer length
BSE	Back-scattered electrons
c^*	Overlap concentration
c^{**}	Concentrated solution
Ca	Capillary number
C_b	Binder concentration
CED	Cohesive energy density
C_g	Green concentration
C. I.	Confidence interval
CT	Compression test
θ	Contact angle
δ	Solubility parameter
ΔH_v	Molar enthalpy of vaporization
DCT	Diametral compression test
ΔP	Pressure
ε	Powder packing density
ϵ	Correlation length
η	Viscosity
F	Load

F_{bond} Maximum load supported by one interparticle bond

Φ Fill factor

FT Flexural test

γ Surface tension

γ^d Dispersive component of the surface tension

γ^p Polar component of the surface surface tension

h Bridge length

I Moment of inertia

k Average number of neighbour particles

$m_{additives}$ Mass of the additives

m_{piece} Mass of the piece

$m_{polymer}$ Mass of the polymer

$m_{solvent}$ Mass of the solvent

M Torque

M_e Molecular weight for entanglement

M_w Molecular weight

μ Velocity of the fluid

n Number of bridges

N Number of monomers

ν Flory exponent

Oh Ohnesorge number

p Volume fraction of pores

PAA Polyacrylic acid

pI	Isoelectric point
pK_a	Acid dissociation constant
PVA	Polyvinyl alcohol
PVP	Polyvinylpyrrolidone
R	Particle radius
r	Bridge outer radius
r_0	Bridge inner
r_1, r_2	Curvature radiuses
R_c	Universal gas constant
Re	Reynolds number
R_g	Gyration radius
ρ	Density
S	Surface area
σ_{binder}	Binder strength
σ_{CT}	Compression test strength
$\sigma_{cylinder}$	Cylinder strength
σ_{green}	Green strength
SEM	Scanning electron microscope
SR	Saturation ratio
SS	Stainless steel
$T°$	Temperature
TM	Traditional manufacturing
v	drop velocity

V' $V_{air} + V_{binder}$

V_{air} Air volume

V_{binder} Binder volume

V_{bridge} Bridge volume

V_m Molar volume

V_{metal} Metal volume

$V_{particle}$ Particle volume

V_{piece} Piece volume

W_a Work of adhesion

We Weber number

y Highest stress accumulation point

Z Z parameter

LIST OF APPENDICES

Appendix A Suplementary litterature review....101

Appendix B Certificate of analysis of the metalic powder 114

Appendix C Binder identification in SEM images....115

Appendix D Binder interonnections....117

Appendix E Effect of molecular weight: SEM images 118

Appendix F Fill factor of PVA samples with ink....119

Appendix G Effect of hydrolysis percentage 120

CHAPTER 1 INTRODUCTION

1.1 Context

1.1.1 Additive manufacturing and traditional manufacturing

Additive manufacturing (AM) or 3D printing is a relatively new manufacturing technique that consists of building pieces directly from a computer-assisted design (CAD) model. In this method, a model is converted into a 3D printing file format (STL, OBJ, AMF, 3MF, etc. [1]) and divided into two-dimensional slices. The 3D printer will then fabricate one slice at a time, adding material until the formation of a three-dimensional piece is finished [2-4]. It is one of the three main manufacturing techniques used in today's industry, the other two being subtractive manufacturing and formative manufacturing [5]. Subtractive manufacturing consists of using bulk portions of raw material to fabricate three-dimensional bodies by cutting material away. The main disadvantages of this technique are that it produces large quantities of wasted material and that it generally requires the use of many machining tools and many separate production steps, which results in the management of long supply chains and long production times [6]. Also, subtractive manufacturing is difficult to use for certain materials such as glasses, ceramics, and concrete. Formative manufacturing designates all the fabrication methods that use deformation to shape pieces. Some examples are casting, injection moulding, forging and stamping. One important drawback in this fabrication category relies on the development of a mould or specialized tooling: in order to build one piece, one must develop two or more. For this reason, the time required to develop a piece and get it to a production level is long in traditional manufacturing (TM). AM significantly reduces the lead time between design and production, and thus allows for rapid prototyping. The fact that one only needs a computer, a 3D printer and a CAD model to build a piece simplifies much of the fabrication process. This is why this technique has been able to find its place as a personal household device for polymer printing [7]. AM drastically changes the production cycle, as traditional supply chains and manufacturing lines are bypassed and the development cycle is shortened [5].

The most significant characteristic of the layer-by-layer method of AM is that it allows the fabrication of complex shapes that cannot be obtained using any other TM technique, or are too expensive to be fabricated by traditional means (enclosed structures, lattices, channels, etc.) [6, 8].

In fact, in TM, the price of finished parts increases exponentially with their complexity as opposed to AM, for which price increases linearly [7]. However, the cost-per-piece of TM decreases exponentially as the part's volume increases [7]. In this case, the prices in AM stay relatively constant, but the printed volume is limited by the printer size. Nonetheless, some AM techniques, such as binder jetting and direct energy deposition, can print pieces with volumes on the order of several cubic meters [6]. Another interesting relation between TM and AM is related to the production volume. Prices are significantly lower for TM if the pieces are massively produced while in AM, prices do not vary with production volume [9]. For those reasons, AM is better suited for low-volume high-performance pieces. It is more cost-effective for customized products and functionalized geometries. It has thus found its place in almost every industry, but it is a key manufacturing technique for the aerospace, automotive, defence and biomedical industries [7, 10].

Additionally, AM is considered as a clean and renewable manufacturing method. Since it allows for recycling 95-98% of its waste material, it reduces the usage of 75% of the raw material [5], it uses less harmful chemicals [11], and it reduces the energy consumption for the production and use of the pieces [8, 11]. In fact, AM enables the realization of environmentally friendly designs since AM parts can be highly functionalized. This means that the freedom of design in AM allows users to create pieces that are more optimized. As a result, they perform better and they use less energy when they are being used. Usually, this optimization also means less consumption of material and energy during production (ex: light-weight components in the aerospace industry). In addition, this technique helps in reducing the general carbon emissions as the parts can be fabricated in-place, reducing transportation needs [8, 11]. Finally, AM allows companies to save storage space, since they can save the CAD files of parts and print them as needed. This prevents those parts from becoming outdated while being stored and reduces the part management costs [8]. Consequently, AM is well suited to be integrated into a just-in-time production[1] system and inherently moves industries towards a vertical integrated manufacturing[2] process.

---

[1] Management strategy that reduces costs by matching the product inventory with the forecasted demand.

[2] Vertical integration implies taking control of several production steps by the same company, which results in shorter supply chains.

This said, even though at some point the general belief was that AM could replace all TM in the so-called fourth industrial revolution (manufacturing 4.0) [4], nowadays, this overtake of AM seems unlikely [6]. The industry tends more to their combination, which is called hybrid manufacturing (HM) [7]. TM can profit from the flexibility of AM as it can provide new and specialized tooling and moulds [5]. Also, TM and AM can be combined to fabricate different parts of the same piece in such way that the most functionalized part would be done by AM and the rest, by TM [12]. Additionally, AM has the potential to reduce the dependency of manufacturers on traditional supply chains [7]. This is particularly interesting in the case where the supply chains are disrupted due to an uncontrollable disaster. For instance, during the COVID-19 crisis, stress due to medical components shortages, such as oxygen valves and face masks, were relieved in some hospitals thanks to low volume local AM production [13].

1.1.2 Binder jetting (BJ)

BJ is one of the 7 AM families [4, 5, 14]. It consists of printing a binder on successive powder layers of micrometric thickness [5]. For this, a two-piston system is generally used. Each piston controls one powder reservoir, one with the raw metallic powder and the other with the building area (printed piece and lose powder). First, a counter-rotating roller brings powder from one reservoir to the other and spreads it evenly on the surface of the second container (see also appendix A). Then, the print head selectively jets the binder over the powder bed. After a heating element passes through the building area to dry the binder, the piston with the powder feedstock moves up and the one with the building area moves down. This process is repeated until the formation of the 3D piece is finished (Figure 1.1). At that point the printed part is a “green body”, à mixture of binder and metal, that must be removed from the building area and cleaned. This process is called de-powdering and consists of the removal of lose metallic powder from the piece thanks to vacuum and brush cleaning. Generally, the loose powder is recycled and fed back into the printing process.

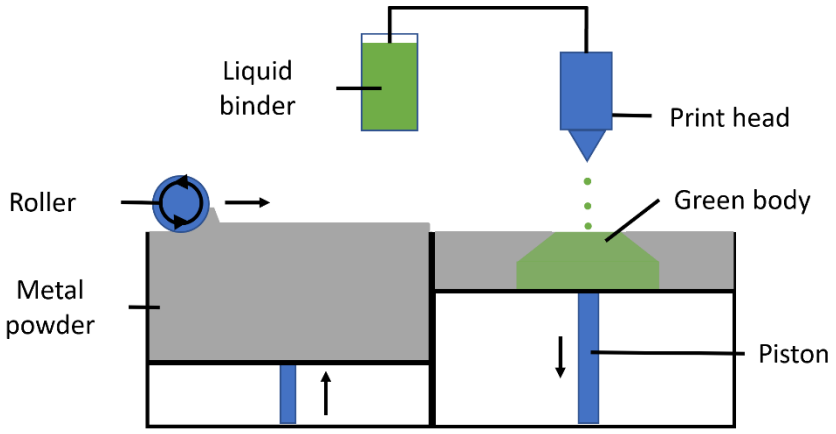

Figure 1.1 BJ system schematic.

In some cases the pieces are designed to be used as green bodies [7]. However, to obtain a pure metallic part, the green body must go through a debinding and sintering heat treatment process. Debinding occurs at relatively low temperatures (300 °C - 800 °C [15, 16]), temperatures sufficiently high to remove the organic binder by pyrolysis and leave the less possible amount of polymer residue behind. This process transforms the green body in a "brown body", a fragile piece made of metal particles that are held together by carbon residue [17], friction forces [18], and unions where sintering has started. Finally, the piece must be treated at higher temperatures (900°C-1400°C), around 2/3 the melting point of the metal, to completely sinter the piece and obtain a solid metallic part [19]. If the brown body is sintered at higher temperatures, it might deform. The final piece shows a dimensional reduction, called shrinkage, as the initial structure is highly porous (~50 % dense) and the final one is close to full density (85- 99 % dense) [20]. This process is illustrated in Figure 1.2 (see also appendix A).

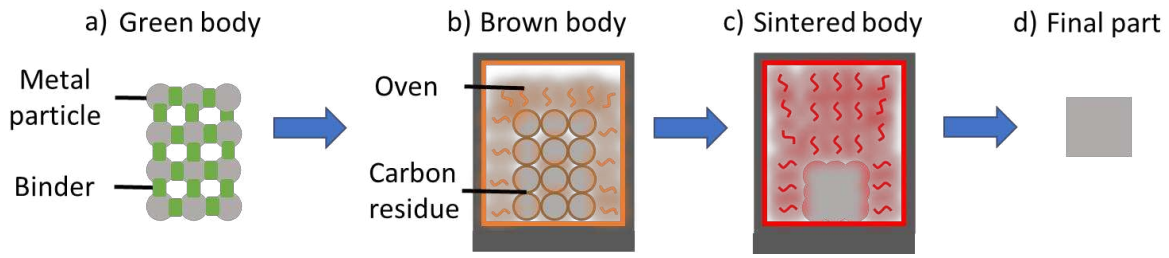

Figure 1.2 Debinding and sintering process. a) green body; b) Heat treatment at low temperature (400 °C - 600 °C) to obtain a brown body; c) Heat treatment at elevated temperatures (900 °C - 1400 °C) to sinter the piece; d) final piece.

1.2 Problematic and objective

BJ is one of the most promising techniques, industrially, as it possesses many advantages over the other AM techniques: it has a broader material versatility (polymers, ceramics, food, metals…virtually any powder), one of the highest resolutions and speeds, one of the lowest building volume restrictions and consumes less energy [6] (see also appendix A for an AM families comparison). Despite all of those advantages, BJ is only the fourth most used AM technique for metallic printing [21]. Even though, in some applications, BJ can compete with the most popular techniques [10], the main disadvantage holding back its flourishing is related to the mechanical properties of the pieces. During their fabrication, green and brown bodies can be fragile [22, 23], which can cause high production losses. Additionally, final pieces can have poor properties due to high porosity and impurity content [6, 10]. These flaws are related to the binder properties and to the printing, debinding and sintering parameters.

This master's thesis is part of a larger project that involves two other master's projects and the collaboration of an industrial partner. The overall project is divided in 4 work packages (Figure 1.3). Packages 2 and 4 are being pursued by other students, package 3, by our partners, as they own a BJ printer, and package 1 is the focus of this work.

Most of the work in the literature to improve BJ focuses on optimizing the process parameters without answering what makes a good binder and how to chose one, depending on the material to be printed [15]. In fact, binder selection in BJ additive manufacturing is mostly done by trial and error. This is a consequence of three factors:

- The number of ingredient choices is extremely vast. There exist a wide range of basic and intermediate chemical products that can result in thousands of binder formulations.
- The same binder formulation may allow the formation of green bodies with different powder materials. However, the impact of the binder on the final piece is difficult to trace due to the tremendously high number of parameters that influence the final properties. In other words, as the binder seems to be working fine, the attention is deviated to other aspects of the process.
- There is a lack of understanding of the fundamental interactions that make a good binder.

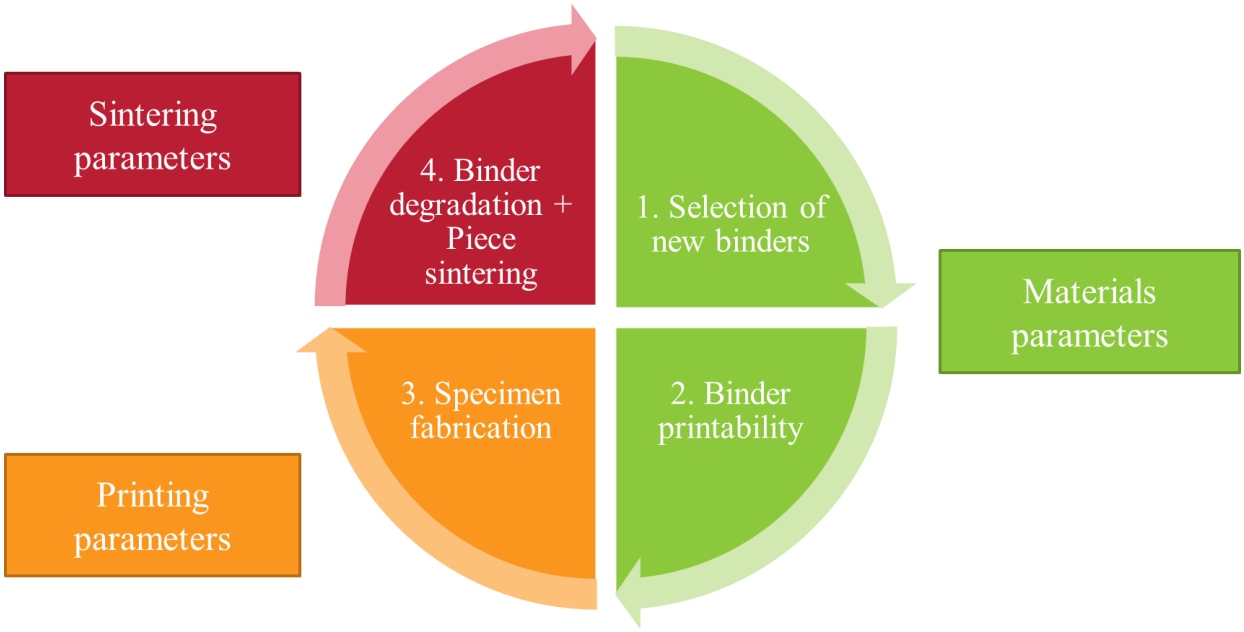

Figure 1.3 Project overview. The work of this thesis is part of a broader project that is composed of three master's thesis and the help of an industrial partner. Package 1 is the focus of this project while packages 2, 3 and 4 were pursued by my colleagues.

Thus, the main objective of this work is to establish binder design parameters for BJ additive manufacturing based on the polymer-polymer and metal-polymer interactions, aiming for increased strength in the resulting green bodies. These parameters will serve as guidelines to develop new high performance and low ecological impact binders and to screen binder candidates more easily.

CHAPTER 2 LITERATURE REVIEW

2.1 Binder

2.1.1 Printhead considerations

The printhead controls the printing speed and droplet parameters such as volume, ejection rate and spacing [23]. The printhead speed is often increased to achieve faster printing rates. However, if the lateral speed of the droplet is too high, accuracy might be lost, as the powder can be disrupted by the impact of the droplet and the liquid might rebound [23]. The drop ejection rate, volume and spacing control the total volume of binder delivered to the powder bed on each layer. Therefore, these parameters govern the final amount of binder in the green piece. These parameters also ensure that the binder drops overlap, a necessary criterion for green part formation, else the cohesion of the piece is not maintained [24] (Figure 2.1) .

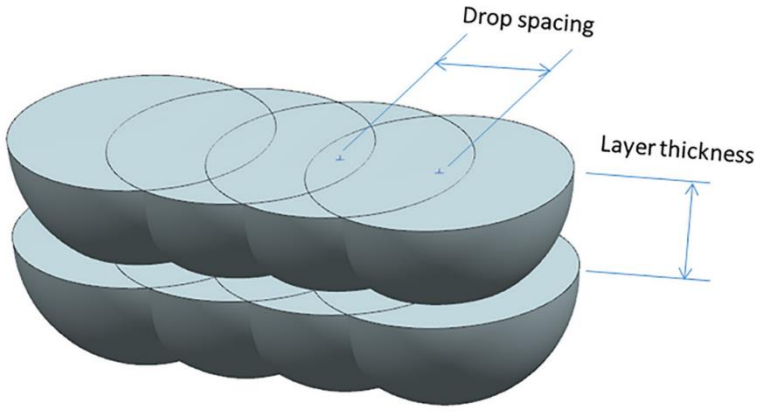

Figure 2.1 Primitive overlapping to form green bodies [25].

Additionally, the printhead characteristics determine the physicochemical properties of the binders for two reasons: binder printability and pinhead protection. The printability can be estimated thanks to the dimensionless Weber number We, Reynolds number Re, and Ohnesorge number Oh [26]:

$$Re = \frac{v\rho\alpha}{\eta} \tag{2.1}$$

$$We = \frac{v^2 \rho \alpha}{\gamma} \tag{2.2}$$

$$Oh = \frac{\sqrt{We}}{Re} = \frac{\eta}{\sqrt{\gamma \rho \alpha}} \tag{2.3}$$

$$Z = \frac{1}{Oh} = \frac{\sqrt{\gamma \rho \alpha}}{\eta} \tag{2.4}$$

where v, ρ, α, η and γ are the drop velocity, the density, the capillary radius of the nozzles, the viscosity and the surface tension. In fact, Derby proposed a region in the Weber number-Reynolds number coordinate system that defines whether a binder will correctly form droplets (Figure 2.2) [26, 27]. The boundaries of that region are defined by Z (eq. 2.4), We and $Re^{\frac{1}{4}}We^{\frac{1}{2}}$. To give an idea of the order of magnitude of these variables, typical values for the ejection speed, surface tension, viscosity, density and nozzle radius are 8 m/s [28] , 41.6 − 47.9 mN/m, 1 - 9 cP, 1.02−1.1 g/ml and 11 μm [29] , respectively.

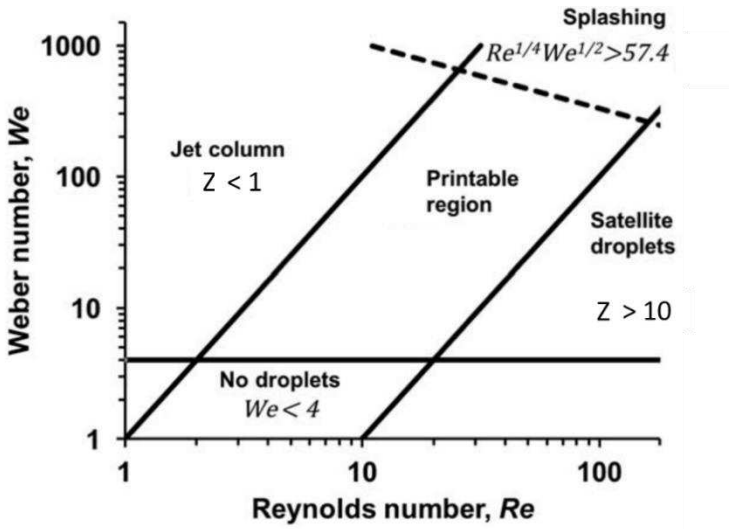

Figure 2.2 Printable region based on dimensionless numbers Weber number, Reynolds number, and Z number (adapted from [27]).

In Figure 2.2, the upper and lower limits, defined respectively by We and $Re^{\frac{1}{4}}We^{\frac{1}{2}}$, represent the relation between the droplet viscosity and kinetic energy. In fact, We puts in evidence the competition between inertial forces and the surface tension of the liquid while Re is the ratio of inertial forces to viscous forces. Therefore, if $We < 4$ the ejection velocity of the liquid from the printhead nozzles is not high enough to form a droplet. On the other hand, the upper limit, if the speed is too high, the drop splashes on the powder bed surface. For smooth powder beds, splashes take place if $Re^{\frac{1}{4}}We^{\frac{1}{2}} > 57.4$. However, this condition depends on the roughness of the powder bed [30].

Concerning the left and right limits, Z depicts the relation between droplet viscosity and surface tension. Viscosity restricts the mobility of the liquid and surface tension tends to minimize the surface area. Therefore, if $Z < 1$ the binder is too viscous, or the surface tension is too low. As a result, it will not break into droplets. It will simply form a continuous jet. On the contrary, if $Z > 10$ the binder will tend to form satellites, little parasite droplets that form around the main droplet and ruin the print resolution. This said, these dimensionless numbers serve only as a first approximation and every binder formulation must go through a series of experiments to validate the printability. In fact, some binders in the printable zone have been found to have poor printability [29]. Other parameters such as the critical overlap concentration C^* have been proposed also as a start point to select the binder viscosity [29].

Besides ensuring the printability of the binder, one must respect the pinhead constraints concerning pH, suspended particle size and re-solubility [31]. In fact, high and low pH binders might corrode the nozzles of the printhead. The pH should be as close to 7 as possible. In fact, as a rule of thumb, the compatibility of the solvents in the binder and the printhead must be verified before any test with the printer. Additionally, the binder might clog the nozzles if it contains suspended particles with diameters close to the nozzle diameter. To be safe, the suspended particle size should be 100 times smaller than the nozzle diameter [31]. Also, binders should always be filtered before being used on the printer to remove any agglomeration and impurity that could block the nozzles [32]. Finally, wile the printer is not in use, the binder might get dry, causing clogging. This can be avoided by choosing binder ingredients that can re-dissolve once the printer restarts [31] or by including humectants such as glycol esters [27, 33].

2.1.2 Types of binders

The binder can be used in three different configurations (Figure 2.3) [32, 34]. It can be a powder, a liquid or a reactive binder. When used as a powder, it must be mixed with the metal particles and put in the powder reservoir. The printhead selectively jets a liquid that reacts with the solid binder to trigger the adhesion of the metal particles. However, mixing the binder as a powder adds a step to the whole process and several difficulties linked to the migration of the binder particles within the powder bed and the powder reservoir appear [35]. Thus, in-bed binders are rarely used in metallic BJ printing.

Reactive binders are those that need a specific reaction to take place with the help of external energy sources or the mixture of reactive ingredients in the powder bed. For instance, some binders need to be heated at a certain temperature to initiate a crosslinking reaction [36]. In other cases, the binder cures with the help of ultraviolet light [37]. The reaction can take place at every printing layer or at the end of the printing process. It is common use to put the entire build box in an oven to cure the binder between 80 and 200°C [38, 39]. Therefore, the use of this type of binder results in stronger green bodies, but longer production times.

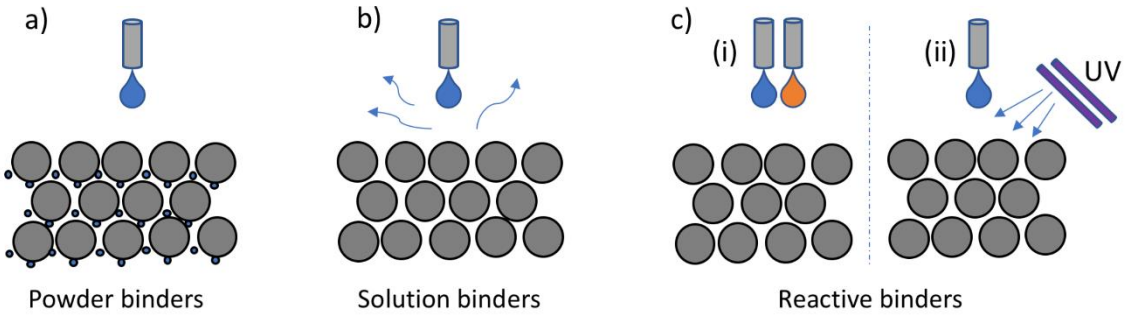

Figure 2.3 Binder types adapted from NSERC CRD grant application by Tavares et al.

Finally, liquid binders are the most common type. They are liquid solutions that contain all the binding ingredients dissolved at relatively low concentration (3 to 15 wt. %). This configuration simplifies the formation of the powder beds, but complexifies the binder formulation design. This work focuses on this type of binders.

2.1.3 Binding materials

An extensive review of binding methods can be found in [31, 32]. They classify binders in 8 categories: organic, inorganic, metal-salts, hydration based, solvent, acid-base systems, phase-changing systems and sintering aids [31]. However, not all of these can be used for metallic printing. In fact, organic polymer-based binders are often preferred as they are easily decomposed during debinding [27]. Also, they do not require an specific reaction to work and can bind a large variety of materials [31]. A list of organic binder materials can be found in Table 2.1.

Table 2.1 Powder - organic binder systems in the literature.

Printed material	**Organic binder**
SS 316L	Phenolic resin - alcohol - Glycol [40] Polyvinylpyrrolidone (PVP) [41] Ethylene glycol monobutyl ether - isopropanol - Ethylene glycol [42] SS 316L nanoparticles - ethylene glycol or diethylene glycol [43]
SS 420	Poly(triethylene glycol dimethacrylate) [44] Ethylene glycol monobutyl ether - isopropanol - ethylene glycol [42] Colloidal latex [45]
SS630	Poly(methyl methacrylate) - cellulose acetate butyrate - polyethylene glycol [17]
Iron alloys	Diethylene glycol [46] Polyvinyl alcohol (PVA) [47]
Ti3SiC2	Dextrin + glycerin [48]

Table 2.1 Powder - organic binder systems in the literature (continued).

Printed material	Organic binder
Titanium	PVA - PVP [49]
	PVA - commercial ZB60 binder [50]
	PVA [51]
Titanium carbide	Dextrin [52-54]
Titanium oxide	Dextrin [53, 54]
	PAA [36]
Alumina	Dextrin [55]
	Acrylic copolymer emulsion [56]
	PAA [36, 57]
	Styrene-acrylic copolymer [57]
	Acrylic copolymer [57]
	Dextrin - commercial ZB 54 [58]
	styrene acrylic co-polymer - polyethylene glycol [59]
	methylcellulose [60]
Tungsten carbide - 10 wt. % cobalt	Polyethyleneimine [61]
Silicon	Dextrin [62]
	Copolymer of methyl ester of acrylic acid - polyurethane [63]
	Starch [63]

Table 2.1 Powder - organic binder systems in the literature (continued).

Printed material	Organic binder
Silicon carbide	Dextrin [62]
Silicon nitride	Styrene acrylic co-polymer - polyethylene glycol [59]
Silicon oxide	PAA [36] Methylcellulose [60]
Neodymium magnet	Diethylene Glycol [64]
Gibbsite	Methylcellulose [60]
Hydroxyapatite	PVA [65, 66] Dextrin - PAA - glycerol [67] PVP [65] Polyacrylamide [65] Maltodextrin [66, 68]
Polyethylene	Maltodextrin [69]
Self-binding with water	Cornstarch - dextran - gelatin [70]
13-93 bioactive glass	Polyvinyl butyral [67] Polyethylene glycol [67] Dextrin [67]

Table 2.1 Powder - organic binder systems in the literature (continued).

Printed material	Organic binder
Glass - ceramic mixture (MgO, CaO, SiO_2, P_2O_5, CaF_2)	Maltodextrin [68]
Calcium zirconate	PVP - polyether copolymer [71]
Yttria stabilised zirconia	PVP [72]
Ceramics and metals in general	Butyral resins, polymeric resins, polyvinyls, sucrose [31]
	Polyvinyl acetate, starch, acrylates, PVA, polyethylene oxide, ethylene vinyl acetate [73]
	PAA, PVP, polymethyl methacrylate, PVA, Poly(methyl vinyl ether-alt-maleic anhydride), polyamides, polyacrylamide [74]
	Polysaccharides, starch, dextrin, amylose, amylopectin [75]

It is to be noted that dextrin, a recuring binder in Table 2.1, is mostly used as an in-bed binder. It is activated with a proprietary water-based solution and it is principally used for ceramic printing. Also, diethylene glycol is the most commonly used ingredient in binder jetting formulations [39], as it has a double function: it can be a binding agent [46, 64] or a humectant (agent to prevent binder drying in the printhead nozzles) [27, 33].

Concerning the properties of the organic polymer, recently, the authors of [29] studied the effect of molecular weight, polymer morphology and binder concentration on the strength of green bodies. Their samples were made of a mixture of sugar and lactose powders and they used PVP as binder. Their results showed that green strength increases with concentration and molecular weight. Other studies have shown similar results [40, 76]. Interestingly, the same authors found that by using a star shape polymer they could prepare binders with higher amounts of polymer but keeping

a low viscosity. In fact, the viscosity of polymer solutions is reduced if the chains are less extended, as they experience less friction [77]. For that reason they were able to print pieces with higher concentrations, which resulted in higher strengths (1.2 MPa). However, star shape polymers are not easily found in the market and modifications to the polymer morphology might come with a higher cost.

2.1.4 Solvents and additives

Water and organic liquids can be used as dispersion medium. Organic solvents encompass alcohols, methyl ethyl ketone, ethyl acetate, propylene carbonate, ethylene glycol butyl ether acetate, diethylene glycol monobutyl ether, etc [78]. Normally, mixtures of the different liquids are used to tailor the viscosity, surface tension and evaporation rate. Among the solvents, water has the advantage of being eco-friendly and cheaper as well as not being health hazardous. In fact, most solvents are volatile and release toxic organic compounds [78]. This said, printheads are not regularly suited for water printing due to its high surface tension (72 mN/m, although it is regularly lower due to surface active contaminants) [31, 78]. This can be solved by adding a significant amount of alcohol to the formula (~20 %) [31].

As previously said polymeric liquid binders are the most common type of binder in BJ [15, 27, 31]. Polymers are the binding agents, but in order to modify the properties of the liquid, additives such as surfactants, buffers, crosslinkers, thickening agents, biocides, humectants, visible dyes and defoamers are generally included in the formulations (Table 2.2) [31, 78, 79].

Besides the solvent mixtures, other ways to tune the viscosity are to change the molecular weight of the polymer or modify its concentration [78]. One can also reduce the concentration of one of the ingredients that promotes interactions among the other ingredients, crosslinkers, for example. On its side, surface tension can also be modified with the help of surfactants. However, it is not recommended in BJ, as surfactants give dynamic surface tension properties to the binder [32, 78]. In fact, the surface tension lowering effect of these products only work when surfactant molecules have enough time to migrate to newly formed surfaces. It might not happen in BJ as the time required for a nozzle to form drops and eject them is generally shorter [31].

Table 2.2 Examples of the principal ink ingredients. These ingredients can be used for all the inkjet printing technologies [78].

Ingredient	Example
Cosolvent	2-pyrrolidone, tetraethylene glycol, glycol ether, hydroxyketone, alkyl lactate, acetoacetate, methanol ethanol, or 2-propanol
Pigment	Carbon black pigment (Cabojet 300), Blue 44, Blue 45
Surfactant	Polyacrylate or polysiloxane, non-ionic Surfonol 465, lithium carboxylate anionic fluorosurfactant
binders	SMA 2000, copolymer of maleic anhydride, vinyl aromatic compound, Mace 85-302-1, polyurethane, vinyl chloride, vinyl acetate copolymer
Humectant	Glycerol, diethylene glycol, polyethylene glycols, and propylene glycol methyl ethers
Biocides	1,2-benzisothiazolin-3-one and 2,6-dimethyl-m-dioxan-4-ol acetate
Defoamer	Tributyl phosphate
Buffer	Trizma Base

Crosslinkers are commonly used to increase the mechanical properties of the binder and give more strength to the green bodies [34]. The crosslinks can be physical (coordination bonding, hydrogen bonding, ionic interaction, or van der Waals interaction) or chemical (covalent bond). Chemical crosslinking generally needs an elevation of the temperature to initiate [39]. It makes the process longer but generally results in much stronger green bodies. That said, crosslinking can also be accomplished without a crosslinker additive in some cases (e.g., photocurable resins) [38, 39].

In water-based organic binders, there might be the proliferation of living organisms. That is why biocides might be included in the formula [78]. Additionally, the stability of the binder can be ensured by adding a buffer. pH stability is particularly important when the binder contains polyelectrolytes [78]. Also, to avoid bubble formation during printing, defoaming agents are added. However, these additives lower the surface tension in small local areas of the liquid, which causes deposition defects [78]. Humectants are only used to retard the evaporation of the solvent. This protects the printhead nozzles from clogging [78]. Ethylene glycols are often used as humectants [27, 33]. Finally, dyes or proprietary inks are often used as a visual aid [32, 70]. They allow to do regular printing tests over white sheets and observe the quality of the print. In the case of proprietary inks, as they are designed to be used in the same type of printhead than the binders, they are also composed with the ingredients mentioned above [78].

2.1.5 Binder penetration mechanism

When the binder impacts the powder bed, it spreads on the surface (Figure 2.4 b). This is driven by the kinetic energy from the fall [80]. When this energy equilibrates with the liquid cohesion, the capillary and gravitational forces make the binder penetrate the powder bed (Figure 2.4 c). When the liquid is completely absorbed, it forms a saturated primitive (Figure 2.4 d). All the pores in that primitive are filled with binder. However, the capillary forces make the binder to go further into the powder bed until the pressures of all the air-liquid interfaces are equilibrated (Figure 2.4 e) [25, 28]. Generally, this final primitive has an irregular shape and a saturation ratio of around 60 % [28, 31]. At this point all the liquid is interconnected within the primitive.

As the solvent dries, the liquid disconnects and the capillary force drives the binder towards the necking regions, interparticle contact points (Figure 2.5) [31, 80]. In the case of polymeric binders, as evaporation continues, the binder passes from a solution to a gel to a solid state. The process finishes by the deposition of the binder around the inter-particle contact points [31]. However, if the binder is too concentrated, the ingredients might start depositing onto the particles before the liquid is fully localized at the necking regions due to early precipitation [81].

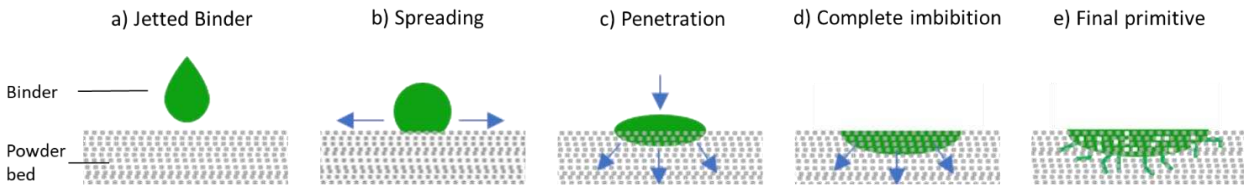

Figure 2.4 Primitive formation mechanism.

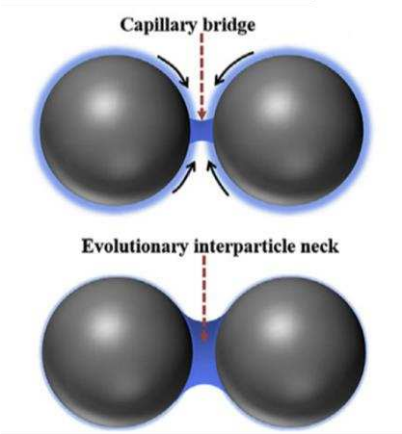

Figure 2.5 Liquid pendular bridge formation [80].

The driving mechanism that pulls the binder to the necking regions is governed by the capillary pressure. This pressure can be written as follows, according to the Young-Laplace equation:

$$\Delta \mathrm{P} = \mathrm{P}_{\mathrm{liq}} - P_{air} = \gamma \left(\frac{1}{r_1} + \frac{1}{r_2} \right) \tag{2.5}$$

where γ is the surface tension and r_1 and r_2 are the curvature radiuses of the bond in the air and liquid side, respectively. For the liquid to be pulled into the necking region, the pressure of the air must be higher than that of the liquid. Equation (2.9) simply highlights that the capillary pressure is higher if the surface tension increases.

Recently, equations more suited for BJ such as eq. (2.6) have been proposed [25, 28]. Eq. (2.6) characterizes the pressure in a powder bed as a function of the surface area of the metallic particles S (surface area/volume), the porosity of the powder bed p and the contact angle θ [28].

$$\Delta P = \frac{S(1-p)\gamma\cos\theta}{p} \tag{2.6}$$

These equations do not take into account the effect of the binder's viscosity. Therefore, the capillary number Ca is also considered as an indicator of the capacity of the binder to undergo a capillary displacement. This dimensionless number highlights the relation between the surface tension and the viscosity η in a capillary flow [28] :

$$Ca = \frac{\mu\eta}{\gamma} \tag{2.7}$$

where μ is the velocity of the fluid. If Ca increases the capillary flow is less favored.

2.1.6 Saturation ratio and binder drying

Saturation ratio (SR) is defined as the ratio between the binder liquid volume and the pore volume of the piece [25, 28].

$$SR = \frac{V_{binder}}{V_{piece}\,(1-\varepsilon)} \tag{2.8}$$

where ε is the powder bed packing density.

When referring to the SR, one must differentiate between the equilibrium saturation ratio and the overall saturation ratio [25]. The equilibrium ratio corresponds to the pore filling level of one drop with respect to one primitive. It is related to the binder interaction with the powder bed and it is specific to every system [25]. On the other hand, the overall ratio, also called binder level [34], corresponds to the pore filling of the total binder volume with respect to the piece pore volume. In this work, SR is used when referring to the overall saturation ratio.

It is an important parameter, as it is related to the final dried binder concentration in the green bodies, which is directly related to green strength. It has been shown that low SR results in weak green bodies [82]. It is also related to resolution. In fact, the drying time, layer thickness and the saturation ratio must be matched. If the SR is high and the drying time, low, an effect called bleeding takes place. The binder migrates outside the desired volume causing piece deformations [28, 82]. It can also happen if the layer thickness is too small for the chosen SR [38]. On the

contrary, excessive drying can cause poor interlayer adhesion, as the binder of the previous layer must be partially redissolved to promote binder permeation between layers and improve green strength [23]. A similar effect occurs with large layer thicknesses, if the depth of the binder penetration is smaller [38]. In addition, over drying can also cause the binder to crack with the pressure applied by the roller when depositing a new layer, but if the binder is too wet, it might stick to the roller [39].

From an economical point of view, faster drying times are regularly preferred, as a binder that dries faster can be printed in higher rates. This can be achieved by using an in-process dryer or by choosing a high drying rate binder. However, the in-process dryer is often preferred even though it makes the printing process longer, as it dries the binder at every printed layer. That drawback is less important than the problems caused by a fast drying binder since it can cause nozzle clogging and uneven binder distribution in the powder bed. [15]. Since the binder can be dried during the printing process, the SR can exceed the pore volume of the piece. It can therefore take values between 40 and 200 % [38]. Despite their importance, these two parameters are often selected by trial and error [34].

2.2 Green strength

2.2.1 Summary of printing parameters' effect on green strength

In the previous sections, an overview of the printing parameters and printing steps of BJ is presented. The parameters influencing the green strength are reported again in this section, merely to give a summary of their effect on green strength and to highlight the complexity of their interrelation.

To ensure proper green formation, the binder primitives must overlap to a certain degree in order to ensure the adhesion between the printed layers and within the agglomerates of one layer [24]. Additionally, the new printed binder must partially redissolve the binder on the previous layer to ensure adhesion. With those conditions covered, green strength can be further enhanced by increasing its density. This can be achieved by increasing the amount of solvent used to print the pieces [24, 29, 40, 83] since the capillary forces applied by the liquid on the particles increase the powder packing density [55, 84]. Additionally, green density can be enhanced by depositing denser

powder beds. This can be accomplished with three methods. First, the powder deposition can be optimized trough parameters such as roller speed, powder layer thickness, roller radius and roller contact pressure [85]. Second, the pores between the particles can be partially filled by using a multimodal size powder, as the smaller particles can fill the interstitial spaces [24, 42]. Finally, powder with spherical shapes result in higher powder packing since they have better flowability [23, 31].

Additionally, the strength of green bodies has been ameliorated thanks to other process parameters such as drying time, saturation ratio and layer thickness [23, 40]. The SR is directly linked to the liquid volume of binder used to print the samples and to the final binder concentration in the green bodies. When increased, this parameter can therefore enhance the powder packing density and the final binder wt. % in the pieces. On its side, the drying time has an impact on the adhesion between layers [23]. In fact, the binder of the previous layer must be partially wet to allow the new binder to redissolve it and form a continuous binder phase trough the printing layers. If the previous binder layer is completely dry, this is more difficult to happen. For this reason, if the binder is too dry when new binder is deposited, poor adhesion between layers is obtained [38]. Finally, small layer thicknesses promote a better binder distribution in depth, which enhances the green strength [38].

It has also ben shown that increasing the binder's polymer concentration and the molecular weight results in higher bodies strength [29, 40, 76]. In addition to the strength obtained with the help of the binder, electrostatic, magnetic and van der Waals forces help to keep together the smaller particles (<1 μm). In addition, irregular shaped particles can increase the strength due to an increase of the friction forces and the presence of more mechanical interlocking between particles [86]. This said, besides the effect of the binder, the impact of these interactions is usually negligible.

2.2.2 Interparticle bonds

2.2.2.1 Onoda's green strength model

In homogeneous materials, stresses can be transmitted through the entire volume. However, green bodies are granular materials held together by interparticle bonds. The bonds in one part of

the piece can break without transmitting the stress to the other bonds. This means that interparticle connections are what gives strength to the pieces, regardless of the individual strength of the particles [86, 87].

In 1976, Onoda [88] built on a previous model [89] and introduced the idea of binder distribution in the interparticle regions. He described three scenarios: the nonwetting state, where the polymer is randomly located on the surface of the particles (Figure 2.6 a), the pendular state, for which the polymer locates at the necking region between particles (Figure 2.6 b) and the coated state, the polymer is evenly distributed on the surface of the particle (Figure 2.6 c). Onoda explained that a binder that does not wet the surface results in a randomly located distribution. If the binder wets adequately the surface (contact angle < 90°), a pendular distribution is obtained. Finally, if the liquid wets adequately the surface, but has a high viscosity, it will preferentially coat the particles. Thus, the coating behavior takes place when the liquid can resist to the capillary pressures. It is worth noting that the pendular and nonwetting states become coating states at a sufficiently high binder concentration. Also, green bodies can be formed in the three cases. However, to maximize strength, the pendular state is preferred over the two others, as in that state, the polymer is entirely used to link particles.

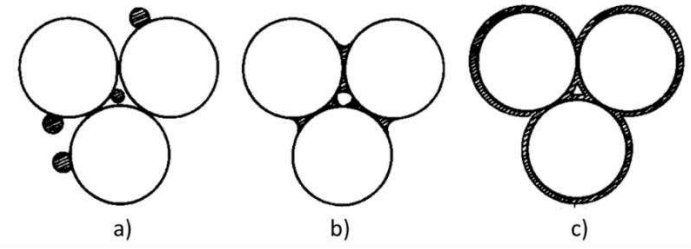

Figure 2.6 Binder distribution types. a) nonwetting binder, b) wetting binder, wetting binder with a high viscosity [88].

Based on geometrical considerations, Onoda estimated the volume of binder between two spherical particles to be:

$$V_{bridge} = \frac{\pi r^2 h}{2} \tag{2.9}$$

where r is the radius of the bond and h, its length (Figure 2.7).

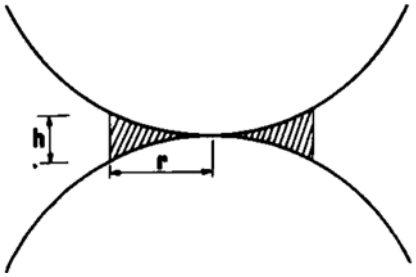

Figure 2.7 Pendular bond geometry model [88].

Additionally, this model proposes a method to calculate the number of bonds in a green body assuming that the particles are spherical and mono-sized:

$$n = \frac{V_{metal}}{V_{particle}} \frac{k}{2} = \frac{V_{metal}}{\frac{4}{3}\pi R^3} \frac{\pi}{2p} \tag{2.10}$$

where V_{metal} is the total volume of metal in the green body p, the volume fraction of pores and $k = \pi/p$ is the average number of neighbour particles around one particle.

Finally, with these and other geometric considerations and assuming that the bonds are all pendular and that the binder is all located at the necking regions, Onoda proposed the following equation to estimate the green strength:

$$\sigma_{green} = \frac{3\sqrt{3\pi}}{8} \frac{1-p}{\sqrt{p}} \left(\frac{V_{binder}}{V_{metal}}\right)^{1/2} \sigma_{binder} \tag{2.11}$$

where σ_{binder} is the strength of the pure binder and V_{binder}, the volume of dry binder in the piece. Pure binder strength can be obtained by performing mechanical tests on samples made of polymer only.

The strength of this model relies on the fact that it highlights the dependency of the green strength on the powder packing, the binder concentration, and the strength of the binder phase. In addition, the estimated values obtained with equation (2.11) are in the same order of magnitude than experimental data [36]. However, this model has been criticized because it does not consider the effect of fracture mechanics. It assumes that breakage occurs when an entire plane of bridges fails simultaneously [87]. For this reason, Kendall et al. developed a model considering fracture mechanics to predict the toughness and Young modulus of green bodies without binder [60, 87].

2.2.2.2 Types of bond failure

Interparticle bridges can fail in two different ways, depending on the affinity between the binder and the metallic powder. If the binder does not adhere adequately to the surface, the bond will break at the interphase (Figure 2.8 b). This is called an adhesive failure. If the interaction between the surface and the binder is strong, the failure will take place at the binder phase (Figure 2.8 a). This failure mode is called a cohesive failure [36, 90]. When the bonds fail cohesively, the strength of the bond is determined entirely by the strength of the binder phase [88]. Consequently, green strength increases with the number and the strength of the interparticle bonds, which is directly related to the final binder wt. % in the piece [36]. On the other hand, when adhesive failure occurs, the strength is determined by the polymer-metal interactions. If these interactions are stronger, the pieces become stronger as well [36].This means that a metal-binder system failing adhesively could be much stronger if the affinity between the materials was ameliorated. However, the toughness, ability to deform without breaking, is increased in green bodies if the adhesion between the polymer and the surface is poor [36].

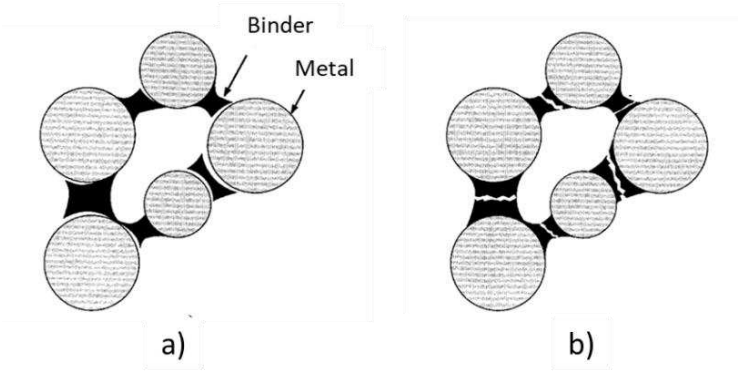

Figure 2.8 Types of failure of interparticle bridges [36]. a) Adhesive failure. b) Cohesive failure

2.2.3 Mechanical tests

2.2.3.1 Compression, diametral and flexural tests

Compression test (CT) of green bodies is mainly done on cylindrical samples [91] [40] [66, 91]. It consists of applying a uniaxial load at a constant crosshead speed. Figure 2.9 presents a typical stress vs strain curve for the compression test of a green body. The curve is divided in three regions. Region A corresponds to the range of stresses where the particles and the binder rearrange. It is an

elastic region characterized by a linear increase of strength. On its side, region B takes place at stresses that cause polymer decohesion. The sample starts to deform permanently. Finally, region C starts at the ultimate green strength. At that point cracks form and propagate through the piece [60].

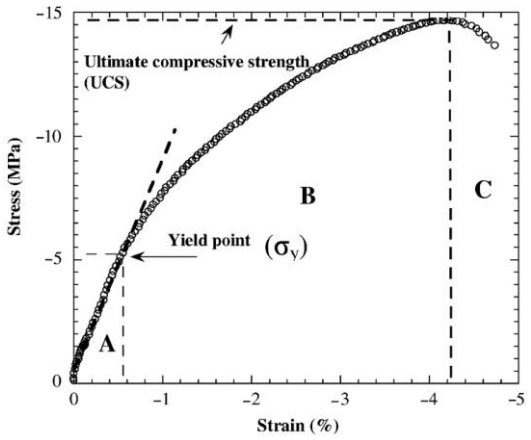

Figure 2.9 Typical stress vs strain curve of a green compression test. Region A: particle rearrangement and binder shear; region B: binder shear and decohesion; region C: initiation of cracks [60].

Standards such as ASTM D695 - 15, ASTM D 3410/D 3410M - 03 and ASTM E9 - 09 can be adapted to test green bodies in compression. The strength of the samples is calculated according to the following equation:

$$\sigma_{CT} = \frac{F}{A_{green}}, \tag{2.12}$$

where A_{green} is the cross-section area of the piece and F, the force. It is to be noted that the maximum strength that a body can handle is the yield strength, strength at which the linear regime ends. After that point, the pieces are permanently deformed. However, it is common practice to present the 0.2 % yield strength as the maximum force a piece can withstand. In fact, the yield strength is usually difficult to find as the transition from elastic to plastic deformation is not clearly defined [92-94], as can be seen in Figure 2.9.

The diametral compression (DCT) test, also called Brazilian or splitting test, is commonly used to measure the green tensile strength [60, 76, 91]. It consists on applying a compression load

in the radial direction of discs. These discs usually have a diameter two times larger than the thickness.Although there is not a standard test method for diametral compression of green bodies, standards ASTM D8289-20, ASTM C496/C496M-17 and ASTM D3967-16 can be adapted to green body testing, even though they are intended to be used to characterize graphite, concrete and rock samples, respectively. Knowing the fracture load, the diameter and the thickness of the sample one can calculate the tensile strength [95].Flexural test (FT) is the only one backed by an ASTM standard (ASTM B312 - 20). That standard suggests doing three-point bending tests on green bodies of dimensions 12.71 mm x 13.75 mm. The specimens can be thin (6.35 mm) or thick (12.70). The tests are accomplished under a load speed of 90 N/min. With the force of fracture, one can calculate the flexural green strength [44]. This said, not all the green flexural strength studies follow this method [36, 68]. Also, in some cases, a four-point bending test was preferred [91].

2.2.4 Strength of green bodies in the literature

The minimum required flexural strength for green bodies to withstand general handling has been suggested to be around 1 MPa [79]. In [68], the authors confirmed that a green body with a flexural strength of 1.27 MPa is strong enough to be handled. They studied this by performing three-point bending tests on 80 mm x 10 mm x 4 mm green bodies made of hydroxyapatite and A-W glass ceramic mixture. They used a water-based maltodextrin binder. However, in [29], the authors estimated that green strength of simple cylinders must be above 0.4 MPa to endure handling and processes such as packing and recoating. In our experience cylindrical samples of 0.33 MPa compressive strength are strong enough to be carefully handled. A strength of 1 MPa is therefore preferred and higher strengths of ~10 MPa are more recommended [79], as higher strengths allow the fabrication of more delicate features. Table 2.3 presents a list of binder - powder systems and their respective strength.

Table 2.3 Summary of binders and green strengths in the literature. CT stands for compression test, DCT, for diametral compression test and FT, for flexural test.

Binder	**Powder material**	**Binder concentration**	**Strength (MPa)**	**Formation technique**

Methylcellulose [60]	Alumina - silica mixture	3.7 wt. % to powder weight	14.5 (CT) 1.06 (DCT)	Extrusion
42 wt.% phenolic resin - 28 wt.% alcohol - 30 wt.% glycol[40]	SS 316L	10 - 100 % inkjet capacity	3.22 - 25.56 (CT) 1.66 - 10.08 (FT)	BJ
PVA [66]	Hydroxyapatite	10 - 30 wt. % to powder weight	1.15 - 5.63 (CT)	BJ (in-bed binder)
Maltodextrin [66]	Hydroxyapatite	30 wt. %	3.70 (CT)	BJ (in-bed binder)
PVP, PVA and polyacrylamide [65]	Hydroxyapatite	1 wt. % water solution	3, 4, 5, respectively (CT)	BJ
Commercial ZB56 binder	proprietary Zcast 501 powder	-	0.26 - 1.26 (CT)	BJ

Table 2.5 Summary of binders and green strengths in the literature. CT stands for compression test, DCT, for diametral compression test and FT, for flexural test (continued).

Binder	**Powder material**	**Binder concentration**	**Strength (MPa)**	**Formation technique**
PAA - glycerol [36]	Silicon, titanium and	2.5 vol. % to powder volume	1.15, 2.08, 7.65, respectively (FT)	BJ

	aluminum oxides	2.4 vol. % PAA - 10 wt. % glycerol water solution		
PVP - Collins Blue ink [41]	SS 316L	5 and 10 wt. % water solutions	50 to 500 N (FT)	BJ
PVA-Maltodextrin [83]	Polymethyl methacrylate	0 to 10 wt. % - 0 to 50 wt. %, respectively	0.2 - 4.35 (CT) 0.2 - 1.16 (FT)	BJ (in-bed binder)
PVP [29]	Lactose-sugar mixtures - silica (40 - 10 - 5 wt. %)	3 - 9 wt. % water solution	0.4 - 1.2 (CT)	BJ
Hydroxypropyl-methylcellulose, PVP [76]	Lactose	5 - 20 wt. % water solution	0.49 - 2.45 (DCT)	Granulation

Several of the studies of green strength are not limited to only one test method and different tests give different strength values. However, the general relation between the studied parameters and the variation of strength is maintained. For instance, Patirupanusara et al. [83] performed compressive and flexural test on polymer green bodies. They obtained an exponential-like increase of strength as a function of concentration in both cases. However, the strength increase of the flexural tested samples was lower. Mao et al. [40] also studied the effect of binder concentration on the compressive and flexural strength of SS 316L green bodies. Their results showed in both cases that strength increased with concentration. Nonetheless, in this study, the shape of the curves was different. The cylindrical samples tested in compression followed an exponential trend whereas the flexural test samples followed a linear increase. In general, compression tested samples are stronger. Therefore, CT is better suited for weak sample characterization.

2.3 Binder selection

As discussed previously, there exist a vast range of materials that have been used as binding agents (section 2.1.3). However, most studies do not include a material selection justification, something that explains why that binder was chosen instead of others. In fact, there exists no algorithm for binder ingredient selection. Additionally, similar to other inkjet applications, several stages of binder development are done based on heuristic considerations [27]. These considerations focus on parameters such as environmental and health risks, printability (viscosity and surface tension), stability in time and at high shear stresses, drying time, powder wetting, green strength and degradation temperature and residues [15, 32, 34, 38, 40, 78]. That said, there exist algorithms and methods to develop the printing process once the liquid ingredients are determined [23, 27, 32].

2.3.1 Ink formulation algorithms

Utela et al. proposed the binder formulation algorithm presented in Figure 2.10. They based this algorithm on two physicochemical properties: viscosity and surface tension. They also considered binder stability in time and redispersion. The algorithm is designed to adjust the properties of the binder to the printhead specifications in order to ensure printability. It is applicable to polymeric binders and binders containing suspended particles.

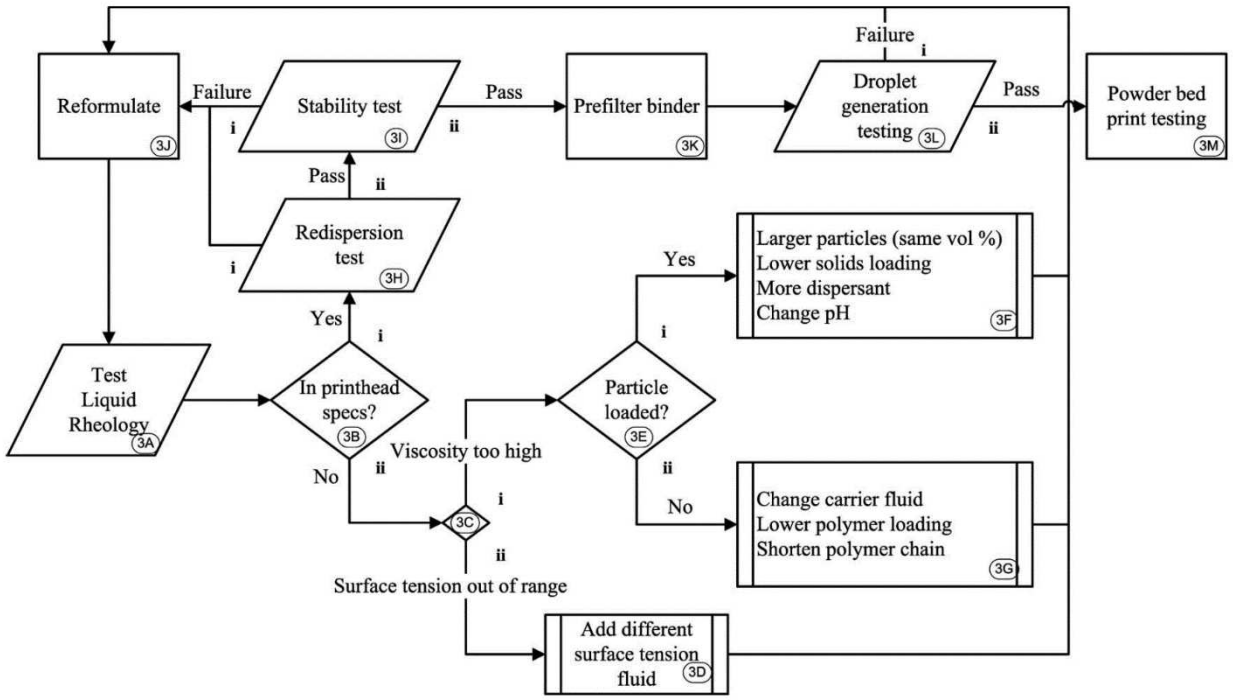

Figure 2.10 Ink formulation algorithm proposed by Uthela et al [32].

Figure 2.10 provides recommendations to adjust the viscosity and surface tension of polymeric binders in steps 3D and 3G. For the surface tension, as previously stated, one must add a higher or lower surface tension solvent. For instance, alcohol can be used to lower the surface tension of water-based binders [31]. With respect to viscosity, a co-solvent can be also used to tune it. Additionally, if viscosity is too high, the binder concentration and molecular weight can be adjusted, as their reduction reduces viscosity as well. This algorithm only considers pH as a selection criterion for binders containing suspended particles. However, it may also influence the viscosity of polymeric binders, as pH might change the interactions between the polymers and the solvents [96].

The algorithm in Figure 2.10 introduces other important considerations such as the redispersion and the stability of the solutions. The authors propose a simple method the ensure binder resolubility: let some quantity of it dry in a watchglass and then rehydrate it with more binder. If the binder redissolves quickly, it passes the test. This selection criterion is controlled by the affinity between the binder ingredients and the solvent. In the case of stability, characteristics such as viscosity, pH, surface tension and optical transmission must be monitored in time. Any

variation of these parameters is a sign of binder degradation. All things considered, this algorithm does not explore the impact of the properties of the fluid on the binder-powder interactions such as powder penetration and interparticle bridge formation. It does not take into account the green part strength either.

In a previous article [31], Utela et al. proposed a benchtop test to assess the amount of binder needed to obtain green bodies with good strengths. It consists of manually mixing different powder: binder ratios and to cast the mixture into bars. The printing tests are done based on the ratio that allows pieces to retain edge definition and to be sufficiently strong to be handled [32].

Another algorithm for ink formulation was developed for the conductive inkjet printing field [27]. The algorithm is presented in Figure 2.11.

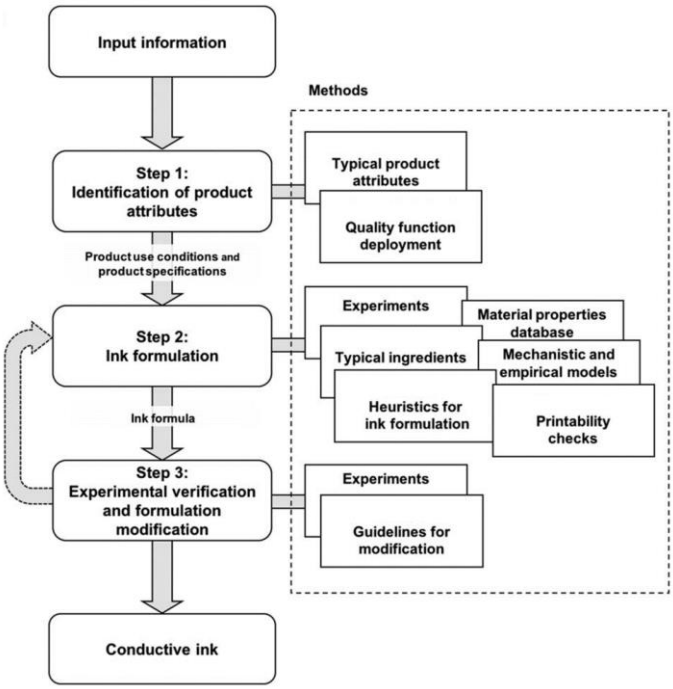

Figure 2.11 Ink formulation algorithm proposed by Tam et al. (adapted from [27]).

The algorithm is very simple, as it comprises only 3 straight forward steps. The main contribution of this work relies on the methods. In step 1, through the use of a quality function deployment matrix, the authors showed that qualitative ink attributes such as “good wettability of the substrate” can be converted to product specifications (i. e. substrate and ink surface tension). In step 2, the authors provide many models that predict the binder attributes. These models coupled

with information found in the literature allow to reduce the experimental needs of ink product development. However, several of these models can not be directly applied to BJ binders since they are suited to characterize inks containing nanoparticles for circuit printing applications. In steps 2 and 3, Tam et al. provide thorough lists of heuristic considerations and problem-solving actions. An example of a heuristic consideration is “a chemical that serves multiple functions is chosen whenever possible”. The problem-solving actions are intended to be applied in step 3, after the printing performance verification. They are a “what to do if” list. To name one example, if cracks form during printing, increase the binder concentration. That said, this algorithm can be adapted to binder formulation developpment. However, it does not include a binder ingredient selection method and evidently, all the binder - powder interactions.

2.3.2 Other selection criteria

Environmental and health risks are principally related to the fumes that can be released by the binder during printing and debinding. This is controlled by the binder’s solvent when printing and by the degradation products, when debinding. Consequently, the solvent can be selected based on its boiling point and polymers can be screened based on data in the literature about the pyrolysis products of the polymers [38]. Experimentally, fume products can be identified with TGA + FTIR measurements [97-99]. Also, the binder residue is one of the most important binder selection criteria [31]. With TGA results in the literature, one can know how much residue a binder lefts behind.

Drying time and powder wetting are related to the dispersing medium. As previously said, drying time must be decreased to allow the printing process to be faster. It must also ensure that the binder dryes before penetrating too deep into the powder [23, 28]. Slow drying might cause oversaturation of the interparticle pores, which results in bleeding (liquid going outside the desired volume), but too fast drying results in poor interlayer adhesion [23]. Therefore, the selected solvent must have a boiling point that allows adequate drying.

On its side, wettability is an indicator of the affinity between the binder and the substrate. It can be estimated studying the binder’s solvents only, as they are the larger phase of the ink. Therefore, the solvent and co-solvents mixture must have a contact angle smaller than 90° with the substrate [27]. Additionally, wetting has an impact on the formation of pendular bonds, in fact if

the binder does not wet the surface, the binder will not deposit at the necking regions[88]. Other selection criteria concerning green strength are polymer concentration, molecular weight and type of bond failure [29, 36, 88]. Preferentially, bonds must be pendular and they must fail cohesively. However, there is no clear method to obtain these conditions.

Finally, since, the binder is subjected to high shear stresses when it is printed [34]. It must maintain its viscosity while being printed, else due to shear thickening or shear thinning effects, the binder can temporally clog the printhead and cause the process to miss some print lines [23].

2.4 Metallic surface

The metal surface chemistry is very chaotic. It is disturbed by the crystallographic orientation (grain distribution), impurities, segregation of the alloy components, uneven oxidation, local electrical fields, etc. [100] All those imperfections create active sites where the reaction with organic groups can take place [101].

In an aqueous medium, the chemistry of the oxide surface is determined by the pH. More precisely, it is determined by the isoelectric point pI, the pH at which the surface charge is zero. If pI is above 7, the metal oxide is a Lewis base and if it is below 7, a Lewis acid. In Figure 2.12, one can see how the pH affects the surface chemistry of different metal oxides: if the surface is charged positively, the group at the surface is mostly OH_2^+. On the contrary, if the surface is negatively charged, the functionality is principally O^-. Finally, a neutral surface would principally be composed of OH groups [102].

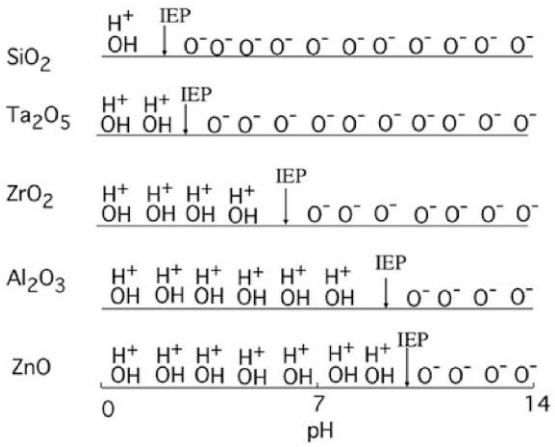

Figure 2.12 Surface charge of different metal oxides as a function of their isoelectric point [102].

2.4.1 Polymer metal interface

As can be seen in the schema of a metal-polymer interface of Figure 2.13, the interface is regularly composed of 5 main layers. The metal is in many cases covered by an oxide layer, then there is always the presence of impurities. After, we find the primer which is a layer made of interfacial agents that promote the adhesion. Finally, there is the polymer layer that can be composed of different types of molecules that will promote entanglement, cross-linking and adhesion [100].

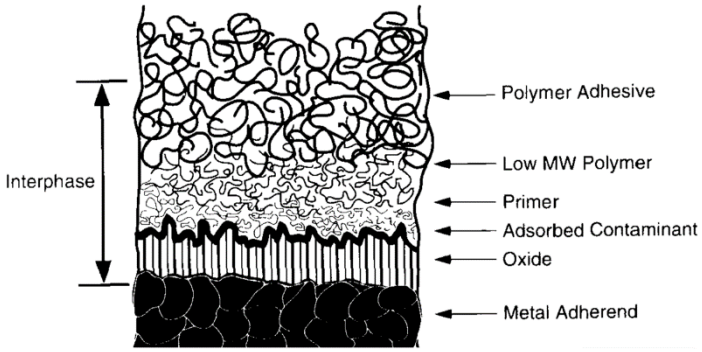

Figure 2.13 Schematics of the polymer-metal surface [100].

Wetting of metallic surfaces by polymer solutions can be explained in terms of surface energy. Metals and metal oxides are high surface energy materials, whereas organic compounds have low energy surfaces [103]. Organic solvents, water and polymers have surface energies below 100 mJ/m^2, while in several cases metals and metal oxides have energy surfaces above 1000 mJ/m^2 [104]. In general, low energy materials adsorb strongly on high energy ones, as surfaces tend to minimize their energy. In fact, the work of adhesion W_a, work required to separate two materials, is governed by the surface energies γ or the two materials [105]:

$$W_a = \gamma_1 + \gamma_2 - \gamma_{12} \tag{2.13}$$

Additionally, γ can be decomposed into a dispersive γ^d and a polar γ^p component [106]. Therefore,

$$\gamma = \gamma^d + \gamma^p \tag{2.14}$$

Finally, the interfacial surface energy in a metal-polymer system can be estimated by the geometric mean of the dispersive and polar components of the two surfaces [106]:

$$\gamma_{12} = \gamma_1 + \gamma_2 - 2\left[\left(\gamma_1^d \gamma_2^d\right)\left(\gamma_1^p \gamma_2^p\right)\right]^{1/2} \quad (2.15)$$

For most materials, the values of the dispersive and polar components are available in the literature.

2.4.2 Properties of stainless steel 316L

Steel is an alloy of iron with low quantities of carbon. Carbon is added to iron to improve its strength. To obtain a stainless steel, one must add around 11 wt. % of chromium [107]. Stainless steel is more resistant to corrosion and rusting than carbon steel since chromium forms a thin self-healing oxide layer that prevents oxygen from penetrating into the metallic bulk. This oxide layer forms within seconds after being exposed to an oxidising environment [108].

There are five main groups of stainless steels: austenitic, ferric, martensitic, austeno-ferritic (duplex) and precipitation-hardened [107, 109]. The difference between those types of SS relies mainly on the composition of the alloy. They can contain nickel, copper, tungsten, molybdenum, manganese, nitrogen, aluminium, etc. in concentrations ranging between 0.1 and 30 wt. % [107]. These additives, can enhance the mechanical properties and the resistance to corrosion in acid, basic or high temperature environments [107, 109].

Table 2.4 SS 316L composition according to ASTM A240/A240M standard

Steel	**Cr**	**Ni**	**Mo**	**Mn**	**N**	**C**	**Si**	**P**	**S**	**Fe**
316L	16-18	10-14	2-3	2	0.1	≤ 0.03	0.75	0.045	0.03	Bal.

SS 316L's typical composition is presented on Table 2.4. It is an austenitic steel, characterised by its high corrosion resistance in a large variety of environments and its high strength [15, 107]. The "L" stands for low-carbon-content, which make it more resistant to intergranular corrosion than regular 316 steel. It is an alloy extensively used in the industry [15]. It can be found in kitchen cookware, surgical tools and automotive and aerospace components [110]. Additionally, it is commonly used for orthopedic devices, as it is biocompatible and less expensive than other biocompatible metallic materials, such as Ti64 [111, 112]. In BJ, SS 316L

has been extensively studied, however, with the exception of [40], there are not much studies about suitable binders for this alloy [15].

2.4.2.1 Surface properties (reactivity)

The passivation layer that forms on stainless steel is only 1 - 3 nm thick [109]. The exact composition of the film depends on the environment and it evolves with it, as there is a constant exchange of chemical species. However, in general terms, the oxide film in austenitic steels is composed principally of chromium oxide (~ 60 %), followed by iron oxide (~ 30 %), then molybdenum oxide (~ 8 %) and finally, nickel oxide (~ 2 %). Within the oxide film, there are concentration gradients. Close to the metal, the composition of the oxide is similar to that of the metal, but at the top, the film is mainly composed of iron oxide (Fe(III)) with a small at. % of molybdenum oxide (Mo(IV,VI)) and then, chromium oxide (Cr(III)) [109, 113]. Additionally, the metallic phase above the oxide film is different from the metallic bulk. It is enriched with nickel. In other words, the surface structure of SS 316L is composed by 4 layers. Going from the metallic bulk to the exterior, there is the nickel enriched zone, the chromium oxide enriched zone, the iron oxide and molybdenum oxide enriched zone and a superficial hydroxide zone [109, 113, 114]. In fact, the surface gets covered by hydroxyl groups at a concentration of 6 to 20 groups per nm^2, if exposed to exposed to air or water [102].

In metallic powders for AM manufacturing, it has been demonstrated that parameters such as particle size and atomization method have an impact on the passivation layer composition and thickness. Recently, the composition of SS 316L powders produced by gas atomization, water atomization and vacuum induction melting inert gas atomization, were compared. In general, The powders surfaces were mainly composed of iron oxide with submicron chromium, manganese and silicon oxide precipitates [115]. These oxides appear to be darker circular marks on SEM images.

Therefore, the charge of the SS surface depends on the isoelectric points of its alloy elements present in the surface. Table 2.5 contains the values of the isoelectric points of the metal oxides of interest. The pI values change slightly depending on whether the measurement was made on an oxide passivation film or a bulk metal oxide. Additionally, the values in the literature of SS 316L vary a lot (between 2.8 and 8.5). The value of 8.5 seems more reasonable as the main surface component is iron oxide and its isoelectric point is the most elevated, between 7 and 10. This means

that the surface is positively charged at low pHs and as pH increases, there start appearing negatively charged surfaces when the pH surpass the isoelectric point of Cr, Mn, and Mo oxides. Such is the case of a neutral environment, where pH = 7: the surface is still mostly positive, but the places with Cr, Mn, and Mo oxides precipitates are negatively charged. This said, some studies report the stainless steel surface to be negatively charged at neutral pH [108, 116].

Table 2.5 Isoelectric points (pI) of the metal oxides present at the SS 316L surface.

Oxide	**SS 316L**	**MoO_3**	**Cr_2O_3**	**MnO_2**	**Fe_2O_3**
pI	4.2 - 5.2 [102]	1.8 - 2.1[102]	6.2 - 6.3 [102]	4.7 - 4.8 [102]	7.5, 8.7 [102]
	5.8, 8.5 [117, 118]	2.5 [117]	5.2–5.3* [102]	4 [117]	9.8, 10* [102]
			6.7 [117]		7 [117]
	2.8 [116]				

* Values measured on the oxide passivation films of metals.

A common method to analyze the adsorption of a binder onto a metallic surface consists on placing a small quantity of metallic powder into a container with binder. The mixture is placed on a centrifuge. After being centrifuged, the powder is separated from the binder. The variation in concentration in the binder solution between the initial binder and the final binder is considered to be the amount of binder that was adsorbed. This method allows to measure the amount of binder adsorbed onto the powder surface in mg/m^2 [36, 61, 119].

2.5 Polymer properties

2.5.1 Concentration regimes in polymer solutions

In solution, polymers take the conformation of a random coil, a chain where the monomers are randomly oriented. The space occupied by the polymer can be described by the radius of gyration, R_g (Figure 2.14). It consists of the radius of a sphere, centered at the center of mass of the polymer, that encloses roughly the entire chain [77]:

$$R_g \cong bN^{\nu} \tag{2.16}$$

where b is the length of one monomer, N, the number of monomers and ν, the Flory exponent. This exponent is a function of the solubility of the polymer in the dispersing medium. In a good solvent, a polymer tends to unfold and will have a Flory exponent of 3/5. On the other hand, a polymer in a bad solvent tends to occupy the lowest possible volume, so ν =1/3 [77]. These two conformations are called free draining coil and non-free draining coil, respectively [120].

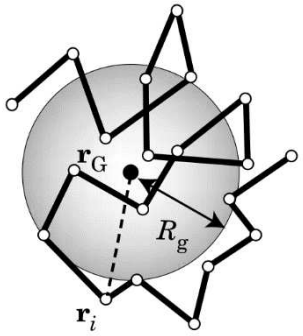

Figure 2.14 Radius of gyration in the bead-stick model [77].

In dilute solution, polymer chains have little interactions with each other. They behave as isolated spheres [121]. As concentration increases, the solution reaches the overlap concentration c^* where the spheres are all packed in the liquid and the polymer chains start to interpenetrate. Solutions at concentrations lower than c^* are called dilute and higher than c^* are called semi-dilute. In a semi-dilute regime, the polymer chains are entangled, which results in a viscosity increase. At even higher concentrations the solutions become concentrated. The concentration at which the transition from semi-dilute to a concentrated regime is regularly denoted c^{**}. At this state, the polymer chains are highly entangled, which significantly reduces their mobility.

Experimentally, the transition from c to c^* to c** can be found by measuring the viscosity of the solution at different concentrations. The transitions occur when the power law of the concentration versus viscosity curve changes of slope [29, 122]. The transitions depend on the type of polymer and its molecular weight. For example, the transition from c to c* occurs at a 14 wt. % concentration for a low molecular weight PVA solution [123] while it takes place at 0.2 wt. % for a 5 Mg/mol PAA solution. [124]. Recently, the overlap concentration has been proposed as the

upper concentration limit for printability in BJ [29]. For a water-based PVP 25k binder the overlap concentration takes place at ~7 wt. % [29]. The values of c^{**} are also highly dependent on the type of polymer and its molecular weight [121]. Studies have found that this transition take place around 15 vol. % and 21 vol. % for poly(methyl methacrylate (600 kg/mol) solutions [125] and around 0.25 vol. % for polyethylene (28 kg/mol) solutions [126]. The transition from c^{*} to c^{**} can also be found with the help of small angle neutron scattering [125]. With that spectroscopy technique, the radius of gyration of the polymers in solution can be found. The transition takes place when R_g stops decreasing with concentration.

In concentrated solutions, where polymers are highly entangled, the chains can be modelled as being contained in blobs [77]. These are spherical regions where a certain number of monomers of one chain are contained. The surface of the sphere is defined by the places where entanglement takes place. In other words, the diameter of a blob is defined as the average distance between entanglements [121]. In Figure 2.15, one can se a schematic of a semi-dilute solution. In the zoomed image, the large circle designates the region defined by the radius of gyration, the smaller circles are blobs and the black dots, entanglement points. The diameter of the blob ϵ, also called correlation length, is a function of the monomer length and the density of the solution [77]:

$$\epsilon \cong b^{-1/(3\nu-1)}\rho^{-\nu/(3\nu-1)} \tag{2.17}$$

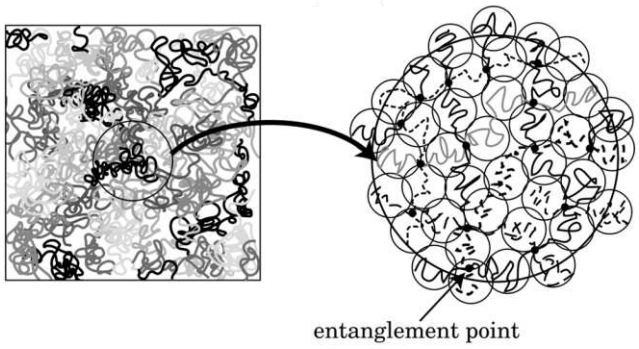

Figure 2.15 Conformation of a highly entangled polymer solution [77].

In BJ, the binder passes through all those concentrations. It is generally a dilute solution (< 7wt. %) when it is printed but goes through the semi-dilute and the concentrated regimes (~20 vol. %), as the solvent dries.

2.5.2 Solubility parameter

The solubility parameter approach, also called Hildebrand approach, is very useful to estimate the compatibility between a polymer and a solvent. The strength of attraction between the molecules in solution can be characterized with the cohesive energy density δ^2 (CED), where δ is the solubility parameter [120]. It can be estimated with the following equation:

$$\delta = [(\Delta H_v - R_c T°)V_m]^{\frac{1}{2}} \tag{2.18}$$

Were ΔH_v is the molar enthalpy of vaporization, R_c, the universal gas constant, $T°$, the temperature and V_m, the molar volume [120].

2.5.3 Polymer mechanical properties

Contrary to metals and ceramics, polymers have viscoelastic properties. This means that polymer chains simultaneously exhibit viscous and elastic responses to varying degrees. For this reason, their response to stress depends on the rate and period of loading [120]. Their properties are also highly dependent on temperature as the mobility of the chains can change drastically depending on the state of the polymer: crystalline, amorphous or rubber (Figure 2.16).

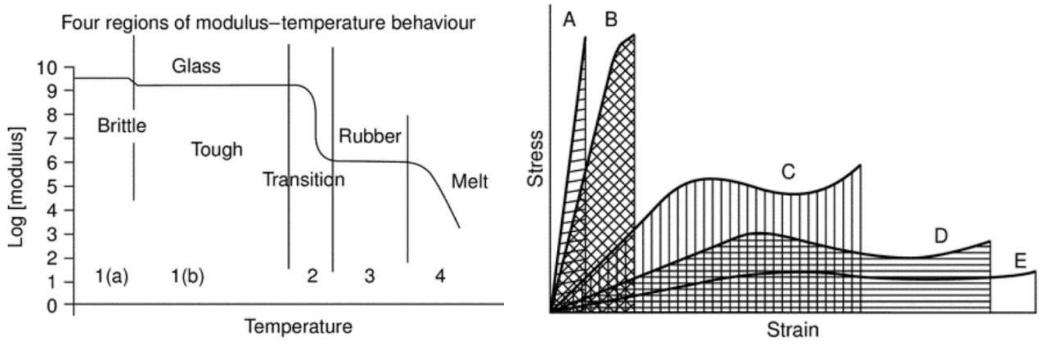

Figure 2.16 a) Modulus regimes as a function of temperature. b) Typical stress - strain plots for different types of failure: brittle (A); brittle-ductile (B); ductile-brittle (C); ductile (D); and rubber (E) [127]

2.5.3.1 Effect of the molecular weight

Mechanical properties of polymers increase with increasing molecular weight (M_w) [103]. The general trend can be observed in Figure 2.17. Point A corresponds to the minimum M_w needed to give significant strength to a given structure. From that point, strength increases quickly up to point B, where it starts to increase slowly. Finally, after point C, there is no more increase, a limit value is reached [128]. This behavior is related to the capacity of the polymer to entangle. Entanglement plays a big role at relatively low M_w, but after a given value, it does not make a big difference. Moreover, there is a minimal molecular weight, called molecular weight for entanglement M_e before which the polymer phase has no significant cohesive strength [129].

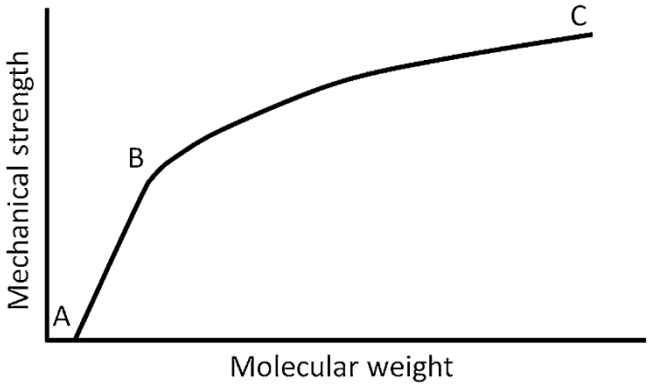

Figure 2.17 Polymer mechanical strength dependence on molecular weight [128].

2.5.4 PVA PVP PAA properties

This section overviews the properties of the three polymers used in this study: polyvinylpyrrolidone (PVP), polyvinyl alcohol (PVA) and polyacrylic acid (PAA). Their molecular structure is presented in Figure 2.18.

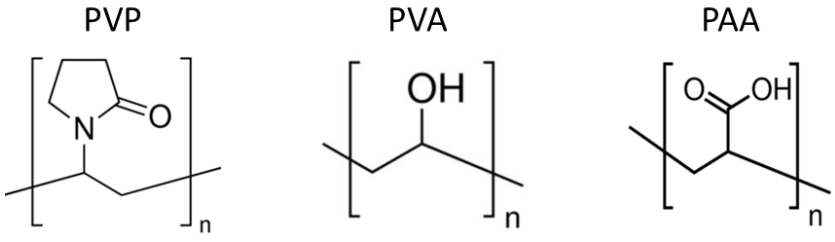

Figure 2.18 Molecular structure of PVP, PVA and PAA.

2.5.4.1 PVA

Polyvinyl alcohol (PVA or PVOH) is a water-soluble polymer with biodegradable and biocompatible properties [130]. It is an excellent film former, emulsifier, stabiliser and adhesive [131]. In addition, it has excellent chemical and thermal stability [132]. Thanks to these properties, it has ben used in the health, agricultural, paper, textile, and food packaging industries. To name some examples, it can be used to enhance the mechanical properties of thin films and as a compatibilizer between other polymers and hydrophilic substances [132]. PVA degradation occurs between 160 °C and 450 °C and only 4 % of its weight remains as carbon residue at 800 °C [133]. In binder BJ, it has been used to fabricate titanium, iron, calcium polyphosphate, Ti-TiB2 composites and metal oxides [38, 47]. Additionally, it has been used to print bone scaffolds of hydroxyapatite [65].

PVA is obtained by the hydrolysis of polyvinyl acetate. It is a process where the acetate groups (CH_3COO-) are replaced by hydroxyl groups (-OH). Typically, PVA is commercially available with different hydrolysis levels, between 80 and 99 % [134]. The hydrolysis level changes the physical and chemical properties of the polymer, as it is in fact a copolymer (Figure 2.19) [132].

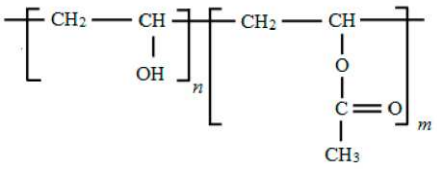

Figure 2.19 Structure of partially hydrolyzed polyvinyl acetate [132].

The acetate groups are hydrophobic while the hydroxyl ones are hydrophilic. As a result of this hydrophilic-hydrophobic configuration, PVA has some unique properties. It is soluble in water, but insoluble in most organic solvents [134]. In fact, increasing the hydroxyl content increases the solubility of the polymer in water. However, a PVA fully hydrolyzed is harder to dissolve than a partially hydrolyzed one due to a higher crystalline arrangement [131]. The high strength of PVA comes from the formation of hydrogen bonds between the hydroxyl groups [131, 132]. This capacity to form crosslinked networks confers it a semicrystalline structure. Therefore, higher hydroxyl group content results in higher crystallinity [131]. Additionally, PVA is a non-specific adhesive. On one hand, the hydroxyl side groups allows it to bind with hydroxylated or protonated

oxide surfaces trough hydrogen bonding [135]. On the other hand, its acetate group allows it to bind to hydrophobic surfaces [131, 136].

2.5.4.1.1 PVA and Borax

The addition of small quantities of crosslinker to the binder can greatly increase the strength of the green bodies. Crosslinkers create a polymer network by linking one or more chains together via covalent or physical bonds. However, they can significantly change the rheological properties of the binder. In fact, interactions between the polymers and ions in solution is not the same depending on their concentrations [137]. In the case of the PVA-borax system, borax discociates into three species [138]:

$$Na_2B_4O_7 + 7H_2O \rightleftharpoons 2B(OH)_3 + 2B(OH)_4^- + 2Na^+. \quad (2.19)$$

Only the borate ion ($2B(OH)_4^-$) interacts with PVA to form a di-diol complex [138]. The diol complexation takes place in two steps [137].

$$P + M \rightleftharpoons PM \quad (2.20)$$

$$PM + P \rightleftharpoons PMP \quad (2.21)$$

where P is a diol (in this case, two hydroxyl groups of the polymer orientated in the same direction), M is a metal ion (or metalloid ion, such as boron), PM is a diol-complex, and PMP is a di-diol complex. Since the borate ion is negatively charged, the complexation sites repel each other causing the polymer chains to unfold, and the number of crosslinks to increase slowly. This means that even if the polymer is neutral, it can behave as a polyelectrolyte in the presence of a crosslinker.

The sodium ions are another reason why the response of the system is not linear. When the concentration of these ions is sufficiently high, they cause an electrostatic shielding effect [139]. As a result, the number of crosslinks increases but this is not completely reflected in the viscosity of the solution, as the chains do not unfold. This shielding effect is present in the system at the solution state, but also in the gel state, when the solution is dryer [139, 140]. One can exploit this effect by adding small quantities of salt to the solution. Doing so, allows for the viscosity to be adjusted to printable levels, despite higher crosslinker concentrations. Nevertheless, if the added salt exceeds a certain concentration, the system segregates [141], ruining the crosslinked network.

2.5.4.2 PVP

PVP, also called polyvidone or povidone, is highly soluble in water. It is a biocompatible, non-ionic, hygroscopic, amorphous, synthetic polymer. It has been used in wet granulation processes as a binder with concentrations between 0.5 and 10 wt. % [142, 143]. Due to its ability to adsorb and desorb active pharmaceutical ingredients, it is used for the preparation of drug tablets [29, 142]. Some other uses are complexing agent, dispersant, film former, suspending agent, and solubilizer [143, 144]. It decomposes at temperatures between 380 and 500 °C and it leaves a residue of 4 to 5 wt. % at 550 °C [145]. Interestingly, its initial degradation temperature decreases with molecular weight, but the final residue is the same for a wide M_w range (8 k - 1.3 M) [145]. In binder jetting, it has been used for ceramic and pharmaceutical tablet manufacturing [71, 72, 74, 146] as well as in hydroxyapatite printing for bone scaffolds [65].

PVP is composed of a hydrophobic alkyl backbone, hydrophilic pyrrolidone side groups and hydrophilic hydroxyl end groups [144]. Its side group contains two electron donating atoms (O and N). Therefore, it is composed of a highly polar amide group (-NC=O) and two nonpolar groups: methine (=CH−) and methylene (-CH_2-) [144, 147, 148]. This configuration makes PVP soluble in polar solvents like ethanol, methanol, IPA, and butanol [143]. The carbonyl group (-C=O) is the most reactive site of PVP since its nitrogen atom's reactivity is reduced due to steric constrains [148]. Thus, the carbonyl group allows this polymer to form hydrogen bonds and coordination bonds on positively charged surfaces[144]. At high pHs, the metallic surfaces get more negatively charged, which decreases the capacity of PVP to adsorb [149].

2.5.4.3 PAA

PAA is a water-soluble polyelectrolyte. It is biodegradable, non-toxic, and biocompatible. It has low mechanical properties. However, it can be crosslinked to ameliorate its strength [36, 150]. Being a polyelectrolyte, it shows pH-responsive properties. This properties make it a good candidate to be used as ophthalmic, oral and transdermal site-specific or feedback-regulated drug delivery [150-152]. Additionally, it has been used as emulsion stabilizer and nanoparticle coating agent [150]. It decomposes at temperatures between 150 °C and 450° C and leaves around 13 wt. % of carbon residue at 800 °C [153]. In BJ, it has been mostly used to print ceramic materials [36, 57], but it has been proposed for metallic printing too [74].

The carboxylic group (-COOH) in PAA can be ionized according to eq. (2.22).

$$RCOOH \rightleftharpoons H^+ + RCOO^-. \quad (2.22)$$

The forward reaction becomes more favorable as the pH of the solution increases [96]. This phenomenon confers PAA an "on-off" behavior. Uncharged carboxyl groups interact by forming hydrogen bonds whereas charged groups experience ionic interactions [154]. The transition from one behavior to the other takes place around the acid dissociation constant value (pK_a) of the carboxylic acid (pH∼5) [96, 154]. In water solution, this behavior translates to a conformational transition. Below that pH, the PAA chains are folded and have a globule-like conformation. After pH = 5, the chains are more elongated in an open coil conformation due to the repulsion between the negatively charged functional groups and the stronger interaction with the water molecules [96]. The elongation of the molecule increases the viscosity of the solution.

The adsorption of PAA into metal oxides depends on the acid-base relation between the polymer and the surface, as PAA is known to react with positively charged surfaces [36]. The carboxyl group can interact with the metal oxide in 5 different ways. As depicted in Figure 2.20, it can form electrostatic bonds, hydrogen bonds and coordination covalent bonds [118, 155].

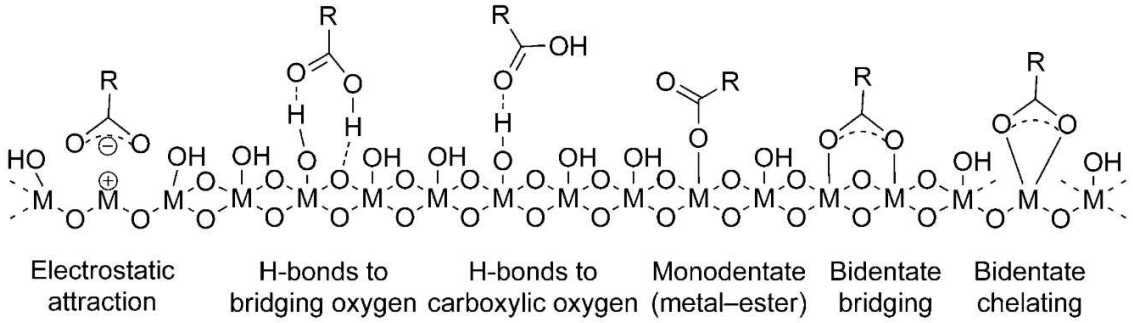

Figure 2.20 Binding mechanisms of the carboxyl group on metal surfaces [155].

CHAPTER 3 OBJECTIVES, MATERIALS AND METHODS

3.1 Objectives

As the literature review reveals, green strength is extremely important, as it limits the capacity of producing parts with thin features. In fact, if the pieces are not strong, these features can be easily crashed or deformed when moving, inspecting and de-powdering the green bodies. Green strength is a function of the characteristics of the liquid organic binder used in the printing process. However, binder design can be overwhelming because of the large amount of possible ingredients and the large number of constraints imposed by the printing process parameters. Although there exists methods and criteria to select a binder, they mostly focus on the printing process requirements and not on the interactions between the binder and the particles. As a result, there is a lack of understanding concerning what gives strength to the green bodies and how.

Therefore, the main objective of this work is to establish guidelines for the selection of binders for BJ based on the polymer-polymer and metal-polymer interactions giving strength to green bodies. This main objective will be fulfilled thanks to the following specific objectives:

1. Develop a method to test the mechanical properties of green bodies made in laboratory conditions without the use of a BJ printer.
2. Determine the relation between binder concentration and green body strength for different binders.
3. Evaluate the impact of crosslinking additives, molecular weight and polymer functionality on the strength of green bodies.

3.2 Materials and Methods

3.2.1 Materials

3.2.1.1 Powder

Stainless steel 316L powder with average diameter of 13 μm was provided by Sautech Technologies and used without any treatment. Back scattered electrons (BSE) scanning electron microscope (SEM) images of the powder can be observed in Figure 3.1 and Table 3.1 contains its

composition. The density of the pure metal is 7.9 g/cm^3 and the surface mean diameter $D21$=15 μm.

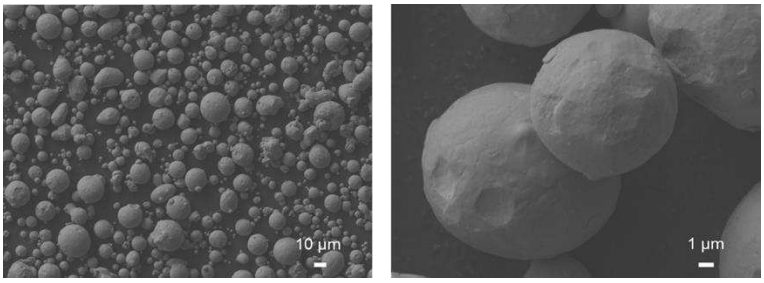

Figure 3.1 BSE SEM images of the SS316L powder.

Table 3.1 Composition of the SS 316L powder (see also appendix B)

Element	**Cr**	**Ni**	**Mo**	**Mn**	**N**	**Si**	**C**	**P**	**O**	**Fe**
At. %	17.13	10.22	2.42	1.28	0.1	0.22	0.03	0.02	0.075	Bal.

3.2.1.2 Polymers and additives

Three different polymers were used in this study: polyvinylpyrrolidone (PVP), polyvinyl alcohol (PVA) and polyacrylic acid (PAA). These polymers were selected as they have been used previously as binders in binder jetting and other manufacturing techniques and are thus useful to gain access to comparative data (section 2.2.4). Additionally, they can be used to produce ecofriendly binders as they are soluble in water [78]. Water is therefore the dispersing medium used in this study. It has good wetting properties on SS316L. In fact, the contact angle between water and stainless steel is lower than 90 °. It is around 54 ° [156].

PVP 360k, PVP 40k, PVP 10k, PVA (low M_w and low hydrolysis) and PAA 100k 35 wt. % water solution, were purchased from sigma-Aldrich. Borax was purchased from Millipore sigma and NaOH from Fisher Scientific. All these materials where used without further purification.

Most of the products previously enumerated were used to study the impact of binder concentration on the green bodies. However, PVP 360k, PVP 40k and PVP 10k were used to assess the impact of molecular weight on the strength of green bodies since PVP was the polymer most available in different molecular weights among the polymers in use. Also, PAA, being a

polyelectrolyte, was selected to analyze the impact of pH on green strength. NaOH was used to adjust the pH of PAA binders and Borax to study the effect of a crosslinking agent on PVA + ink binders. Table 3.2 relates the different polymers and additives to the studied variables.

Table 3.2 Summary of polymers and additives' use and their concentrations range in solution.

Studied effect	Polymers	Concentration range in solution
Concentration	PVA (low M_w and low hydrolysis), PVP 40k, PAA 100k 35 wt. % water solution	3 - 50 wt. %
Molecular weight	PVP 360k, PVP 40k, PVP 10k	5 wt. %
PH	PAA 100k 35 wt. % water solution, NaOH	5 wt. % 0 - 3 wt. % (NaOH)
Ink	PVA 9-10k (80 % hydrolyzed), PVP 40k, PAA 100k 35 wt. % water solution, Borax	2 - 20 wt. % 0 - 0.3 wt. % (Borax)

3.2.2 Binder preparation and characterization

Binders with polymer concentrations ranging from 3 wt. % to 50 wt. % were prepared. The polymers were added to DI water and stirred with a magnetic stir bar for 1 - 24 h. The mixtures were held on a hot-water bath at 60 ° C during stirring to accelerate the dissolution process. Finally, the binders were filtered with 0.45 μm Millipore MIL-SLHV033RB filters, except for the 50 wt. % binder that was too viscous for the filters.

It is common use in binder jetting to add an ink or a dye to the binders because it allows the user to perform quick visual assessments of the printing performance of the binder [32, 41, 70]. In order to assess the impact of a commercial ink on the binders' performance, another set of binders

were prepared. In addition to the polymers, this batch contained 1 - 15 wt. % water-based ink. Once the polymer was dissolved, the ink was added, and the mixtures were stirred for an additional 15 min.

The density of the binders was measured by micro-pipetting 0.33 ml of binder (+/- 0.003 ml) and weighting it on a microbalance ((+/- 0.0001 g). An average and its 95 % confidence interval (95% C. I) were calculated using 5 measurements. The dynamic viscosity of the binders was measured with an Anton-Paar MCR501 rheometer, using a DG26.7 test geometry and a C-PTD200-SN81036684 Pelletier module (23 °C). The measurements were done in rotation with decreasing shear rates (1000 - 0.01 s^{-1}). Surface tension was measured with a Data Physics tensiometer OCA 15 EC by the pendant drop technique. Finally, to study the effect of pH in PAA binders, titration with a 0.1 mol NaOH solution was realized.

3.2.3 Sample formation

Samples were prepared with an out-of-printer approach in order to bypass the optimisation of printing parameters for every binder and to avoid the printhead limitations concerning viscosity and surface tension. This avenue allows to separate the printer parameters' impact on the green bodies' properties from the fundamental interactions. It also allows to study the full range of final dried binder concentrations in the green body, from 0 to 100 wt %. Most of the works exploring binder concentration in binder jetting are limited to small concentration variations due to the constraints of the printhead and the binder's printability [29, 40, 83]. Thus, this approach is not an analogy to the printing process. It is a model work that facilitates the analysis of the interactions of the binder and the metal particles and helps screen various binders. In our case, safety regulations prevented the installation of a BJ printer at Polytechnique Montreal. In fact, due to the manipulation of large quantities of powder, BJ printers must be enclosed with a ventilation system and HEPA filters (300 nm) to avoid the inhalation of ultrafine particles [157]. That said, this method allows companies to keep the printer free for production while developing new binders.

The sample preparation follows the steps in Figure 3.2. First, the binder and the metallic powder are mixed on a crucible until the formation of a malleable paste (Figure 3.2 a). The paste is then put into the mould, which gives it a cylindrical shape (1 cm of height, 1 cm of diameter). The mould consists of two 3D printed PLA pieces (side walls) and a microscope slide (bottom

support). These pieces are held together with an elastic band (Figure 3.2 b). Once the paste is molded, it is dried in an oven at 60 °C for a day. The piece is then demoulded (Figure 3.2 c).

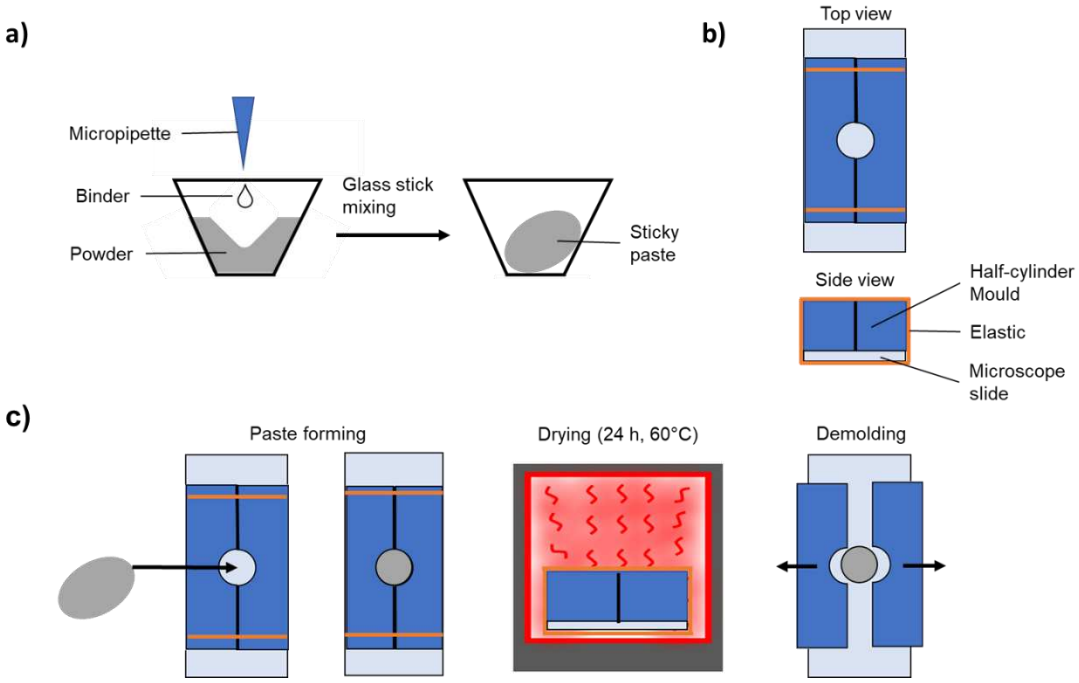

Figure 3.2 Green body preparation schematic: a) paste preparation, b) mould assembly and c) sample preparation.

Here, a distinction must be made between the concentration of the binder and the green concentration. The binder concentration is the polymer concentration in the liquid solution:

$$C_b = \frac{m_{polymer}}{m_{solvent} + m_{polymer} + m_{additives}},$$

while the green concentration is the amount of solid polymer in the piece, after the evaporation of all the liquid:

$$C_g = \frac{m_{polymer}}{m_{piece}},$$

where m is the mass.

Depending on the C_b values and their corresponding viscosities, the first step (Figure 3.2 a) is modified. Low C_g samples were made with C_b values between 3 and 35 wt. %. In such case, the green bodies were made by adding 0.33 ml of binder solution to 5 g of powder. Binder volumes

were measured with a micropipette and the powder weight was measured with a microbalance. This resulted in C_g values between 0.2 and 2 wt. %. Note that C_b values below 3 wt. % were not used, as they resulted in green bodies that broke during the demoulding step.

For the medium C_g samples, a $C_b = 50$ wt. % was used. The proper amount of binder solution was added to the powder by weight, using a microbalance, as the binder's viscosity was too high to use a pipette. This resulted in a C_g value of 5 wt. %.

Green bodies with high C_g (50 wt. %) were prepared by hand-mixing the binder ingredients and the powder in a crucible. In other words, the binder was not prepared as a solution. The ingredients were all manually mixed with the powder at the same time. Once moulded, dried and demoulded, these samples were heated in a convection oven (Precision Freas 625S Oven from Thermo Scientific) to sinter the polymer granules that were not dissolved during the hand mixing stage. These sampled were held at 60 °C for 1 h. Then, the temperature was increased in steps of 10 °C every 10 minutes up to 180 °C (90 % the melting temperature of PVA). The oven was then turned off to let the samples cool down (30 min).

Finally, pure polymer samples were obtained with a similar technique as that of the 50 wt. % green concentration samples. To form the paste, the polymer granules were hand-mixed with water (or water + ink) in a crucible without any metallic powder. Once demoulded the samples were heat treated to sinter the polymer: 60 °C for 1 h, followed by steps of 10 °C every 10 minutes up to 190 °C before and a cool down of 30 min.

The maximum temperature of the heat treatment of the 50 wt. % green concentration samples was lower than that of the pure polymer samples because the metallic particles improved the heat distribution in the piece. If these samples were held at higher temperatures, the polymer would completely melt. Table 3.3 summarizes the paste formation techniques and indicates the binder concentrations (C_b) used and the final green concentrations (C_g) obtained.

3.2.4 Mass and dimensions

The mass and dimensions of the green bodies were measured with a caliper (+/- 0.01 mm) and a microbalance (+/- 0.0001 g). Measurements were repeated 3 times for every sample. These results were used to calculate the density of the green bodies and to define its 95% C.I. The densities

of pure SS316L (7.9 g/cm^3) and pure PVA (1.27 g/cm^3) were used as references to calculate the relative density.

Table 3.3 Summary of C_b, C_g and paste compositions.

Paste composition	C_b	C_g
0.33 ml of binder + 5 g of powder	3 - 35 wt. %	0.2 - 2 wt. %
0.56 g of binder + 5 g of powder	50 wt. %	5.35 wt. %
2.5 g polymer granules + 2.5 g metal + water*	-	50 wt. %
3 g polymer granules + water* + 0.33 g of ink**	-	100 wt. % (without metal particles)

* Enough water to form a malleable paste.

** Samples were made with and without ink. The concentration of the ink was 1-15 wt. % with respect to $m_{polymer}$.

3.2.5 Mechanical test

The samples were tested in compression with an MTS Insight electromechanical testing system with a strain rate of 1 mm/min and a load cell of 1kN, 20 kN or 50kN, depending on the green strength. The tests were done on 3 replicates or more (N ≥ 3).

The compression test was chosen among the different mechanical tests because it can be realized with the simpler geometry. Rectangles for flexural tests, dogbones for tensile tests and discs for Brazilian tests are more difficult to obtain by this method because of two reasons. First, the moulds would be bigger, so the amount of paste needed to fill it would be larger, which makes the preparation more difficult to conduct by hand. Second, the mould consists of two sides walls and a bottom support. This means that the top surface of the samples is exposed to air. If this surface is larger, which would be the case with the geometries of the other tests, the smoothness and flatness of the surface would be much more difficult to retain due to the paste consistency. In the same line

of thoughts, if the mould is too deep, it would be more difficult to avoid the presence of bubbles trapped in the paste. Additionally, green bodies are mostly subjected to compression when they are being handled, as they can be squeezed by the hands or fingers.

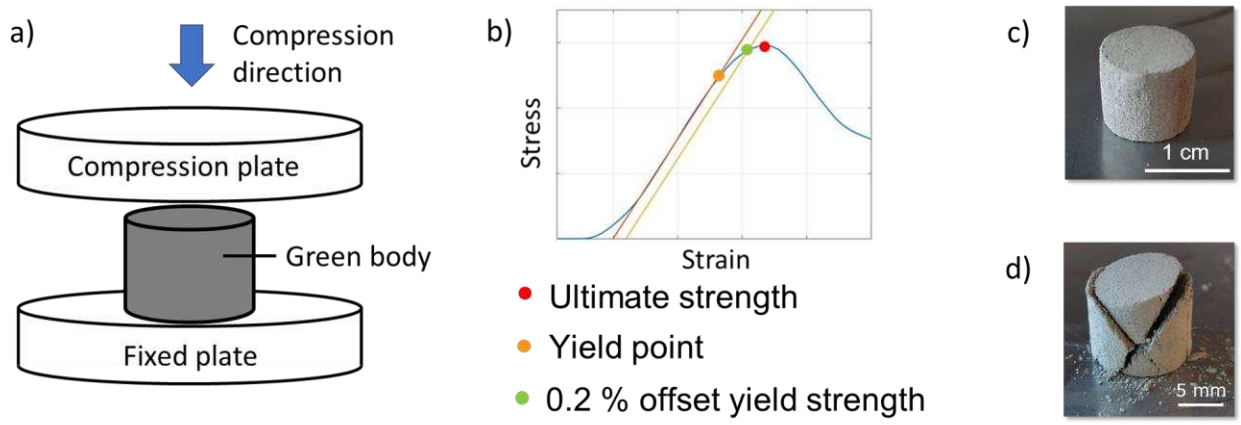

Figure 3.3 Green body strength analysis by compression test (N ≥ 3): a) mechanical test schematic, b) data analysis schematic, c) green body before compression and d) green body after compression.

From the compression test data, the 0.2 % yield strength was calculated (Figure 3.3) and a 95% C.I. was defined. The 0.2 % yield strength was preferred to characterise the green strength over the elastic limit and the yield point because those parameters are difficult to find, as the green bodies didn't show a clear transition between elastic and plastic behavior [92-94]. The 0.2 % offset strength gives a value with a smaller confidence interval. This value was also preferred over the ultimate strength since it is directly linked to the limit where the green body starts deforming permanently. This means that a piece that bears a load higher than that of its 0.2 % yield strength is already broken. Thus, the maximum load that a green body can handle should be estimated using the 0.2% yield strength and not the ultimate strength.

3.2.6 SEM

SEM images were taken in BSE mode to analyse the interactions of the binder with the powder and the failure mechanisms. The images were taken with a JEOL JSM 7600F microscope, a potential of 5 kV, a working distance between 13 and 17 mm and an emission current of 219.2 μA. Only in the case of high concentration PVP samples (> 1 wt. %), the charging effect forced

the use of an electroplated gold film. In all the other cases, no surface treatment was required. Therefore, the images were all taken on 3D untreated surfaces. The surfaces were not smoothened because the samples were too fragile. The use of a low viscosity epoxy was needed to polish the surfaces, but the epoxy would fill the interparticle space and hide the binder bridges.

ImageJ is an image processing open-source software. It was used to measure the length of the interparticle bridges on SEM BSE images. Six bridges were measured, and every bridge was measured 6 times. Figure 3.4 shows an example of the measurement. It is to be noted that the transition from places where the binder is present to spaces where there is no binder are difficult to find. However, there are spaces where one can be certain of the presence of binder. In Figure 3.4, the yellow arrows point at regions with clear presence of polymer while the white arrows point at regions where the presence of polymer is not evident.

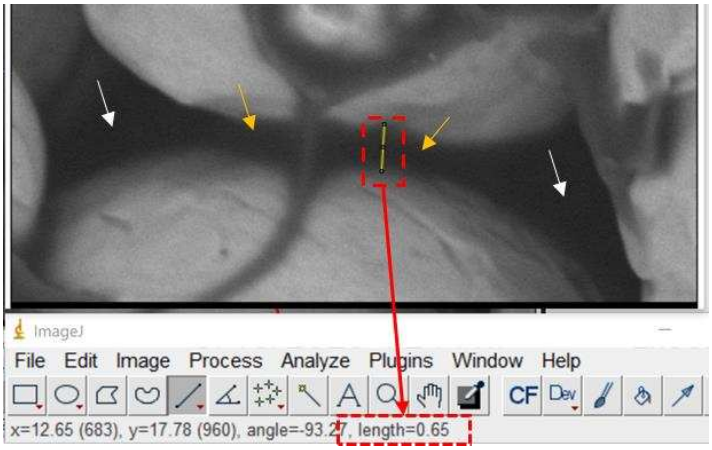

Figure 3.4 Bond length measurement with ImageJ. The white arrows point at spaces that are probably . The yellow arrow point at the limits of the binder bridge distinguishable with the eye.

3.2.7 Binder distribution

The binder saturation of the hand-made green bodies was slightly higher than 100 %. In fact, the samples presented a sedimentation effect: the volume of binder exceeded that of the space between the powder particles. Therefore, the particles to sank and the excess liquid accumulated at the top of the piece. The effect was only apparent under a microscope. Figure 3.5 illustrates this effect. It presents SEM images of different parts of the same sample. One can see that the bottom and middle have similar binder distribution (seen as dark areas, see also appendix B) whereas the

top part is filled by polymer. This means that there is an accumulation of binder on the top of the sample. However, compared to the height of the pieces (10 cm), this occurs in a very thin layer (~50 μm). Thus, the effect of this binder accumulation is considered negligible and is assumed not to have a significant impact on the results.

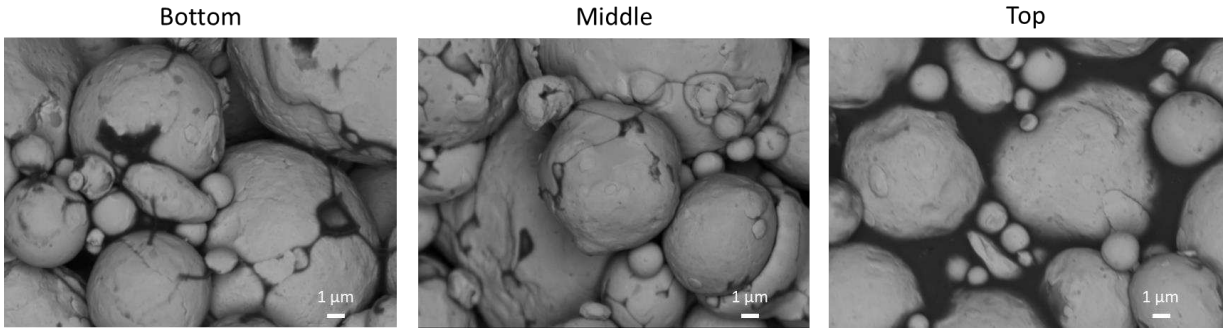

Figure 3.5 Binder distribution on a green body with respect to the height of the piece ($C_g = 0.69$ wt. %). The three images come from different broken parts of the same sample.

CHAPTER 4 KEY RESULTS AND DISCUSSION

4.1 Binder concentration and mechanical properties

4.1.1 PVA

The strength of the green bodies increases with the binder's concentration in the piece (C_g). The trend in Figure 4.1 shows that this increase resembles a quasi-sigmoidal curve. Thus, it can be divided in two main regions: an exponential-like increase of strength from 0.2 to 1.92 wt. % and a tail, a long reach of the maximum strength from 1.92 to 100 wt. %. Even though the strength increase is slower after the inflexion point at 1.92 wt. %, it continues rising significantly up to around 10 wt. %. Then it seems to reach a plateau at relatively low concentrations (~20 wt. %). At 50 wt. % it is evident that the curve has reached a plateau. The maximum strength (60 ± 10 MPa) is that of pure polymer samples, samples containing no metal particles.

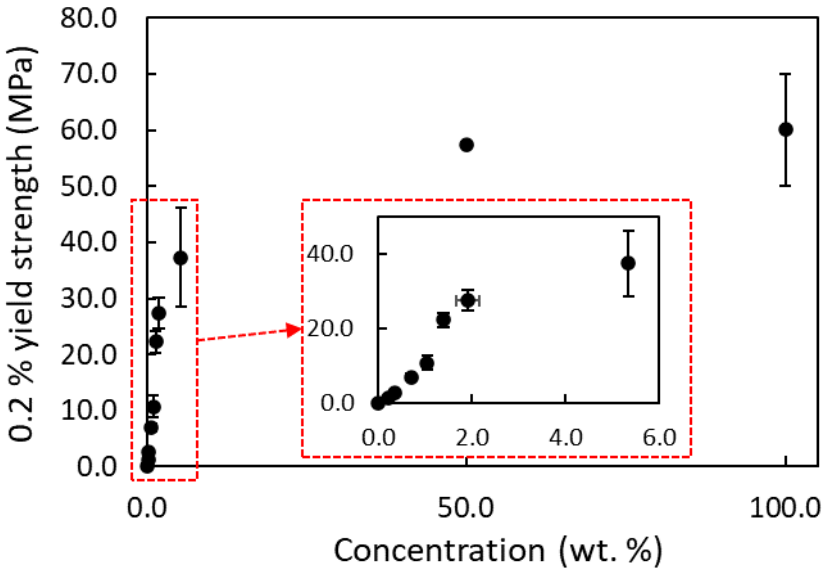

Figure 4.1 0.2 % yield strength of PVA green bodies as a function of C_g. Errors are 95% C. I.

Onoda's theoretical model of green strength predicts a fast increase at the beginning of the strength-concentration curve followed by a plateau [88]. However, it does not account for the exponential shape of the curve. That exponential trend at low binder concentrations has been observed experimentally before [40]. However, due to the limitations of the printhead in BJ, only small variations of concentration are possible. For this reason, the trends seem linear in some

studies [29, 44]. In fact, the strength of a single particle-particle bridge can be modelled as the strength of a hollowed cylindrical beam:

$$\sigma_{cylinder} = \frac{My}{I} = \frac{Fhr}{\frac{\pi}{4}(r^4 - r_0^4)} \tag{4.1}$$

where M is the torque applied to the beam, I, the moment of inertia of an annular surface and y, the point with the higher accumulation of stress, which is the outer radius of the bond r in this case. r_0 is the inner radius and h, the length of the bond (Figure 4.2).

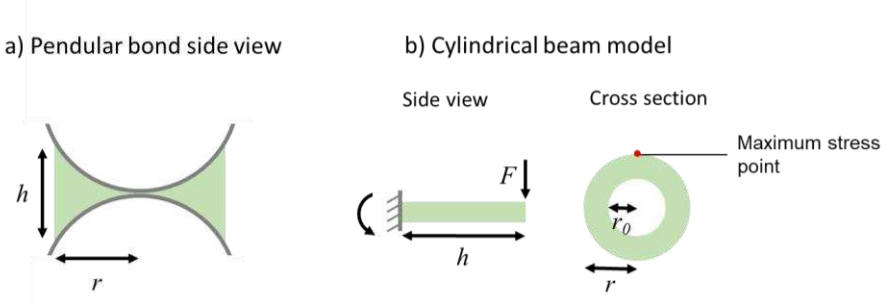

Figure 4.2 Schematic of the cylindrical beam model.

Therefore, the maximum load that a bridge can hold is:

$$F_{bond} = \frac{\sigma_{binder}\pi(r^4 - r_0^4)}{4hr} \tag{4.2}$$

Since the strength of the bond is determined by the strength of the pure binder [36, 88], σ_{binder} replaces $\sigma_{cylinder}$. Figure 4.3 shows the trend of equation (4.2. It clearly reveals the exponential-like increase of the strength of a single bond as its radius increases. Since the strength of a green body is the sum of the contributions of every interparticle bridge (eq. 4.3), it is reasonable to obtain an exponential-like increase for the green strength too.

$$\sigma_{green} = \frac{1}{A_{green}} \sum_i F_{bond,i} n_i \tag{4.3}$$

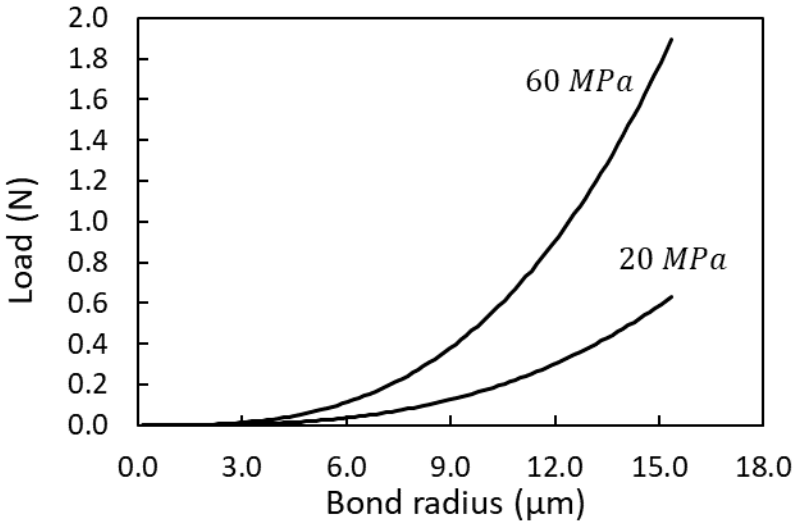

Figure 4.3 Model curve of the maximum bond strength as a function of bond radius for a single bond according to equation 4.2 for two different binder strengths.

This said, equation (4.3 overestimates the real green strength because it does not consider the effect of stress inhomogeneities and crack nucleation and propagation mechanics. Additionally, it does not consider the impact of the binder location in the piece.

Figure 4.4 presents SEM micrographs of green bodies after compression tests at three different PVA C_g values. As concentration increases, the polymer is more and more visible (seen in these micrographs as dark areas, especially at particle contact points, see also appendix B). Interestingly, the polymer is almost invisible in the lower concentration sample (Figure 4.4 a) However, its 0.2 % yield strength is 2.6 MPa. This implies that the polymer is mostly located between the particles. As concentration increases, the shape of the binder bridges becomes more apparent. In the middle image, the circular and semi-circular binder marks are places where particles were bonded. Additionally, in the same image, we can observe that the binder tends to form an interconnected network. Slim binder lines (yellow arrows) are connected to the annular marks, which indicates that there is a certain amount of binder that is not useful, as it does not participate in the interparticle bonding (see also appendix C).

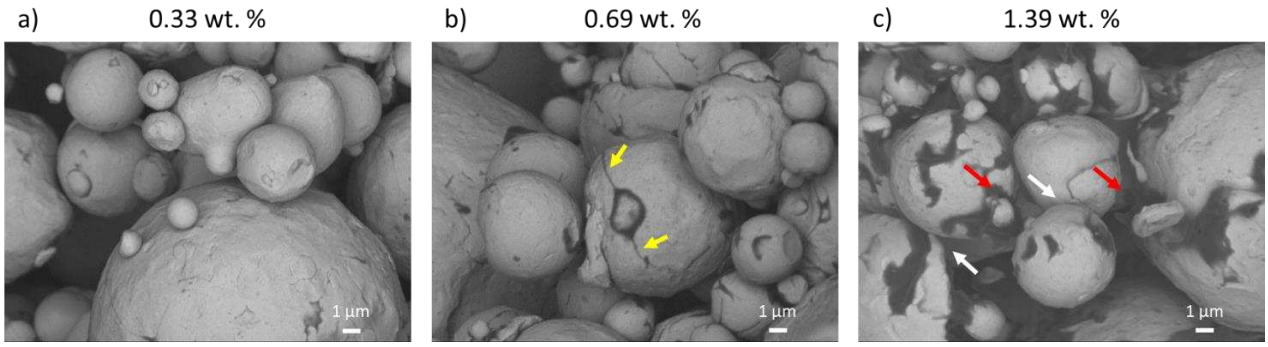

Figure 4.4: BSE SEM images of fractured PVA green bodies with different C_g values: a) 0.33 wt. %, b) 0.69 wt. % and c) 1.39 wt. % . Yellow arrows point at the slim binder lines coming out of the annular mark. Red arrows point at places where the polymer failed cohesively. White arrows point at interparticle necking regions.

Normally, the binder is interconnected when it is liquid (Figure 4.5 a) and as it dries, it is pulled towards the necking regions under the effect of capillary pressures (Figure 4.5 b and c) and results in individual interparticle bridges (Figure 4.5 d). In this case, as the binder dries, it turns into a gel because the polymer concentration increases [158]. Through hydrogen bonding, PVA chains form a physically crosslinked network: the hydroxyl groups of one chain can react with the hydroxyl groups of other chains [132, 159]. For this reason, as the liquid dries, the cohesive energy is sufficiently high to maintain the binder interconnected. Finally, when the binder is almost dry, the concentration of PVA reaches saturation, which makes it deposits even if it is not located at the necking regions [31] (Figure 4.5 f). This said, these interconnections are not maintained through all the piece and they become thicker in samples with higher binder concentration. At low concentrations they are not apparent.

In Figure 4.4, the higher concentration sample shows signs of polymer decohesion. Between the particles, the polymer seems to be torn (red arrows). It leaves two polymer sides with uneven, rough shapes. This implies effectively, that the PVA-SS316L samples fail in the polymer phase, and not at the polymer-metal interface. Therefore, the interactions between the binder and the metal are stronger than those between the polymer chains. In other words, the strength of the green bodies is governed by the binder phase strength.

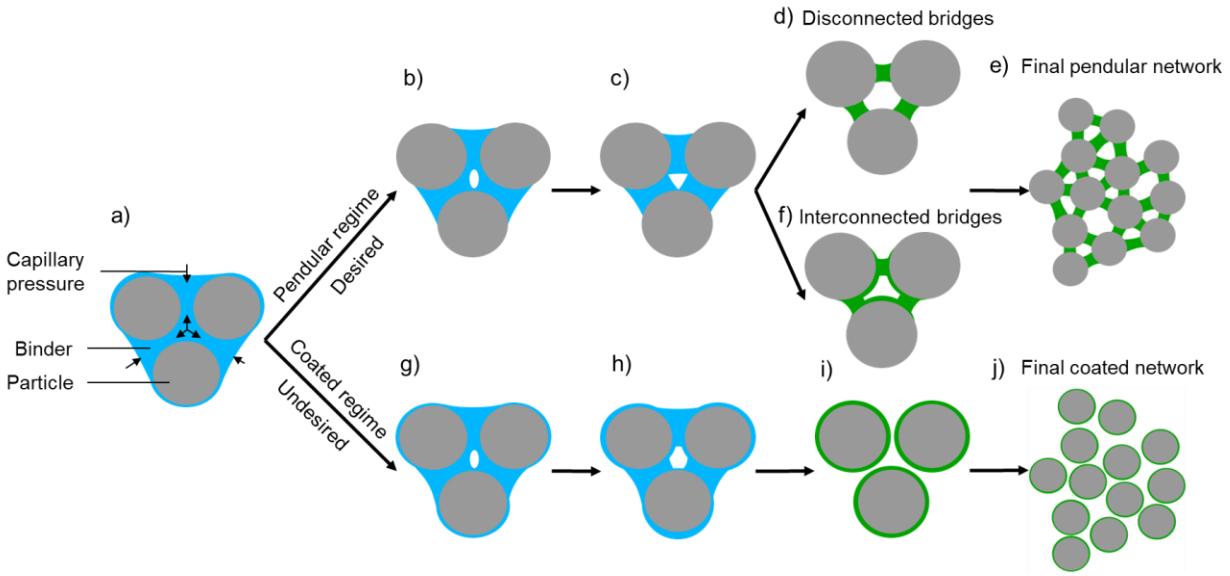

Figure 4.5 Binder drying mechanisms and final bridges. The blue binder is liquid, and the green binder is solid after evaporation. a) Initial state (100 % SR). b-c-g-h) Binder drying, reduction of the SR. d-f-i) Types of interparticle bridges. e) Strong interparticle network (preferred). j) Weak interparticle network (not preferred): due to the binder distribution, more binder is needed to form interparticle bridges.

The micrographs of Figure 4.4 also show that the inter-particle volume is replaced by the binder as its concentration rises. Thus, the fill factor, Φ, defined as the ratio between the volume of dried binder, V_{binder}, and the volume of the piece that is not occupied by the metal powder, V', can be used to better visualize the distribution of binder in the system. The fill factor is defined as follows:

$$\Phi = \frac{V_{binder}}{V_{piece} - V_{metal}} = \frac{V_{binder}}{V_{air} + V_{binder}} = \frac{V_{binder}}{V'} \tag{4.4}$$

where V_{piece} is the volume of the green body (metal + binder + air), V_{metal}, the volume of metal as if the powder was one full metallic piece and V_{air}, the volume of air.

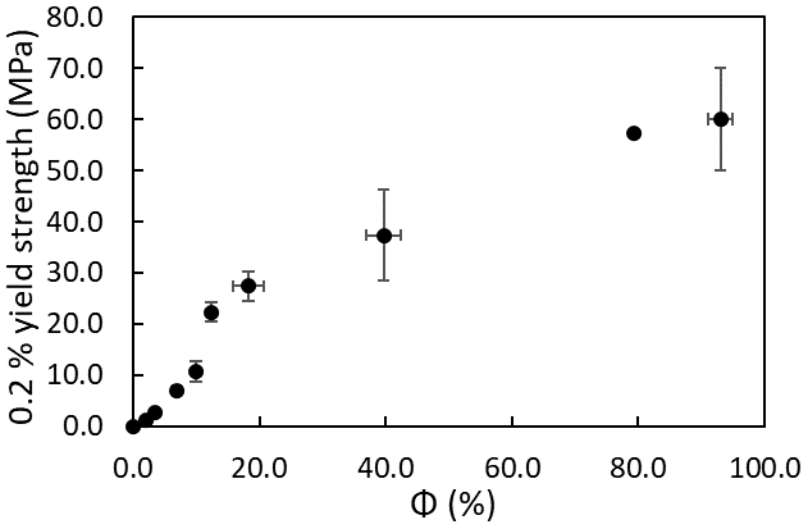

Figure 4.6 0.2 % yield strength of PVA green bodies as a function of the fill factor. Errors are 95% C. I.

The 0.2 % yield strength of the PVA green bodies is plotted against the fill factor in Figure 4.6. Compared to concentration (Figure 4.1), the fill factor results in a more evenly distributed curve. The graphic maintains the quasi-sigmoidal shape, but the regimes become more distinguishable. The exponential-like regime goes from 2.1 to 18.3 % (0.20 - 1.92 wt. %) and the tail, from 18.3 to 93 % (1.92 - 100 wt. %). Directly, one can conclude that the reason why the plateau of strength is reached at low binder concentrations is because the fill factor is already close to 100 %. For instance, the 40 % Φ value corresponds to the 5.35 wt. % concentration and the 80 % Φ, to the 50 wt. %. In other words, the strength increases until the point where the binder replaces a significant fraction of the air volume in the piece and that happens well below 100 wt. % (~20 wt. %).

The green strength increases in an exponential-like manner due to interparticle bond coarsening. This happens up to 18.3 % Φ (1.92 wt. %) where the bonds start touching each other. By dividing the binder volume of the piece by the number of bridges (eq. (2.10)), one can obtain the volume of binder between particles, assuming that all the binder is located at the necking region. With that information for the samples at 1.92 wt. %, the inflexion point, equation (2.9 tells us that the interparticle bridges' length is approximately 1.10 μm. The real length of the bonds, measured with the help of SEM images for 0.69 wt. % samples, is 0.62 ± 0.05 μm (error is a 95 % C. I.). The bridge size measurements were done on 0.69 wt. % samples since the interparticle bonds at that

concentration are more defined. A bridge length of 0.62 μm is reasonably close to 1.10 μm considering that all the binder is located in the interparticle regions only in ideal cases. In reality, there is always binder deposition in non-optimal locations. In fact, in Figure 4.4, one can see that the 1.39 wt. % sample has already a significant amount of binder outside the necking regions even though, the interparticle zones are not saturated (white arrows). This is normal, as that sample is close to the inflexion point concentration.

Before the inflexion point, the relative density of the green bodies stays constant since the volume and mass of the polymer are negligible with respect to the volume of metal (Figure 4.7). After that point, the density of the bodies starts increasing, which also indicates that the necking regions are saturated and the pores between particles are being filled by the binder.

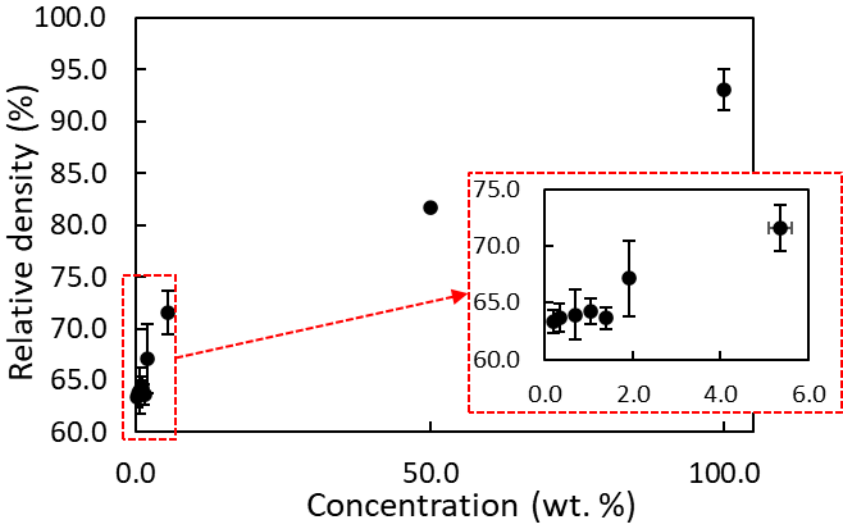

Figure 4.7 Relative density of PVA green bodies as a function of C_g. Errors are 95% C. I.

Comparing Figure 4.1 and Figure 4.7, one can see that for low concentrations (0 to 1.92 wt. %), the relative density stays constant even though the concentration and the strength increase. This is rarely seen in BJ, as changes in concentration are often achieved by changing the binder volume through the printing parameters. In other words, to change the final binder concentration of a piece, normally, the printing parameters such as saturation ratio or droplet volume are adjusted. This results in an increase of binder concentration in the final piece, but also in an increase of liquid binder volume. This increase of liquid in the green body results in a densification of the powder bed because of the action of capillary forces that pull the particles together [55, 84]. As a result of the powder densification, the green strength increases [29, 40, 83]. This is not the case in our

method, as the different samples up to $C_g = 2$ wt. % were prepared using the same liquid volume (0.33 ml), but different C_b values. Therefore, with our technique, the final dried binder content increased, but the liquid volume used to prepare the samples was constant. As a result, the powder packing density did not change. Hence, this method results in an increase of C_g without having a significant impact on the relative density. Thus, this data shows that even if higher densities result in higher green strengths, the impact of binder concentration is much more important in BJ.

The relative density of the low C_g bodies varies between 63 and 65 %, which is comparable to what can be obtained for SS 316L [40] and other types of SS [42] in the printing process, generally close to 60 %. It is important to notice that the density of the pure PVA samples was of 93 %, which indicates that these samples had a porosity of 7 %.

The general shape or the strength as a function of Φ is presented in Figure 4.8. The behavior of the green body as a function of binder content is divided into three regions, limited by the red points and dashed lines. Region A corresponds to the range of concentrations where binder starts accumulating in the interparticle regions without forming interparticle bridges. The transition to B occurs when the first binder bridges are formed. At that point the strength starts rising in an exponential-like manner.

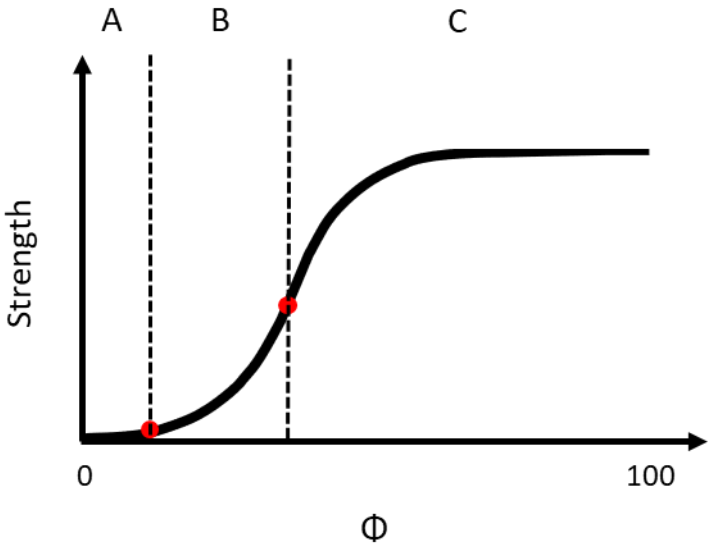

Figure 4.8 Strength as a function of the fill factor model curve. Region A: induction period where no interparticle bridges have formed; Region B: interparticle bridge network formation and bond coarsening; Region C: tail off to pure polymer properties

The exponential-like increase takes place due to the increasing number of interparticle bonds that are being formed. Additionally, in this region the coarsening of the interparticle bridges takes place (Figure 4.3) and the formation of an interparticle solid network is completed (Figure 4.5 e). Binder jetted samples fall in this region, as a good binder results in the formation of an interparticle network held together by pendular bridges.

Finally, the transition from region B to C takes place when the binder's fill factor in the metal powder bed is high enough to saturate the interparticle region. At that point, interparticle bridges touch each other and the binder starts filling the remaining pores as the concentration increases. This region is a long tail off. The strength increases until it reaches the pure polymer strength.

4.1.2 PAA and PVP

In Figure 4.9, the 0.2 % yield strengths of PVP and PAA green bodies are compared to those of PVA samples for various fill factors. Interestingly, PVP and PAA also show an exponential-like increase. However, the strength increase is slower for PVP and even slower for PAA. This could be caused by the mechanical properties of the polymers. As displayed in Figure 4.3, the mechanical strength of the binder has a direct impact on the shape of the exponential strength increase. Tensile tests of pure PVA, PAA and PVP films indicate that the strengths of those polymers are 44 MPa (M_w = 26 kg/mol) [160], 27 MPa (M_w = 90 kg/mol) [161] and 16 MPa (M_w = 75 kg/mol) [162], respectively. As PAA and PVP have lower mechanical properties than PVA, it is normal that their strength increase is also lower.

The SEM images in Figure 4.10 show how these three binders behave and form the inter-particle bridges in the green bodies. On one hand, PVP's behavior is similar to that of PVA. They both form pendular bridges and have annular marks where the particles were bonded. However, PVP does not tend to have interconnected bridges. It forms regular pendular bonds such as those depicted in Figure 4.5 d. In fact, PVP has a lower CED than PVA (305 J/cm^3 and 519 J/cm^3, respectively [65] and 529 J/cm^3 for PAA [163]) Therefore, as the PVP binder dries, it is unable to resist the capillary pressures that pull the binder to the necking regions. On the other hand, the PVA binder forms interconnected pendular bridges (Figure 4.5 f and yellow arrows in Figure 4.4), as it can resist the capillary forces because it forms a crosslinked hydrogel [159].

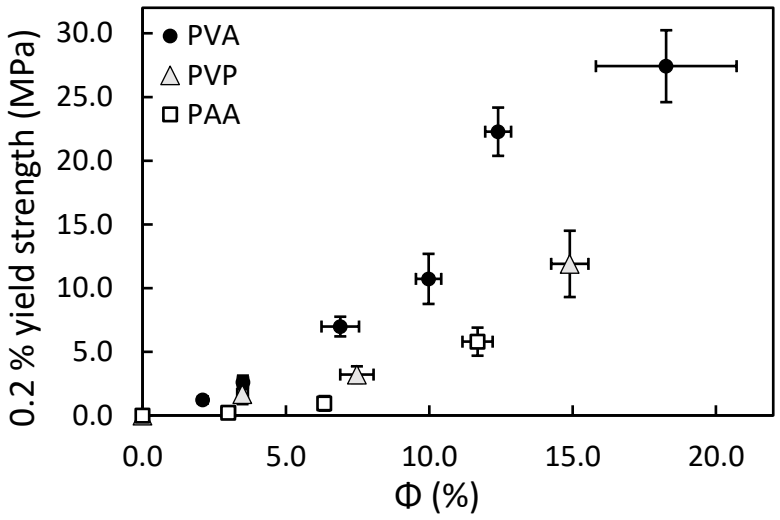

Figure 4.9 0.2 % yield strength of green bodies made with PVA, PVP and PAA binders with respect to the fill factor. Errors are 95% C. I.

On the other hand, PAA tends to preferentially coat the metallic particles (Figure 4.5 i). At small concentrations (top images in Figure 4.10), the PAA sample contains annular marks where particles were bonded, but it also contains several non-annular marks all over the metallic surface. This means that a significant amount of binder is not participating in the inter-particle bridging, which reduces significantly the mechanical properties of the sample [88]. This behavior is therefore undesired. It explains why PVP gives more strength than PAA even if it has lower mechanical properties. The coating behavior of PAA is more apparent in the bottom images. One can clearly see that the particles in the PAA sample are completely coated by the binder. Interestingly, there is only a 2.4 % difference between the CED of PVA and PAA (i.e. 519 J/cm^3 and 529 J/cm^3, respectively)

Whether the binder coats the particles or forms pendular bridges depends on the relation between metal-polymer affinity (binding energy) and polymer-solvent affinity. In fact,. PAA forms covalent bonds with the iron oxide present in the stainless steel surface [117, 155] while PVA and PVP form hydrogen bonds with the hydroxylated oxide surface of the metal [135, 144]. Contrary to PVA and PVP, PAA samples could resist being immersed in water, which confirms that the interactions of PAA with the metal are much stronger. In the case of PVA and PVP, at low polymer concentrations the -OH groups on the metal surface adsorb the solvent molecules (water, in this

case) which form hydrogen bonds with the polymers [164]. As the water dries these bonds break and the polymers return to the solution. This is not the case with PAA, as the covalent bonds cannot be easily broken.

Evidently, if the binder is too viscous and has a low surface tension, capillary forces cannot transport the binder to the necking regions as it dries, which causes the binder to deposit over all the metallic surface (coated regime, Figure 4.5 i) [88]. However, this is not the case in our study, as can be seen in Table 4.1, where the physicochemical properties of the binders used to prepare the top samples on Figure 4.10 are presented. In fact, the PVP forms pendular bridges even though it has similar properties to PAA. Also, PVA has the higher capillary number, which indicates that it is the worse binder to form pendular bridges. This clearly indicates that a binder can be in the coating regime even if it has a low surface tension and a high viscosity. These results also suggest that the coating behavior of PAA is not related to its physicochemical properties.

Table 4.1 Physicochemical properties of the 3 binders used to prepare 0.69 wt. % (C_g) samples.

Sample	**Surface tension (mN/m)**	**Viscosity[*] (cP)**	$\boldsymbol{Ca}^{**}$ **(2.7)**
PVP	67.7 ± 0.1	8.3 ± 0.1	0.12
PVA	43.0 ± 0.1	16.1 ± 0.1	0.37
PAA	65.0 ± 0.1	10.7 ± 0.1	0.16

[*] Ambient temperature.

[**] Assuming the same velocity of 1 m/s to simplify the units.

Additionally, these SEM images show that the three binders fail by polymer decohesion. Particularly in the bottom images, one can see signs of ductile-brittle failure in the polymer phase for every binder (red arrows). As a result, the strength of the PVP and PAA samples is also dictated by the binder phase strength, as was shown for PVA previously. In the case of PAA, the samples do not reach their maximum possible strength (i.e. pure polymer strength) because of poor binder distribution (coated regime).

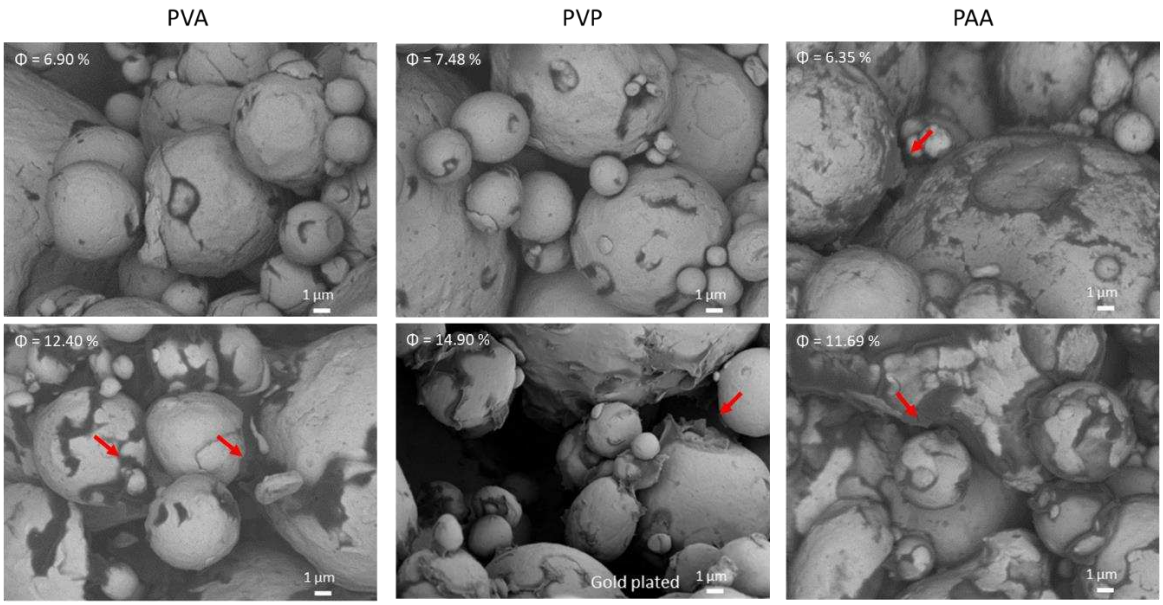

Figure 4.10 BSE SEM images of PVA, PVP and PAA green bodies with two different C_g values: 0.69 wt. % in the top and 1.39 wt. % in the bottom. Red arrows point at places where the polymer failed cohesively.

It has been shown that as C_b rises, the adsorption of the polymer onto the metallic oxide surface increases [36, 119]. The adsorption is negligible before a certain C_b value and after a higher concentration, the number of molecules bonded to the surface reaches saturation. The adsorption process forms the first monolayer of polymer from which the bridges will initiate. It explains why PAA does not form a homogeneous coating at low C_b values (Figure 4.10). Initially, the concentration of PAA is too low to form this first monolayer, but as binder dries, the concentration increases, and a more significant adsorption takes place. Therefore, when the PAA concentration is sufficiently high to adsorb significantly into the surface, the liquid is no longer coating the entire particle. As a result, the polymer is not deposited evenly on all the metallic surface. It only forms homogenous coatings when the initial binder concentration is sufficiently high to start adsorbing onto the metal surface while the liquid is still coating the particles.

In addition, the formation of that first polymer monolayer is another factor explaining why the exponential-like increase in the strength vs C_g curve is steeper for some binders. They reach adsoption saturation at different C_b values, as have ben seen in other binder - powder systems [119].

Comparing the model curve of Figure 4.8 to the experimental values in Figure 4.9, one can observe that PAA presents the longest induction period, followed by PVP and then, by PVA. This is expected, as PAA tends to deposit over the entire particle surface. Therefore, it takes higher PAA concentrations to form the first interparticle bridges. In the case of PVP, it readily forms pendular bridges, which means that it has a short induction period. However, PVP is significantly weaker than the other polymers. Thus, the exponential-like increase as a function of fill factor of this binder takes place at a lower rate, as weaker polymers form weaker interparticle bridges. In other words, PVP needs the accumulation of higher binder quantities than the other polymers to attain the same strength.

These results give us new insights into the characteristics of a good binder. First, it would have a narrow induction period (region A). This means that it would form the first interparticle bridges at the lowest possible fill factor and it would then transit to region B, as region B is the region of interest for BJ. Additionally, it would also have a steeper rise in properties as a function of the fill factor in region B. In other words, it would have high pure polymer properties and would readily form a network of pendular bridges. Among the studied polymers, PVA is the one that better meets these performance criteria. Under these considerations, it is the best binder over PAA and PVP.

4.2 Effect of molecular weight

The impact of the molecular weight was studied with 5 wt. % (C_b) binders of PVP since PVP was commercially available in different molecular weights without changing other polymer parameters. In the case of PVA, it was available with different molar masses, but the hydrolysis percentages or the molecular weight distribution varied.

The mechanical properties of the green bodies increase with increasing molecular weight (see also Appendix D). Figure 4.11 shows a logarithmic trend which corresponds to the normal behavior of the mechanical properties of a polymer when the molecular weight increases [76, 165-167] (Figure 2.17). Previously, the degree of polymerisation of PVP was found to increase the strength of granules, as higher M_w results in higher polymer cohesion [90]. However, the strength reaches a plateau at relatively low molecular weights. In fact, the strength gain between 40 kg/mol and 360 kg/mol is less significant compared to the gain between 10 kg/mol and 40 kg/mol even

though the variation of M_w is much higher. This means that there is a threshold M_w when the size of the polymer chains stops having an impact on the green strength. Compared to the effect of ϕ, the strength variation with respect to M_w is less pronounced. However, the M_w helps to tune the printability of the binders through their viscosity since higher M_w results in higher binder viscosities [27]. On the other hand, high M_w polymers become more difficult to burn off during debinding [38].

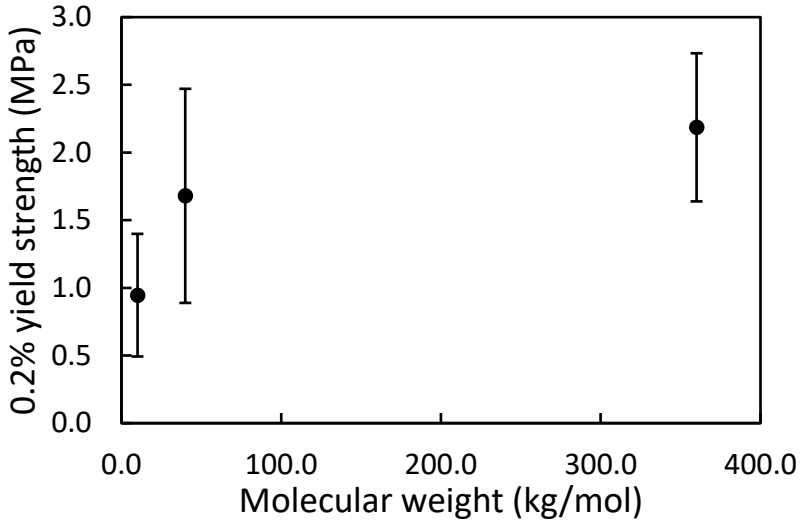

Figure 4.11 0.2 % yield strength of PVP green bodies as a function of the molecular weight. Errors are 95 % C. I.

4.3 Effect of pH

Figure 4.12 presents the strength of the PAA green bodies with respect to the pH of the binder solution. One can see that the strength of the PAA samples is very low at low pHs and it is much higher at high pHs ($C_b = 5$ wt. %). It increases significantly between pH=3 and 6. However, it stays constant up to pH $\approx$ 10. This sudden change of properties between pH = 3 - 6 might be a consequence of the "on-off" behavior of this polyelectrolyte [96, 154]. At pH = 5 the carboxylic groups become predominantly negatively charged ($RCOO^-$), according to equation (2.22). The properties of the metal being dominated by the presence of Fe_2O_3 [109, 113], the metallic surface is principally covered by OH_2^+ groups [102, 117]. This means that the interactions between the

polymer and the metal become stronger, as PAA is known to react with positively charged surfaces [36].

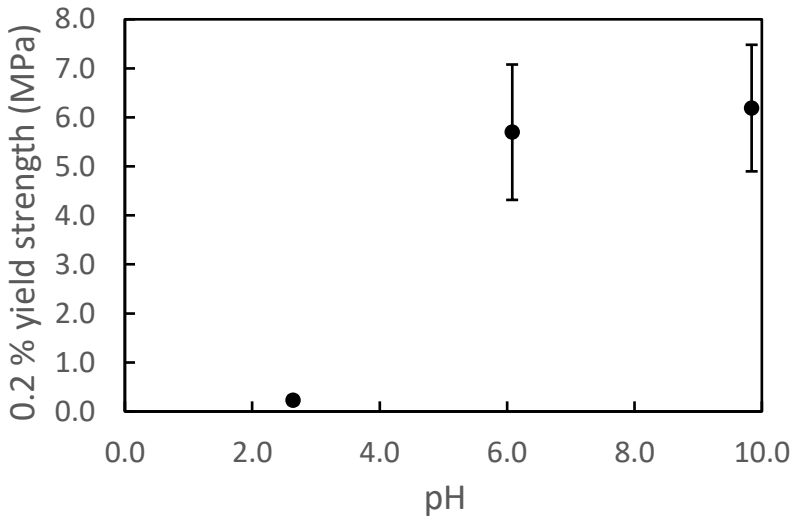

Figure 4.12 0.2 % yield strength of PAA green bodies as a function of the binder's pH ($C_b = 5$ wt. %). Errors are 95 % C. I.

4.4 Effect of ink

The results presented previously are obtained with binders made only of polymer dissolved in the dispersing medium (water). However, most of the time the printability of these simple formulations is not optimized for binder jetting printheads. Different additives must be added to the formula to obtain the desired liquid properties. This section is merely an example of what could happen to the properties of the green bodies if an ingredient is added to an existing formula. The impact of a water-based ink was selected, as it is common use in BJ to add an ink to facilitate the observation of the binder with the naked eye [32, 41, 70]. The results highlight the importance of assessing the impact of every new ingredient on the properties of the green bodies.

Table 4.2 contains the values of the dimensionless numbers of the 1-15 wt. % wt. % (C_b) PVA binders, with and without 1-15 wt. % of ink (composition is a trade secret). These binders resulted in green bodies with fill factors of 3.5 % (without ink) and 3.55 % (with ink). One can conclude that the physicochemical properties of the binder and the fill factor values are not significantly affected by the ink. In both cases, binders are in the printability region defined by the

Reynolds number - Weber number plane. The same amount of ink was added to the PVP and PAA binders for comparison purposes.

Table 4.2 Physical properties of the PVA binder solution with and without ink (1-15 wt. % addition).

Sample	$\boldsymbol{Re}$ **(eq. (2.1))**	$\boldsymbol{We}$ **(eq. (2.2))**	$\boldsymbol{Z}$ **(eq. (2.4))**	$\boldsymbol{Re^{\frac{1}{4}}We^{\frac{1}{2}}}$
PVA 1-15 wt. % wt. % (C_b) with ink	5.8	6.4	14.7	5.0
PVA 1-15 wt. % wt. % (C_b) without ink	4.7	6.9	12.4	4.9

Even though the PVA binder with ink maintains the same physicochemical properties, the strength of the green bodies varies significantly. Figure 4.13 a displays the values of the strength of the green bodies made with the modified binders (see also appendix E). Interestingly, the three curves maintain the exponential-like regime. However, the strength increase is very slow for PVA and PVP, compared to the no-ink binders (Figure 4.13 b). This effect is especially apparent in the PVP values. With ink, PVP gives almost no strength to the bodies and PVA's strength is significantly reduced. In contrast, PAA maintains similar properties as a function of fill factor. It is interesting to note that, earlier in this chapter, PAA without ink was shown to have the weakest tendency to form interparticle bridges as compared to PVA and PVP. This may explain why its properties were the least diminished with added ink among the three binder types.

One can compare the behavior of the three binders with and without ink thanks to the images in Figure 4.14. It is not possible to differentiate between the ink and the polymer. One can only see the binder as a whole: polymer plus additives. This is probably due to the small amount of solid ink in the dry binder (~ 5- 10 wt. %). Another explanation is that they form a homogeneous phase. In the case of PVA, the binder distribution is very similar. The binder is mostly located between the particles and is almost not present out of those regions. For PVP, the ink sample has more binder outside of the necking region. Around the particles, one can see a bigger polymer stain than in the case without ink. This is one of the factors explaining why the strength of the PVP green

bodies decreases so much. Not all the binder is contributing to the interparticle bridge. Finally, we can see that PAA behaves the same way with and without ink. The SEM images shows clear signs of polymer decohesion in both cases and an inefficient polymer distribution.

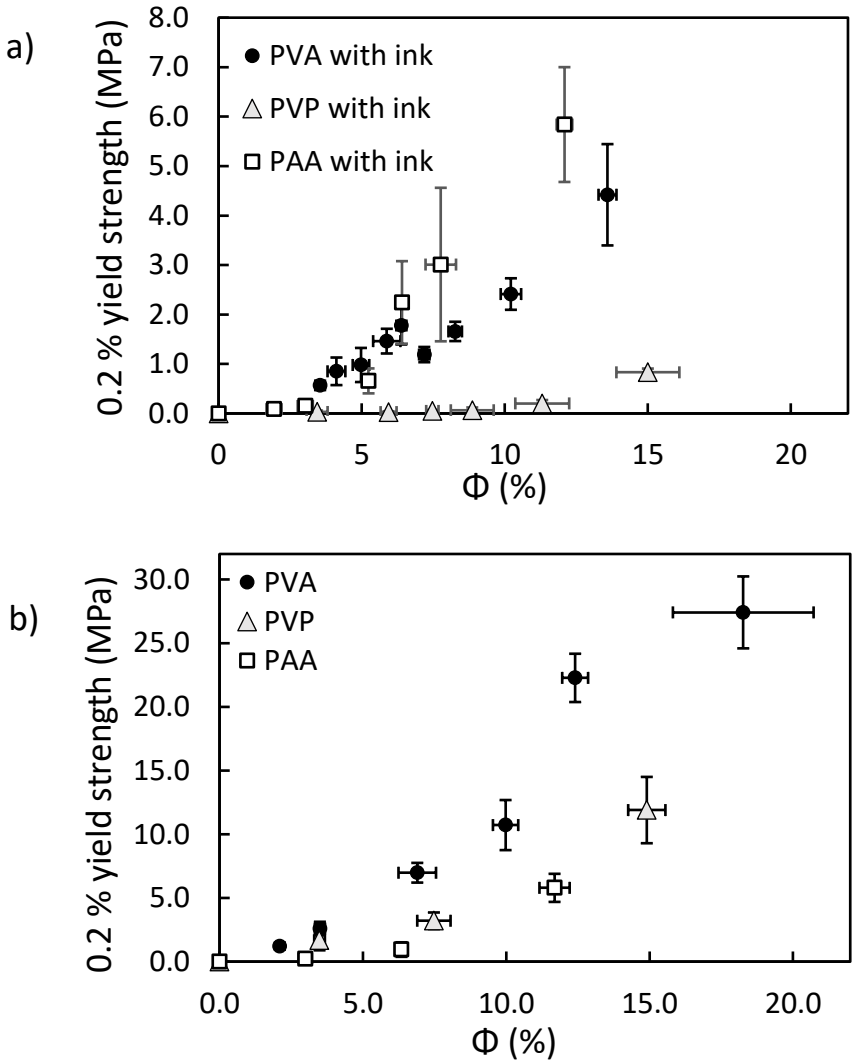

Figure 4.13 0.2 % yield strength of green bodies made with PVA, PVP and PAA binders as a function of the fill factor for samples a) with and b) without ink (1-15 wt. % of the binder solution). Errors are 95% C. I.

The strengths of 100 % PVA samples with and without ink are 38 ± 6 and 60 ± 10 MPa, respectively. The value of PVA with ink is significantly lower than that of the pure PVA samples. Therefore, the strength reduction of green bodies made with the binder containing ink is related to

a decrease of the strength of the polymer phase, on top of the surface spreading phenomena described. In fact, the ink might contain glycol esters since they are often used as humidifiers (Table 2.2) [39, 78]. However, they are also known for being common plasticizers [168]. Additionally, there might be adsorption competition between the different molecules in the ink and those in the binder. As a result, the metal - binder adhesion might be deteriorated. Probably, a combination of these phenomena is lowering the green bodies properties.

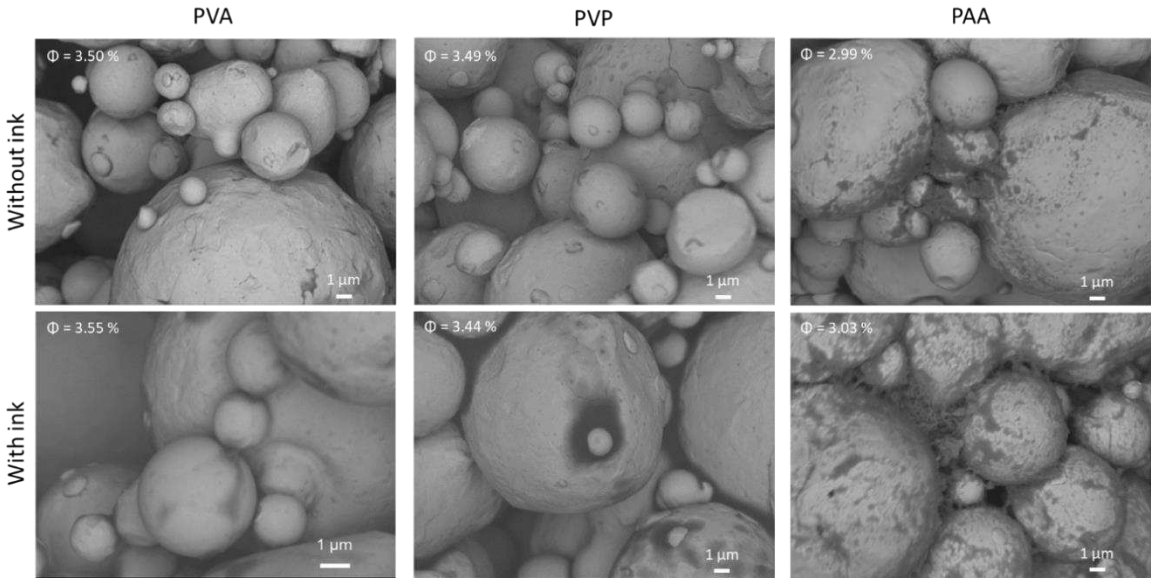

Figure 4.14 BSE SEM images of fractured PVA, PVP and PAA green bodies with a C_g value of 0.33 wt. % with and without ink.

In order to counter the effect of the ink, a crosslinker was added to the PAA+ ink binder. The effect of borax on the PVA + ink samples' strength is shown in Figure 4.15. The strength increases in an exponential-like manner up to ~ 0.2 wt. %. After that value, the strength starts decreasing. This can be explained by the different ionic interactions that vary depending on the concentration.

At low sodium tetraborate concentrations, the crosslink density increases, making stronger green bodies. Probably, at some concentration between 0.15 and 0.2 wt. %, the Na^+ concentration is sufficiently high to screen the repulsion between the negatively charged crosslinks. As a result, the complexation density could increase rapidly, drastically changing the strength of the pieces [139, 140]. After a threshold value, the strength of the green bodies starts decreasing. This is a behavior observed in other polymer crosslinker systems [169]. It can be explained by three

mechanisms. First, the binder network is charged as a whole, so it repels the surface to which it should adhere [140], which is not the case here, as borax confers a negative charge to the binder and the metallic surface is positively charged. Second, the mobility of the polymer chains needed to create the adhesive bonds is reduced by the crosslinks [170]. Finally, there is competitive adsorption between the borax molecules and the polymer [119]. Therefore, the decrease in strength in this system after 0.2 wt. % of borax is probably due to a combination of competitive adsorption and chain mobility reduction.

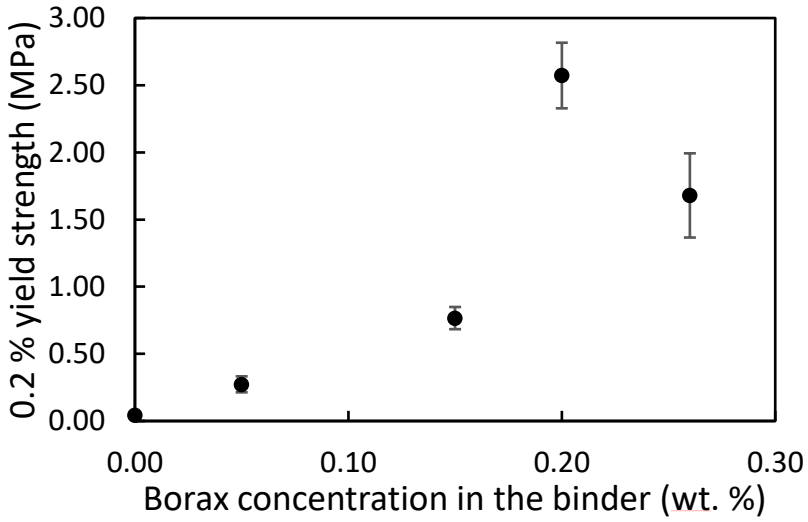

Figure 4.15 0.2 % yield strength of green bodies made with PVA + ink binder as a function of crosslinker concentration in the binder solution. Errors are 95 % C. I.

4.5 Proposed binder selection algorithm

Concerning the binder, the goal is to obtain the highest green strength while using a minimum amount of binder, having a high resolution, protecting the printhead and resulting in good final properties. Considering this and the findings discussed before. The following selection algorithm is proposed (Figure 4.16). It is a straightforward algorithm. However, the steps and considerations in colored circles are based on the findings of this work.

The algorithm is composed of 6 steps. It starts by selecting the solvent. It is accomplished by considering the wettability of the powder bed by the solvent thanks to contact angles reported in the literature. The solvent's contact angle on the metal must be lower than 90° (condition 1 a).

The toxicity of the solvent is also a selection criterion at this stage. The solvent must not be toxic or release toxic fumes in order to protect the environment and the worker's health (condition 1 b).

The second step consists in finding the adhesive agent of the binder by making a list of polymers that can be dissolved in the selected dispersing medium. The polymers are then screened in step three with the help of a screening table. The table must contain the following information about the polymers found in the literature: cost of the polymer per kilogram, degradability (residue percentage and degradation products), interactions of the polymer with the metal (physisorption vs chemisorption), interactions of the polymer in solution (CED), polymer strength and polymer density. Screening is done with a traffic light system: red = discarded, yellow = possible and green = good to move to next stage.

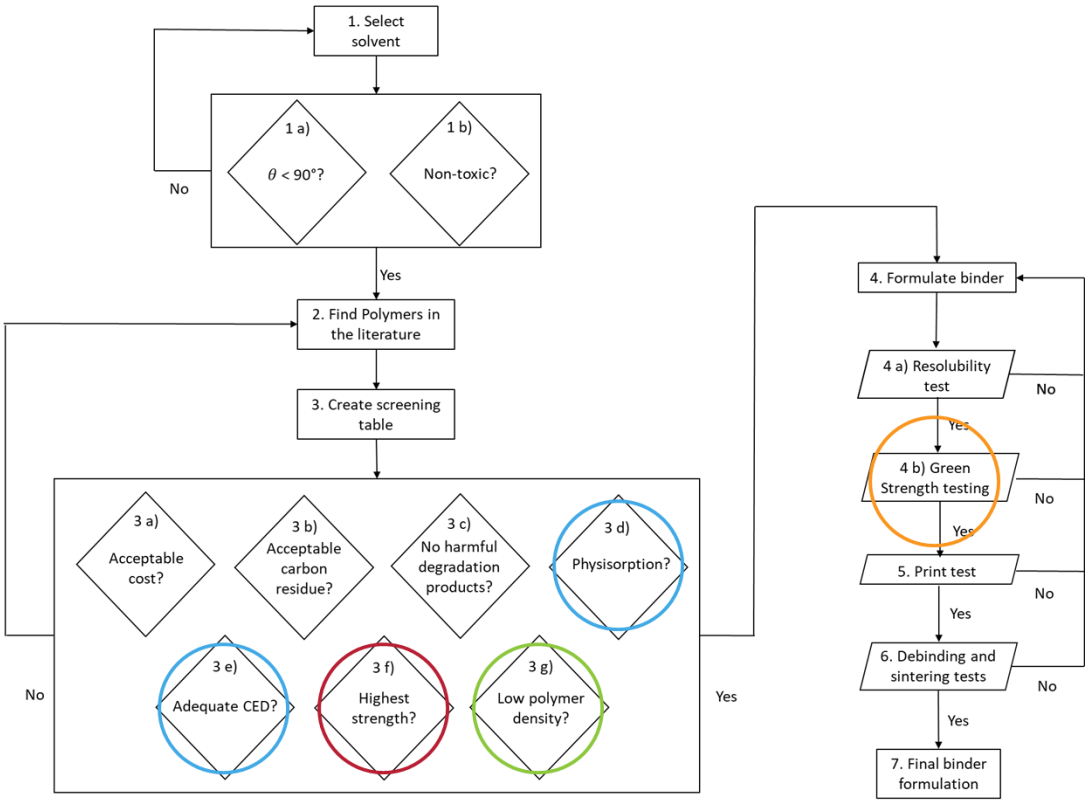

Figure 4.16 Binder selection algorithm. Squares represent process steps, diamonds, conditions, and parallelograms, testing operations. Diamonds inside one box need to be all respected. The circled steps are the ones proposed based on the findings of this work.

It is important to keep track of the polymer's cost to avoid spending time in an expensive material. Set a price limit and the polymers exceeding that limit do not pass (condition 3 a).

Concerning the degradation, the degradation products and residues are important parameters to know if a polymer is compatible with the final required metallurgical specifications and with the health and environmental constrains. In fact, any residue will be incorporated in the final piece, which might significantly change the metal composition. Therefore, a maximum residue amount must be selected as a function of the material standard composition intervals (condition 3 b). With respect to the degradation products, they are important to consider in order to avoid any health risk or environmental damage. Polymers with toxic degradation products such as CO, SO_2, HCl and nitrogen oxides [171] should not be considered (condition 3 c). Conditions 3 a and b can be respected based on literature data. Thermogravimetric experiments contain information on how much residue we can expect and the degradation temperature of our candidates. If the thermogravimetric experiments are coupled to Fourier transform infrared spectroscopy measurements, one can know also the degradation products.

With regards to the interactions of the polymer with the metal, one must consider that strong polymer metal interactions lead to a coating binder distribution regime, as observed with the PAA binder. Therefore, physisorption is preferred over chemisorption (condition 3 d). Additionally, the affinity of the polymer chains in solution with themselves must not be too high, else the binder might not migrate to the necking regions properly, as was the case of PVA. With information of the CED one can keep track of the polymer-polymer affinity in solution. According to the results on PVP and PVA's binder distribution, a CED between 305 J/cm^3 and 519 J/cm^3 is acceptable, although 519 J/cm^3 starts being too high (condition 3 e).

Polymer strength and density are the final aspects to take into account in step three. For the strength, data of tensile test of pure polymer films or other testing techniques are available on the literature. However, only data obtained with similar methods is comparable. One must choose the polymers with the highest strength as shown with the cylindrical beam model (condition 3 f). additionally, one must select the candidates with the lowest densities, as a low density promotes a steeper increase of the fill factor (condition 3 g).

Therefore, in step three, important polymer-metal and polymer-polymer interactions are considered. The blue circles in Figure 4.16 highlight parameters related to the binder distribution in the piece. The respect of these conditions leads to the formation of pendular bridges. On its side, the red circle accentuates the importance of pure polymer strength, which must be maximized for

a steep increase of green properties with respect to binder content. Finally the polymer density, circled in green, plays an important role on ϕ, as a polymer with a low density occupies more space in the interparticle regions.

The algorithm continues with step 4, which is the binder formulation. For this, the use of the algorithms of Utela et al. [32] and Tam et al. [27] is recommended. In this step the selection of additives and co-solvents is made. The screening table method can be used here too to select the other ingredients. Once the formulation obtained, crystallisation and resolubility (capacity to dissolve once it was dried) should be assessed because crystal formation as well as poor resolubility are nozzle clogging risks. In [32] a simple method to perform a resolubility test is proposed: let some binder dry in a watch glass and then rehydrate it by adding more binder. If the binder is not redissolved in seconds, it is not safe for the printhead. Same case if it forms solid particles after rehydration (test 4 a).

In step 4 b, one must prepare green bodies and test them in compression with the same or a similar technique that the one used in this project (out-of-printer approach). At this stage, the strength of green bodies made with two binders must be assessed: i) formulated binder and ii) polymer + solvent. If binder ii results in stronger bodies, the effect of every ingredient must be assessed separately. Solution ii is the baseline. Any ingredient that makes the strength go lower than that of solution ii, should be reformulated, if possible. Step 4 b is also important to explore the range of ϕ values that are in Region B, the exponential-like increase of the binder of interest.

The final two steps, steps 5 and 6, were not the focus of this project. Step 5 is a printing test and formulation modification stage. It is to be noted that the printing parameters should be optimized for every binder with the help of existing methods [23, 32], else a comparison between the binders reaching this stage is not possible. Finally, for step 6, debinding and sintering tests must be accomplished to verify the quality of the final piece.

4.6 General discussion

The project led to the development of an out-of-printer approach to prepare green bodies with a cylindrical shape of 1cm of height and 1cm of diameter. The preparation method can be further improved by analyzing the homogeneity of the binder powder mixture. In fact, the mixture was labelled as “good” when its consistency allowed hand manipulation. The only evidence of

binder homogeneous distribution comes from SEM images. Although the presence of binder in different parts of the same piece seemed similar in the micrographs, the images do not allow to conclude with a 100% certainty that the binder is homogeneously distributed. The hand mixing step could be replaced by a more specialized technique, but part of the relevance of this forming method is its simplicity. Another sign of adequate binder - powder mixing is the repeatability of the compression test and density data.

A second important aspect to analyze is the pressure applied to the paste while being molded and its impact on the green strength. As the paste is pushed by hand, there is no record of the pressure applied. It has been shown that pressure plays a major role in processes such as dry press forming. It would be worth assessing its impact on the hand-made samples. That said, the pressure applied by the hand (in the order of the kPa) is not as high as the one used in a dry press process (in the order of the MPa), which indicates that probably the pressure applied by hand is negligeable [172, 173].

Aiming to understand the different polymer-polymer and metal-polymer interactions giving strength to green bodies, the compressive properties of green bodies made with three different binders in various conditions was investigated. The results lead to the establishment of a new parameter to characterize the binder content in the pieces, ϕ. ϕ is an interesting parameter, as it contains information about the green concentration and the green density. ϕ is similar to the SR. However, it considers the solidified binder and not the liquid binder.

With the help of ϕ, a model curve was proposed (Figure 4.8). The curve considers important concepts such as the cylindrical beam model and the saturation of the interparticle necking regions. The curve contains three regimes of strength as a function of ϕ: an induction regime, an exponential-like regime and a tail-off. The conceptual understanding gained with the proposed model curve is very useful for concentration selection and binder ingredient selection. The curve allows the users to acknowledge the regime in which their application is situated and the impact that a given change of concentration might have on the green body's properties and on the debinding step. Therefore, the curve could serve as a guideline for binder concentration selection or modification. It also elucidated new binder selection criteria: a good binder passes to Regime B at low concentrations, it has a steep increase of strength and reaches Region C at low concentrations

also. That behavior can be obtained if the binder has a high pure binder strength and a low solid density.

While comparing, strength and binder distribution in the pieces made with PVA, PAA and PVP binders, it was shown that the binder distribution is related to the interactions of the polymer with the metal and the solvent. If the interactions with the metal are too strong the binder will tend to coat the particles. This conclusion was formulated based on SEM images, compression test data and literature values. However, it could benefit from a more detailed study on the bonds that form the three polymers with the metal surface. Fourier transform infrared spectroscopy or X-ray photoelectron spectroscopy measurements could help reinforce this conclusion.

It was additionally proposed that the CED played an important role in the binder's distribution in the piece. The polymers with the higher CED values did not form or only partially formed pendular networks. In fact, PVA (519 J/cm^3) formed a pendular network with interconnected bridges and PAA (529 J/cm^3) a coated network. On the other hand, PVP (305 J/cm^3) formed a regular pendular network. It is therefore probable that if the interactions between the polymer chains in solution are too strong, the binder will not form a pure pendular network. Therefore, the CED and type of adsorption (physical vs chemical) are two new important parameters that will help predict if a binder forms a pendular network in the piece or not.

Concerning the cylindrical beam model (Figure 4.3), the curve follows an exponential-like trend, which is in agreement with the experimental data. However, the model does not take into account the different shapes and directions of the pendular bonds. The bridges holding a green body while it is being tested in compression might withstand compressive, shearing and tension stresses. Therefore, the fact that this model agrees with the data tells us that it is the dominant mechanism at play, but most certainly it is not the only one. Thus, this model must be combined with other models such as the one developed by Onoda [88], the one developed by Kendall [87] or other classical mechanics models such as the thick cylinder model to gain a more comprehensive understanding of the failure of the green bodies. Also, other mechanical tests such as the bending test and the diametral compression test could be compared to these models and to the results obtained by regular compression test in order to obtain comparative and contrasting data.

It is to be noticed that the M_w of the three polymers is different, which makes the direct comparison between the binders apparently doubtful. However, it has been shown that the effect

of the molecular weight is less important than that of the fill factor (Figure 4.11). Additionally, M_w was never used to justify the properties of the green bodies. The binders were just seen as three materials with three different pure properties. Now, if one wants to take into account the M_w of the polymers, one needs to consider M_e, the glass transition temperature T_g and the crystallinity of the polymers.

The M_w of the three polymers is well above M_e, the minimum M_w a polymer needs to be able to give strength to a structure. The M_e of the three polymers is 5250 g/mol [174], 6900 g/mol [175] and 17000 g/mol [176] for PVA, PAA and PVP, respectively. Interestingly, the M_e of the polymers follows the same trend of the strength of the green bodies, but in the opposite direction. With respect to T_g, the values are 85 °C [130], 103 °C [177] and 410 °C [178] for PVA, PAA and PVP, respectively. The T_g values indicate that the polymers are all in the brittle regime when the green bodies are being tested in compression. However, PVA is a semi-crystalline polymer, while PVP and PAA are amorphous [130, 179, 180]. Therefore, PVA performs as a better binder because it has better mechanical properties even if its M_w is smaller.

Several conclusions and hypothesis in this work are based on SEM images of the different green bodies tested in compression. It is worth noting that the images are subject to interpretation and errors, as they are two-dimensional images of three-dimensional structures. Therefore, some of the features observed in the images might not be real. An example of this is the distinction between regions with binder and empty spaces (Figure 3.4). It is possible that some binder has been taken for empty space. Therefore, it would be pertinent to analyse the fractured green body surfaces with other methods to confirm the conclusions exposed. For example, if the green bodies surfaces were polished, the 3D on 2D images problem would be removed. However, the choice of the epoxy resin for the polishing process is very important, as it fills the interparticle spaces and might hide the binder. Thus, the epoxy must give a different signal than the binder so they can be both identified in the SEM or with another technique such as the atomic force microscope. Another way to solve the 3D on 2D image problem is to take 3D images. It can be accomplished with X-ray microtomography. The only restriction is that the samples must be sufficiently small to let the X-rays pass trough the sample. Else, the metallic particles would absorb all the rays. Additionally, using an X-ray microtomography might be expensive.

The selection algorithm proposed includes the findings of this work, consideration from the literature and considerations of general knowledge of the BJ printing process. However, it does not take into account important factors related to the binder penetration time into the powder bed and the primitive formation. Additionally, debinding and sintering selection aspects are not integrated into the algorithm yet: factors such as debinding and sintering times and temperatures. These considerations are the focus of the work of two colleagues. The overall findings will be integrated in a future work. As it is, this is the firs algorithm that brings polymer - polymer and metal - polymer interactions into consideration.

All things considered, this work led to the elucidation of new binder selection criteria, a method to prepare green bodies without stopping production and using less material and a binder selection algorithm. The three aspects can be used for binder selection or modification for BJ applications, but also, for other binder-based 3D printing techniques such as direct ink writing and material jetting.

CHAPTER 5 CONCLUSION AND RECOMMANDATIONS

Even though the selection of binders is a major concern in BJ printing, it is mainly done by trial and error. The existing binder selection algorithms are mostly centered on the printhead specifications and they neglect the polymer-polymer and polymer-metal interactions. Therefore, the main objective of this work is to elucidate the interactions giving strength to the pieces in order to use them in a selection algorithm as binder selection guidelines. To accomplish this, first, a method to prepare green bodies without using a BJ printer was developed. The method consists in manually mixing the green body ingredients to obtain a paste. The paste is pushed into a cylindrical mould and left to dry. After demoulding, the strength of the samples was carefully studied with compression tests. The 0.2 % yield strength of the samples was the parameter of interest. SS 316L samples made with PVA, PVP and PAA binders with and without additives were studied with this technique. The experiments led to the formulation of a model curve of the relation between green strength and binder content in the pieces. Finally, the impact of molecular weight, polymer functionality and the presence of a crosslinker agent and a proprietary ink in the binder formulation were studied. In the following section, the polymer - polymer and metal - polymer interactions elucidated in this project and their key role on green strength are summarized.

5.1 Summary of key findings

Fill factor. The fill factor is a good metric to characterize the behavior of the green bodies as a function of binder concentration. It is an indicator of how much void in the piece is replaced by dry binder. As fill factor increases, the strength of the pieces increases. However, there are three different strength increase regimes. First, in region A, there is an induction period, where interparticle bonds are not yet formed. Then, in region B, there is an interparticle network strengthening region, where interparticle bridges get thicker and more of them are formed. Finally, in region C, the void space of the piece starts to saturate, and the properties of the green bodies tend to the pure binder strength. Thanks to the analysis made with the help of this parameter. Three new binder selection criteria were enunciated: Pendular bond formation at low fill factor, fast transition to the bond thickening regime and fast strength increase with the fill factor. These criteria are dominated by the pure polymer strength the efficiency of the binder distribution. According to eq. (4.4, the fill factor increases if the binder concentration increases, if the packing density of the powder bed increases and if the binder density decreases.

Pure polymer strength. The strength of the green bodies is determined by the strength of the pure polymer (see also appendix F). In fact, green strength is only a fraction of the pure polymer strength: $\sigma_{green} = x\sigma_{polymer}$. As the fill factor increases x, increases, until it reaches 100 %. Additionally, a high polymer strength results in a shorter induction period and a high increase of strength as a function of the fill factor.

Cohesive polymer failure. It is important to have a binder that fails in its bulk phase and not at the interphase, as adhesive failure means that the body is not reaching its maximum strength. Cohesive failure can be obtained by choosing a polymer containing functional groups capable of reacting with the metallic surface. In this study, we have shown than cohesive failure is possible in systems bonded by covalent bonds and by hydrogen bonds. In fact, hydrogen bond systems performed better. If the polymer does not have affinity with the metal, one can use coupling agents such as small molecules or copolymers to improve the affinity, which is a compatibilization technique widely used in adhesion science [181, 182].

Binder distribution. The binder must deposit only at the necking regions so that all of it is used in forming the interparticle pendular bridges. This allows a faster formation of the interparticle bonds and faster thickening of them as a function of the fill factor. It depends on the physicochemical properties of the binder and their relation to the capillary number Ca. Lower capillary numbers favor pendular bond formation. Pendular bond formation also depends on the affinity of the binder with the metal surface. If they are too compatible, the polymer will tend to deposit over the entire metallic surface (coated regime).

Molecular weight. The molecular weight must be higher than the entanglement molecular weight. Else, it cannot confer strength to the green bodies. This parameter has an impact on the green strength, the viscosity, surface tension and degradability of the binder. It can be used to tune one of those parameters. However, result show that the improvement of strength due to a M_w increase is not as important as what can be achieved by toning the fill factor. Therefore, it is more useful to use M_w to adjust the rheological properties of the binder.

Adsorption. The interaction of the binder with the metallic surface must be weaker than the CED of the solution while the liquid is not located at the interparticle necking regions. Else, the binder could be wasted, as it will start depositing outside the regions of interest. Additionally, if the binder is too concentrated, there is an early precipitation effect. Finally, one should note that additives can compete with the main binder ingredient to adsorb on the metallic surface. This

competitive adsorption can reduce the strength of the interparticle bridges at the particle binder interphase.

pH. The pH of the binder can change the reactivity of the binder with the metal surface. It changes the properties of the surface and those of the polymer. This needs to be assessed on a case-by-case basis, as it is controlled by the isoelectric point of the metal, the chemical species on its surface and the polymer's pK_a.

Crosslinkers. The addition of small amounts of a crosslinking agents (< 0.2 wt. % in this case) can significantly enhance the green strength. This is often done with molecules that need an energy input to cure [36, 57], which makes the printing process longer. However, our results show that a significant improvement of green strength can be obtained with physically crosslinked binders. It should be noted, that after a threshold concentration, the crosslinker starts having a negative effect on strength.

General note. Due to the high amount of ingredients in a binder formulation (Table 2.2), it is very important to assess the impact of each one of them on the green strength separately. The results on the effect of the ink show how detrimental a new ingredient can be.

5.2 Limits encountered and future work

The green body preparation method is simple and results in accurate and repeatable data. However, there is room for improvement. The ingredient mixing and the pressure applied while moulding were not studied. Since they might have an impact on the final green properties, it would be useful to ameliorate those preparation steps. A specialized mixing equipment like a mill could be used and the forming pressure could be controlled with weights.

It was suggested to keep track of the type of bond between the polymer and the metal to predict if the binder would form pendular bridges or not. However, that parameter was not directly investigated in this project. Therefore, Infrared and X-ray photoelectron spectroscopies could be used to investigate the type of bond between the polymer and the metal, and the results could be related to the type of network formed. It could serve to confirm this hypothesis. Similarly, the CED seems to be a good indicator of the possibility of forming pendular bridges. It would be useful to study the range of values of CED that result in a pendular network.

Concerning the mechanical testing and the strength models, the compression test coupled with an analysis of the 0.2 % yield strength is the best way of characterizing green strength. Additionally, the cylindrical beam model seems to be in agreement with the experimental results. That said, including more test methods such as the flexural test and more models to the analysis such as Onoda's model and the thick cylinder model could result in a more complete understanding of failure mechanisms in the green bodies.

Another limit encountered is related to the SEM images and the difficulty of analyzing 2D images of 3D objects. Although the results obtained with SEM images are very compelling, it would be interesting to confirm the observations with the help of another imaging techniques such as X-ray microtomography scan or atomic force microscopy.

Considering the algorithm proposed, there are several steps that require further studies. The CED, the type of polymer - metal interaction and the effect of the fill factor must be linked to other aspects of the printing process: powder penetration, printability, debinding, sintering and final properties.

From a practical point of view, the equipment used to characterize the samples of this study is not accessible for anyone. In fact, SEM images were used to verify that the binder forms adequate bridges and a specialized electromechanical testing system was used to preform the compression tests. Simpler and less expensive methods need to be developed in order to be able to use the algorithm freely in the industry.

Finally, some additional ideas are the study of a correlation between polymer thin film formation and fill factor and the study of the binder ingredients compatibility based on Hansen solubility parameters and its impact on green strength. All these supplementary studies would certainly improve the algorithm proposed. Subsequently, its performance should be tested with a case study, preferably with another powder material.

REFERENCES

[1] All3DP. "2020 Most Common 3D Printer File Formats." https://all3dp.com/1/3d-printer-file-format/ (accessed May 18th, 2020).

[2] S. F. Shirazi *et al.*, "A review on powder-based additive manufacturing for tissue engineering: selective laser sintering and inkjet 3D printing," *Sci Technol Adv Mater,* vol. 16, no. 3, p. 033502, Jun 2015, doi: 10.1088/1468-6996/16/3/033502.

[3] H. Jee, "Preparation of "Ready-Made STL (RMS)" for build assurance in additive metal manufacturing (AMM): A review," *Journal of Mechanical Science and Technology,* vol. 33, no. 12, pp. 5643-5652, 2019.

[4] I. Gibson, D. W. Rosen, and B. Stucker, *Additive manufacturing technologies*. Springer, 2014.

[5] M. Srivastava, S. Rathee, S. Maheshwari, and T. Kundra, *Additive Manufacturing: Fundamentals and Advancements*. CRC Press, 2019.

[6] S. A. Tofail, E. P. Koumoulos, A. Bandyopadhyay, S. Bose, L. O'Donoghue, and C. Charitidis, "Additive manufacturing: Scientific and technological challenges, market uptake and opportunities," *Materials today,* vol. 21, no. 1, pp. 22-37, 2018.

[7] A. Bandyopadhyay and S. Bose, *Additive manufacturing*. CRC press, 2019.

[8] S. Ford and M. Despeisse, "Additive manufacturing and sustainability: an exploratory study of the advantages and challenges," *Journal of Cleaner Production,* vol. 137, pp. 1573-1587, 2016.

[9] M. Fera, R. Macchiaroli, F. Fruggiero, and A. Lambiase, "A new perspective for production process analysis using additive manufacturing—complexity vs production volume," *The International Journal of Advanced Manufacturing Technology,* vol. 95, no. 1-4, pp. 673-685, 2018.

[10] P. K. Gokuldoss, S. Kolla, and J. Eckert, "Additive manufacturing processes: Selective laser melting, electron beam melting and binder jetting—Selection guidelines," *Materials,* vol. 10, no. 6, p. 672, 2017.

[11] T. Peng, K. Kellens, R. Tang, C. Chen, and G. Chen, "Sustainability of additive manufacturing: An overview on its energy demand and environmental impact," *Additive Manufacturing,* vol. 21, pp. 694-704, 2018.

[12] M. Merklein, D. Junker, A. Schaub, and F. Neubauer, "Hybrid additive manufacturing technologies–an analysis regarding potentials and applications," *Physics Procedia,* vol. 83, pp. 549-559, 2016.

[13] M. PETCH. "3D PRINTING COMMUNITY RESPONDS TO COVID-19 AND CORONAVIRUS RESOURCES." https://3dprintingindustry.com/news/3d-printing-community-responds-to-covid-19-and-coronavirus-resources-169143/ (accessed 23-05, 2020).

[14] J.-Y. Lee, J. An, and C. K. Chua, "Fundamentals and applications of 3D printing for novel materials," *Applied Materials Today,* vol. 7, pp. 120-133, 2017.

[15] S. Mirzababaei and S. Pasebani, "A Review on Binder Jet Additive Manufacturing of 316L Stainless Steel," *Journal of Manufacturing and Materials Processing,* vol. 3, no. 3, p. 82, 2019.

[16] W. Du, X. Ren, C. Ma, and Z. Pei, "Binder jetting additive manufacturing of ceramics: a literature review," in *ASME 2017 International Mechanical Engineering Congress and Exposition*, 2017: American Society of Mechanical Engineers Digital Collection.

[17] M. Song *et al.*, "Water-soluble binder with high flexural modulus for powder injection molding," *Journal of Materials Science,* journal article vol. 40, no. 5, pp. 1105-1109, March 01 2005, doi: 10.1007/s10853-005-6924-2.

[18] C. Xu, "Solvent cast direct ink writing of mesoscale metallic structures," Ph. D. Dissertation, Mechanical Engineering, Polytechnique Montréal, 2018.

[19] R. Castro and K. Van Benthem, *Sintering: mechanisms of convention nanodensification and field assisted processes*. Springer Science & Business Media, 2012.

[20] P. Dougherty, "New Materials for Binder Jetting: High-demand Alloys," *Oral presentation at the ExOne Global Inovation Event: Binder jet 3D Printing,* May 27, 2020.

[21] R. Berger, "Additive manufacturing: a game changer for the manufacturing industry," *Roland Berger Strategy Consultants GmbH, Munich,* vol. 1, no. 5.1, 2013.

[22] R. M. Sachanandani and S. J. Lombardo, "Effect of green body size and heating rate on failure during thermal debinding and on the debinding cycle time," *Journal of Ceramic Processing Research,* vol. 12, no. 2, pp. 115-121, 2011.

[23] H. Miyanaji, M. Orth, J. M. Akbar, and L. Yang, "Process development for green part printing using binder jetting additive manufacturing," *Frontiers of Mechanical Engineering,* vol. 13, no. 4, pp. 504-512, 2018.

[24] C. B. Williams, "Design and development of a layer-based additive manufacturing process for the realization of metal parts of designed mesostructure," Georgia Institute of Technology, 2008.

[25] Y. Bai, C. Wall, H. Pham, A. Esker, and C. B. Williams, "Characterizing Binder–Powder Interaction in Binder Jetting Additive Manufacturing Via Sessile Drop Goniometry," *Journal of Manufacturing Science and Engineering,* vol. 141, no. 1, 2018, doi: 10.1115/1.4041624.

[26] B. Derby, "Inkjet printing ceramics: From drops to solid," *Journal of the European Ceramic Society,* vol. 31, no. 14, pp. 2543-2550, 2011.

[27] S. K. Tam, K. Y. Fung, G. S. H. Poon, and K. M. Ng, "Product design: Metal nanoparticle-based conductive inkjet inks," *AIChE Journal,* vol. 62, no. 8, pp. 2740-2753, 2016.

[28] H. Miyanaji, S. Zhang, and L. Yang, "A new physics-based model for equilibrium saturation determination in binder jetting additive manufacturing process," *International Journal of Machine Tools and Manufacture,* vol. 124, pp. 1-11, 2018, doi: 10.1016/j.ijmachtools.2017.09.001.

[29] E. M. Wilts, D. Ma, Y. Bai, C. B. Williams, and T. E. Long, "Comparison of Linear and 4-Arm Star Poly (vinyl pyrrolidone) for Aqueous Binder Jetting Additive Manufacturing of Personalized Dosage Tablets," *ACS applied materials & interfaces,* vol. 11, no. 27, pp. 23938-23947, 2019.

[30] G. E. Cossali, A. Coghe, and M. Marengo, "The impact of a single drop on a wetted solid surface," *Experiments in fluids,* vol. 22, no. 6, pp. 463-472, 1997.

[31] B. Utela, D. Storti, R. Anderson, and M. Ganter, "A review of process development steps for new material systems in three dimensional printing (3DP)," *Journal of Manufacturing Processes,* vol. 10, no. 2, pp. 96-104, 2008, doi: 10.1016/j.jmapro.2009.03.002.

[32] B. R. Utela, D. Storti, R. L. Anderson, and M. Ganter, "Development Process for Custom Three-Dimensional Printing (3DP) Material Systems," *Journal of Manufacturing Science and Engineering,* vol. 132, no. 1, 2010, doi: 10.1115/1.4000713.

[33] M. Li, L. Zhang, D. Wang, C. Agbo, and S. Fu, "Influence of nano-coated pigment ink formulation on ink-jet printability and printing accuracy," *Coloration Technology,* vol. 133, no. 6, pp. 476-484, 2017.

[34] M. Ziaee and N. B. Crane, "Binder Jetting: A Review of Process, Materials, and Methods," *Additive Manufacturing,* 2019.

[35] M. A. Behjani, A. Hassanpour, M. Ghadiri, and A. Bayly, "Numerical analysis of the effect of particle shape and adhesion on the segregation of powder mixtures," in *EPJ Web of Conferences*, 2017, vol. 140: EDP Sciences, p. 06024.

[36] S. A. Uhland, R. K. Holman, S. Morissette, M. J. Cima, and E. M. Sachs, "Strength of green ceramics with low binder content," *Journal of the American Ceramic Society,* vol. 84, no. 12, pp. 2809-2818, 2001.

[37] W.-H. Lee, D.-S. Kim, J.-S. Kim, T.-M. Lee, D.-Y. Shin, and M.-C. Lee, "Strength and processing Properties using a Photopolymer Resin in a Powder-based 3DP Process," in *2006 SICE-ICASE International Joint Conference*, 2006: IEEE, pp. 3674-3677.

[38] A. Mostafaei *et al.*, "Binder jet 3D printing–process parameters, materials, properties, and challenges," *Progress in Materials Science,* p. 100707, 2020.

[39] A. Lores, N. Azurmendi, I. Agote, and E. Zuza, "A review on recent developments in binder jetting metal additive manufacturing: materials and process characteristics," *Powder Metallurgy,* vol. 62, no. 5, pp. 267-296, 2019.

[40] Y. Mao, J. Li, W. Li, D. Cai, and Q. Wei, "Binder jetting additive manufacturing of 316 L stainless-steel green parts with high strength and low binder content: binder preparation and process optimization," *Journal of Materials Processing Technology,* p. 117020, 2020.

[41] R. M. LEWIS, "Powder binder interactions in 3D inkjet printing," 2014.

[42] T. Do, P. Kwon, and C. S. Shin, "Process development toward full-density stainless steel parts with binder jetting printing," *International Journal of Machine Tools and Manufacture,* vol. 121, pp. 50-60, 2017, doi: 10.1016/j.ijmachtools.2017.04.006.

[43] A. Elliott, S. AlSalihi, A. L. Merriman, and M. M. Basti, "Infiltration of nanoparticles into porous binder jet printed parts," *American Journal of Engineering and Applied Sciences,* vol. 9, no. 1, 2016.

[44] D. Gilmer *et al.*, "An in-situ crosslinking binder for binder jet additive manufacturing," *Additive Manufacturing,* p. 101341, 2020.

[45] S. M. Allen and E. M. Sachs, "Three-dimensional printing of metal parts for tooling and other applications," *Metals and Materials,* vol. 6, no. 6, pp. 589-594, 2000.

[46] Z. C. Cordero, D. H. Siddel, W. H. Peter, and A. M. Elliott, "Strengthening of ferrous binder jet 3D printed components through bronze infiltration," *Additive Manufacturing,* vol. 15, pp. 87-92, 2017.

[47] C. B. Williams, J. K. Cochran, and D. W. Rosen, "Additive manufacturing of metallic cellular materials via three-dimensional printing," *The International Journal of Advanced Manufacturing Technology,* vol. 53, no. 1, pp. 231-239, 2011.

[48] M. M. M. Carrijo *et al.*, "Fabrication of Ti3SiC2-based composites via three-dimensional printing: Influence of processing on the final properties," *Ceramics International,* vol. 42, no. 8, pp. 9557-9564, 2016.

[49] Y. Xiong, C. Qian, and J. Sun, "Fabrication of porous titanium implants by three-dimensional printing and sintering at different temperatures," *Dental materials journal,* vol. 31, no. 5, pp. 815-820, 2012.

[50] E. Sheydaeian, Z. Fishman, M. Vlasea, and E. Toyserkani, "On the effect of throughout layer thickness variation on properties of additively manufactured cellular titanium structures," *Additive Manufacturing,* vol. 18, pp. 40-47, 2017.

[51] F. E. Wiria, S. Maleksaeedi, and Z. He, "Manufacturing and characterization of porous titanium components," *Progress in crystal growth and characterization of materials,* vol. 60, no. 3-4, pp. 94-98, 2014.

[52] B. Nan, X. Yin, L. Zhang, and L. Cheng, "Three-dimensional printing of Ti3SiC2-based ceramics," *Journal of the American Ceramic Society,* vol. 94, no. 4, pp. 969-972, 2011.

[53] X. Yin, N. Travitzky, and P. Greil, "Near-net-shape fabrication of Ti3AlC2-based composites," *International journal of applied ceramic technology,* vol. 4, no. 2, pp. 184-190, 2007.

[54] X. Yin, N. Travitzky, and P. Greil, "Three-dimensional printing of nanolaminated Ti3AlC2 toughened TiAl3–Al2O3 composites," *Journal of the American Ceramic Society,* vol. 90, no. 7, pp. 2128-2134, 2007.

[55] R. Melcher, N. Travitzky, C. Zollfrank, and P. Greil, "3D printing of Al 2 O 3/Cu–O interpenetrating phase composite," *Journal of materials science,* vol. 46, no. 5, pp. 1203-1210, 2011.

[56] M. Cima *et al.*, "Structural ceramic components by 3D printing," in *1995 International Solid Freeform Fabrication Symposium*, 1995.

[57] J. Moon, J. E. Grau, V. Knezevic, M. J. Cima, and E. M. Sachs, "Ink-jet printing of binders for ceramic components," *Journal of the American Ceramic Society,* vol. 85, no. 4, pp. 755-762, 2002.

[58] R. Melcher, S. Martins, N. Travitzky, and P. Greil, "Fabrication of Al2O3-based composites by indirect 3D-printing," *Materials Letters,* vol. 60, no. 4, pp. 572-575, 2006.

[59] S. Uhland, R. Holman, M. Cima, E. Sachs, and Y. Enokido, "New process and materials developments in 3-dimensional printing, 3DP™," *MRS Online Proceedings Library Archive,* vol. 542, 1998.

[60] S. Gupta, D. J. Green, G. L. Messing, and I. M. Peterson, "Thermomechanical behavior of ceramic green bodies during presintering," *Journal of the American Ceramic Society,* vol. 93, no. 9, pp. 2611-2616, 2010.

[61] B. D. Kernan, E. M. Sachs, M. A. Oliveira, and M. J. Cima, "Three-dimensional printing of tungsten carbide–10 wt% cobalt using a cobalt oxide precursor," *International Journal of Refractory Metals and Hard Materials,* vol. 25, no. 1, pp. 82-94, 2007.

[62] Z. Fu, L. Schlier, N. Travitzky, and P. Greil, "Three-dimensional printing of SiSiC lattice truss structures," *Materials Science and Engineering: A,* vol. 560, pp. 851-856, 2013.

[63] L. Rabinskiy, A. Ripetsky, S. Sitnikov, Y. Solyaev, and R. Kahramanov, "Fabrication of porous silicon nitride ceramics using binder jetting technology," in *IOP Conference Series: Materials Science and Engineering*, 2016, vol. 140, no. 1: IOP Publishing, p. 012023.

[64] L. Li *et al.*, "A novel method combining additive manufacturing and alloy infiltration for NdFeB bonded magnet fabrication," *Journal of Magnetism and Magnetic Materials,* vol. 438, pp. 163-167, 2017.

[65] Q. Wei, Y. Wang, W. Chai, Y. Zhang, and X. Chen, "Molecular dynamics simulation and experimental study of the bonding properties of polymer binders in 3D powder printed hydroxyapatite bioceramic bone scaffolds," *Ceramics International,* vol. 43, no. 16, pp. 13702-13709, 2017.

[66] Z. Zhou, A. Lennon, F. Buchanan, H. O. McCarthy, and N. Dunne, "Binder jetting additive manufacturing of hydroxyapatite powders: Effects of adhesives on geometrical accuracy and green compressive strength," *Additive Manufacturing,* vol. 36, p. 101645, 2020.

[67] A. Winkel *et al.*, "Sintering of 3 D-Printed Glass/HA p Composites," *Journal of the American Ceramic Society,* vol. 95, no. 11, pp. 3387-3393, 2012.

[68] J. Suwanprateeb, R. Sanngam, W. Suvannapruk, and T. Panyathanmaporn, "Mechanical and in vitro performance of apatite–wollastonite glass ceramic reinforced hydroxyapatite composite fabricated by 3D-printing," *Journal of Materials Science: Materials in Medicine,* vol. 20, no. 6, p. 1281, 2009.

[69] J. Suwanprateeb and R. Chumnanklang, "Three-dimensional printing of porous polyethylene structure using water-based binders," *Journal of Biomedical Materials Research Part B: Applied Biomaterials: An Official Journal of The Society for Biomaterials, The Japanese Society for Biomaterials, and The Australian Society for Biomaterials and the Korean Society for Biomaterials,* vol. 78, no. 1, pp. 138-145, 2006.

[70] C. X. F. Lam, X. Mo, S.-H. Teoh, and D. Hutmacher, "Scaffold development using 3D printing with a starch-based polymer," *Materials Science and Engineering: C,* vol. 20, no. 1-2, pp. 49-56, 2002.

[71] H. Zhao, C. Ye, S. Xiong, Z. Fan, and L. Zhao, "Fabricating an effective calcium zirconate layer over the calcia grains via binder-jet 3D-printing for improving the properties of calcia ceramic cores," *Additive Manufacturing,* vol. 32, p. 101025, 2020.

[72] S. Huang, C. Ye, H. Zhao, Z. Fan, and Q. Wei, "Binder jetting yttria stabilised zirconia ceramic with inorganic colloid as a binder," *Advances in Applied Ceramics,* vol. 118, no. 8, pp. 458-465, 2019.

[73] F. K. Feenstra, "Method for making a dental element," ed: Google Patents, 2005.

[74] D. T. Brunermer, "Low Residual Carbon Binder for Binder Jetting Three-Dimensional Printing and Methods for Use of Same," ed: Google Patents, 2020.

[75] J. Liu and M. Rynerson, "METHOD FOR ARTICLE FABRICATION USING CARBOHYDRATE BINDER," U.S. Patent 6585930, 2003.

[76] K. DANJO, K. KOZAKI, H. SUNADA, and A. OTSUKA, "Influence of the molecular weight of binding agents on the physical properties of granules and tablets," *Chemical and pharmaceutical bulletin,* vol. 42, no. 10, pp. 2121-2125, 1994.

[77] I. Teraoka, *Polymer solutions*. John Wiley & Sons, Inc, 2002.

[78] A. Kamyshny and S. Magdassi, "Inkjet ink formulations," *Inkjet-Based Micromanufacturing; Korvink, JG, Smith, PJ, Shin, D.-Y., Eds,* 2012.

[79] J. F. Bredt, T. C. Anderson, and D. B. Russell, "Three dimensional printing material system and method," ed: Google Patents, 2003.

[80] M. Salehi, S. Maleksaeedi, S. M. L. Nai, G. K. Meenashisundaram, M. H. Goh, and M. Gupta, "A paradigm shift towards compositionally zero-sum binderless 3D printing of magnesium alloys via capillary-mediated bridging," *Acta Materialia,* vol. 165, pp. 294-306, 2019.

[81] E. M. Sachs, C. Hadjiloucas, S. Allen, and H. J. Yoo, "Metal and ceramic containing parts produced from powder using binders derived from salt," ed: Google Patents, 2003.

[82] L. A. Chavez *et al.*, "The Influence of Printing Parameters, Post-Processing, and Testing Conditions on the Properties of Binder Jetting Additive Manufactured Functional Ceramics," *Ceramics,* vol. 3, no. 1, pp. 65-77, 2020.

[83] P. Patirupanusara, W. Suwanpreuk, T. Rubkumintara, and J. Suwanprateeb, "Effect of binder content on the material properties of polymethyl methacrylate fabricated by three dimensional printing technique," *journal of materials processing technology,* vol. 207, no. 1-3, pp. 40-45, 2008.

[84] C. D. Willett, S. A. Johnson, M. J. Adams, and J. P. Seville, "Pendular capillary bridges," in *Handbook of Powder Technology*, vol. 11: Elsevier, 2007, pp. 1317-1351.

[85] Y. Shanjani and E. Toyserkani, "Material spreading and compaction in powder-based solid freeform fabrication methods: mathematical modeling," in *19th Annual International Solid Freeform Fabrication Symposium, SFF*, 2008, vol. 2008, pp. 399-410.

[86] A. D. Salman, G. K. Reynolds, H. S. Tan, I. Gabbott, and M. J. Hounslow, "Breakage in granulation," in *Handbook of Powder Technology*, vol. 11: Elsevier, 2007, pp. 979-1040.

[87] S. Gupta, "A Perspective on Green Body Fabrication and Design for Sustainable Manufacturing," in *Green and Sustainable Manufacturing of Advanced Material*: Elsevier, 2016, pp. 549-580.

[88] G. Y. ONODA JR, "Theoretical strength of dried green bodies with organic binders," *Journal of the American Ceramic Society,* vol. 59, no. 5-6, pp. 236-239, 1976.

[89] H. Rumpf, "The strength of granules and agglomerates," in *Agglomeration-Proceedings of the First International Symposium on Agglomeration, Philadelphia, 1962*, 1962, pp. 379-418.

[90] E. HORISAWA, A. KOMURA, K. DANJO, and A. OTSUKA, "Effect of binder characteristics on the strength of agglomerates prepared by the wet method," *Chemical and pharmaceutical bulletin,* vol. 41, no. 8, pp. 1428-1433, 1993.

[91] U. Gbureck, T. Hölzel, U. Klammert, K. Würzler, F. A. Müller, and J. E. Barralet, "Resorbable dicalcium phosphate bone substitutes prepared by 3D powder printing," *Advanced Functional Materials,* vol. 17, no. 18, pp. 3940-3945, 2007.

[92] M. Ohring, *Engineering materials science*. Elsevier, 1995.

[93] B. S. Mitchell, *An introduction to materials engineering and science for chemical and materials engineers*. John Wiley & Sons, 2004.

[94] P. van Liempt and J. Sietsma, "A physically based yield criterion I. Determination of the yield stress based on analysis of pre-yield dislocation behaviour," *Materials Science and Engineering: A,* vol. 662, pp. 80-87, 2016.

[95] A. Procopio, A. Zavaliangos, and J. Cunningham, "Analysis of the diametrical compression test and the applicability to plastically deforming materials," *Journal of Materials Science,* vol. 38, no. 17, pp. 3629-3639, 2003.

[96] T. Swift, L. Swanson, M. Geoghegan, and S. Rimmer, "The pH-responsive behaviour of poly (acrylic acid) in aqueous solution is dependent on molar mass," *Soft Matter,* vol. 12, no. 9, pp. 2542-2549, 2016.

[97] N. Ketata *et al.*, "Thermal degradation of polyurethane bicomponent systems in controlled atmospheres," *Polymers Polymer Composites,* vol. 13, no. 1, pp. 1-26, 2005.

[98] S. Atre, R. Enneti, S. Park, and R. German, "Master decomposition curve analysis of ethylene vinyl acetate pyrolysis: influence of metal powders," *Powder Metallurgy,* vol. 51, no. 4, pp. 368-375, 2008.

[99] K. Pielichowski and J. Njuguna, *Thermal degradation of polymeric materials*. iSmithers Rapra Publishing, 2005.

[100] L.-H. Lee, "Molecular Bonding and Adhesion at Polymer-Metal Interphases," *The Journal of Adhesion,* vol. 46, no. 1-4, pp. 15-38, 1994, doi: 10.1080/00218469408026646.

[101] C. Boiziau and G. Lecayon, "Adhesion of polymers to metals: A review of the results obtained studying a model system," *Surface and Interface Analysis,* vol. 12, no. 9, pp. 475-485, 1988.

[102] E. McCafferty, "Acid-Base Properties of Surface Oxide Films," in *Surface Chemistry of Aqueous Corrosion Processes*: Springer, 2015, pp. 1-54.

[103] S. Wu, "Polymer interface and adhesion," 1982.

[104] A. J. Kinloch, *Adhesion and adhesives: science and technology*. Springer Science & Business Media, 2012.

[105] I. A. Starostina, O. V. Stoyanov, and R. Y. Deberdeev, *Polymer surfaces and interfaces: Acid-base interactions and adhesion in polymer-metal systems*. Apple Academic Press, 2014.

[106] J. Friedrich, *Metal-Polymer Systems: Interface Design and Chemical Bonding*. John Wiley & Sons, 2017.

[107] J. K. L. Lai, C. H. Shek, and K. H. Lo, *Stainless steels: An introduction and their recent developments*. Bentham Science Publishers, 2012.

[108] A. Bakterij, "An overview of the influence of stainless-steel surface properties on bacterial adhesion," *Mater. Tehnol,* vol. 48, pp. 609-617, 2014.

[109] C.-O. Olsson and D. Landolt, "Passive films on stainless steels—chemistry, structure and growth," *Electrochimica acta,* vol. 48, no. 9, pp. 1093-1104, 2003.

[110] D. Weinhandl. "COMMON USES FOR STAINLESS STEEL." https://www.meadmetals.com/blog/common-uses-for-stainless-steel (accessed 2021).

[111] M. Fellah, M. Labaïz, O. Assala, A. Iost, and L. Dekhil, "Tribological behaviour of AISI 316L stainless steel for biomedical applications," *Tribology-Materials, Surfaces & Interfaces,* vol. 7, no. 3, pp. 135-149, 2013.

[112] C. Morsiya, "A review on parameters affecting properties of biomaterial SS 316L," *Australian Journal of Mechanical Engineering,* pp. 1-11, 2020.

[113] Z. Wang, A. Seyeux, S. Zanna, V. Maurice, and P. Marcus, "Chloride-induced alterations of the passive film on 316L stainless steel and blocking effect of pre-passivation," *Electrochimica Acta,* vol. 329, p. 135159, 2020.

[114] Z. Wang, E.-M. Paschalidou, A. Seyeux, S. Zanna, V. Maurice, and P. Marcus, "Mechanisms of Cr and Mo enrichments in the passive oxide film on 316L austenitic stainless steel," *Frontiers in Materials,* vol. 6, p. 232, 2019.

[115] D. Riabov, E. Hryha, M. Rashidi, S. Bengtsson, and L. Nyborg, "Effect of atomization on surface oxide composition in 316L stainless steel powders for additive manufacturing," *Surface and Interface Analysis,* vol. 52, no. 11, pp. 694-706, 2020.

[116] G. Lefèvre, L. Čerović, S. Milonjić, M. Fédoroff, J. Finne, and A. Jaubertie, "Determination of isoelectric points of metals and metallic alloys by adhesion of latex particles," *Journal of colloid and interface science,* vol. 337, no. 2, pp. 449-455, 2009.

[117] A. Raman, R. Quiñones, L. Barriger, R. Eastman, A. Parsi, and E. S. Gawalt, "Understanding organic film behavior on alloy and metal oxides," *Langmuir,* vol. 26, no. 3, pp. 1747-1754, 2010.

[118] K. Takahashi and S. Fukuzaki, "Cleanability of titanium and stainless steel particles in relation to surface charge aspects," *Biocontrol science,* vol. 13, no. 1, pp. 9-16, 2008.

[119] M. R. B. Romdhane, T. Chartier, S. Baklouti, J. Bouaziz, C. Pagnoux, and J.-F. Baumard, "A new processing aid for dry-pressing: a copolymer acting as dispersant and binder," *Journal of the European Ceramic Society,* vol. 27, no. 7, pp. 2687-2695, 2007.

[120] R. J. Young and P. A. Lovell, C. a. Hall, Ed. *Introduction to polymers*, 2nd ed. London, 1991.

[121] A. Agasty, A. Wisniewska, T. Kalwarczyk, K. Koynov, and R. Holyst, "Scaling equation for viscosity of polydimethylsiloxane in ethyl acetate: From dilute to concentrated solutions," *Polymer,* vol. 203, p. 122779, 2020.

[122] G. Cuvelier and B. Launay, "Concentration regimes in xanthan gum solutions deduced from flow and viscoelastic properties," *Carbohydrate Polymers,* vol. 6, no. 5, pp. 321-333, 1986.

[123] A. Norton, R. Hancocks, and L. Grover, "Poly (vinyl alcohol) modification of low acyl gellan hydrogels for applications in tissue regeneration," *Food Hydrocolloids,* vol. 42, pp. 373-377, 2014.

[124] R. Y. Lochhead and C. J. Rulison, "An investigation of the mechanism by which hydrophobically modified hydrophilic polymers act as primary emulsifiers for oil-in-water emulsions 1. Poly (acrylic acids) and hydroxyethyl celluloses," *Colloids and Surfaces A: Physicochemical and Engineering Aspects,* vol. 88, no. 1, pp. 27-32, 1994.

[125] G. Cheng, W. Graessley, and Y. Melnichenko, "Polymer dimensions in good solvents: crossover from semidilute to concentrated solutions," *Physical review letters,* vol. 102, no. 15, p. 157801, 2009.

[126] S. Westermann, L. Willner, D. Richter, and L. J. Fetters, "The evaluation of polyethylene chain dimensions as a function of concentration in nonadecane," *Macromolecular Chemistry and Physics,* vol. 201, no. 5, pp. 500-504, 2000.

[127] R. A. Pethrick, T. Amornsakchai, and A. M. North, *Introduction to molecular motion in polymers*. Whittles, 2011.

[128] G. Odian, *Principles of polymerization*. John Wiley & Sons, 2004.

[129] C. CRETON and P. FABRE, "Tack," in *Adhesion science and engineering*: Elsevier, 2002, pp. 535-575.

[130] S. Ghoshal, P. Denner, S. Stapf, and C. Mattea, "Study of the formation of poly (vinyl alcohol) films," *Macromolecules,* vol. 45, no. 4, pp. 1913-1923, 2012.

[131] N. Karimi, "Direct laser writing of fluorescent microstructures containing silver nanoclusters in polyvinyl alcohol films," 2015.

[132] T. S. Gaaz, A. B. Sulong, M. N. Akhtar, A. A. H. Kadhum, A. B. Mohamad, and A. A. Al-Amiery, "Properties and applications of polyvinyl alcohol, halloysite nanotubes and their nanocomposites," *Molecules,* vol. 20, no. 12, pp. 22833-22847, 2015.

[133] X. Gong, C. Y. Tang, L. Pan, Z. Hao, and C. P. Tsui, "Characterization of poly (vinyl alcohol)(PVA)/ZnO nanocomposites prepared by a one-pot method," *Composites Part B: Engineering,* vol. 60, pp. 144-149, 2014.

[134] M. I. Baker, S. P. Walsh, Z. Schwartz, and B. D. Boyan, "A review of polyvinyl alcohol and its uses in cartilage and orthopedic applications," *Journal of Biomedical Materials Research Part B: Applied Biomaterials,* vol. 100, no. 5, pp. 1451-1457, 2012.

[135] S. Kayal and R. Ramanujan, "Doxorubicin loaded PVA coated iron oxide nanoparticles for targeted drug delivery," *Materials Science and Engineering: C,* vol. 30, no. 3, pp. 484-490, 2010.

[136] M. Kozlov and T. J. McCarthy, "Adsorption of poly (vinyl alcohol) from water to a hydrophobic surface: effects of molecular weight, degree of hydrolysis, salt, and temperature," *Langmuir,* vol. 20, no. 21, pp. 9170-9176, 2004.

[137] L. Leibler, E. Pezron, and P. Pincus, "Viscosity behaviour of polymer solutions in the presence of complexing ions," *Polymer,* vol. 29, no. 6, pp. 1105-1109, 1988.

[138] H.-L. Lin, W.-H. Liu, Y.-F. Liu, and C.-H. Cheng, "Complexation equilibrium constants of poly (vinyl alcohol)-borax dilute aqueous solutions–consideration of electrostatic charge repulsion and free ions charge shielding effect," *Journal of Polymer Research,* vol. 9, no. 4, pp. 233-238, 2002.

[139] C. Y. Chen and T.-L. Yu, "Dynamic light scattering of poly (vinyl alcohol)-borax aqueous solution near overlap concentration," *Polymer,* vol. 38, no. 9, pp. 2019-2025, 1997.

[140] M. B. Lawrence, J. Desa, and V. Aswal, "Reentrant behaviour in polyvinyl alcohol–borax hydrogels," *Materials Research Express,* vol. 5, no. 1, p. 015315, 2018.

[141] G. Keita and A. Ricard, "Phase diagram of borate-PVA system: sol-gel transition and demixtion," *Polymer bulletin,* vol. 24, no. 6, pp. 633-640, 1990.

[142] P. Hiremath, K. Nuguru, and V. Agrahari, "Material attributes and their impact on wet granulation process performance," in *Handbook of pharmaceutical wet granulation*: Elsevier, 2019, pp. 263-315.

[143] T. Dürig and K. Karan, "Binders in wet granulation," in *Handbook of Pharmaceutical Wet Granulation*: Elsevier, 2019, pp. 317-349.

[144] K. M. Koczkur, S. Mourdikoudis, L. Polavarapu, and S. E. Skrabalak, "Polyvinylpyrrolidone (PVP) in nanoparticle synthesis," *Dalton Transactions,* vol. 44, no. 41, pp. 17883-17905, 2015.

[145] A. E. Jablonski, A. J. Lang, and S. Vyazovkin, "Isoconversional kinetics of degradation of polyvinylpyrrolidone used as a matrix for ammonium nitrate stabilization," *Thermochimica acta,* vol. 474, no. 1-2, pp. 78-80, 2008.

[146] S. J. Trenfield, C. M. Madla, A. W. Basit, and S. Gaisford, "Binder jet printing in pharmaceutical manufacturing," in *3D Printing of Pharmaceuticals*: Springer, 2018, pp. 41-54.

[147] Q. Wei, Y. Zhang, Y. Wang, W. Chai, and M. Yang, "Measurement and modeling of the effect of composition ratios on the properties of poly (vinyl alcohol)/poly (vinyl pyrrolidone) membranes," *Materials & Design,* vol. 103, pp. 249-258, 2016.

[148] P. Gupta, R. Thilagavathi, A. K. Chakraborti, and A. K. Bansal, "Role of molecular interaction in stability of celecoxib− PVP amorphous systems," *Molecular pharmaceutics,* vol. 2, no. 5, pp. 384-391, 2005.

[149] E. Spruijt, P. Biesheuvel, and W. M. de Vos, "Adsorption of charged and neutral polymer chains on silica surfaces: The role of electrostatics, volume exclusion, and hydrogen bonding," *Physical Review E,* vol. 91, no. 1, p. 012601, 2015.

[150] S. P. Pandey, T. Shukla, V. K. Dhote, D. K. Mishra, R. Maheshwari, and R. K. Tekade, "Use of polymers in controlled release of active agents," in *Basic Fundamentals of Drug Delivery*: Elsevier, 2019, pp. 113-172.

[151] X. Hu, H. Tan, P. Chen, X. Wang, and J. Pang, "Polymer micelles laden hydrogel contact lenses for ophthalmic drug delivery," *Journal of nanoscience and nanotechnology,* vol. 16, no. 6, pp. 5480-5488, 2016.

[152] X. Hu *et al.*, "Preparation and characterization of a novel pH-sensitive Salecan-g-poly (acrylic acid) hydrogel for controlled release of doxorubicin," *Journal of materials chemistry B,* vol. 3, no. 13, pp. 2685-2697, 2015.

[153] S. V. Ebadi *et al.*, "Immobilization of acetylcholinesterase on electrospun poly (acrylic acid)/multi-walled carbon nanotube nanofibrous membranes," *RSC Advances,* vol. 5, no. 53, pp. 42572-42579, 2015.

[154] R. G. Riley *et al.*, "An investigation of mucus/polymer rheological synergism using synthesised and characterised poly (acrylic acid) s," *International journal of pharmaceutics,* vol. 217, no. 1-2, pp. 87-100, 2001.

[155] S. P. Pujari, L. Scheres, A. T. Marcelis, and H. Zuilhof, "Covalent surface modification of oxide surfaces," *Angewandte Chemie International Edition,* vol. 53, no. 25, pp. 6322-6356, 2014.

[156] R. P. de Castro Costa, D. A. L. de Oliveira, F. R. Marciano, and V. J. Trava-Airoldi, "Tribological Behavior of DLC Films in Space and Automotive Oil under Boundary Lubrication," *Journal of Aerospace Engineering,* vol. 4, no. 1, p. 104, 2012.

[157] M. Petretta, G. Desando, B. Grigolo, and L. Roseti, "3D printing of musculoskeletal tissues: impact on safety and health at work," *Journal of Toxicology and Environmental Health, Part A,* vol. 82, no. 16, pp. 891-912, 2019.

[158] M. Kobayashi and H. S. Hyu, "Development and evaluation of polyvinyl alcohol-hydrogels as an artificial atrticular cartilage for orthopedic implants," *Materials,* vol. 3, no. 4, pp. 2753-2771, 2010.

[159] T. Liu *et al.*, "Hydrogen-bonded polymer–small molecule complexes with tunable mechanical properties," *Macromolecular Rapid Communications,* vol. 39, no. 9, p. 1800050, 2018.

[160] C. Peng and G. Chen, "Preparation and assessment of heat-treated α-chitin nanowhiskers reinforced poly (viny alcohol) film for packaging application," *Materials,* vol. 11, no. 10, p. 1883, 2018.

[161] R. Liu *et al.*, "Preparation of polyacrylic acid-grafted-acryloyl/hemicellulose (PAA-g-AH) hybrid films with high oxygen barrier performance," *Carbohydrate polymers,* vol. 205, pp. 83-88, 2019.

[162] C. Liu, C. Xiao, and H. Liang, "Properties and structure of PVP–lignin “blend films”," *Journal of Applied Polymer Science,* vol. 95, no. 6, pp. 1405-1411, 2005.

[163] M. Ioelovich, "Finding of Relationships between Cohesive Energy, Glass Transition Temperature and Melting Point for Various Polymers."

[164] C. Merişanu, A. Samide, G. E. Iacobescu, B. Tutunaru, C. Tigae, and A. Popescu, "Anticorrosive Performance of Vinyl Butyral-co-vinyl alcohol-co-vinyl Acetate Based Copolymer Adsorbed on Steel Surfaces. Electrochemical and AFM Studies," *Int. J. Electrochem. Sci,* vol. 15, pp. 10197-10211, 2020.

[165] J. Zhao and G. Ghebremeskel, "A review of some of the factors affecting fracture and fatigue in SBR and BR vulcanizates," *Rubber chemistry and technology,* vol. 74, no. 3, pp. 409-427, 2001.

[166] P. Smith, P. J. Lemstra, and J. P. Pijpers, "Tensile strength of highly oriented polyethylene. II. Effect of molecular weight distribution," *Journal of Polymer Science: Polymer Physics Edition,* vol. 20, no. 12, pp. 2229-2241, 1982.

[167] C. M. Chan *et al.*, "Composites of wood and biodegradable thermoplastics: A review," *Polymer Reviews,* vol. 58, no. 3, pp. 444-494, 2018.

[168] N. Cao, X. Yang, and Y. Fu, "Effects of various plasticizers on mechanical and water vapor barrier properties of gelatin films," *Food hydrocolloids,* vol. 23, no. 3, pp. 729-735, 2009.

[169] Z. Czech, "Crosslinking of pressure sensitive adhesive based on water-borne acrylate," *Polymer International,* vol. 52, no. 3, pp. 347-357, 2003.

[170] F. Awaja, M. Gilbert, G. Kelly, B. Fox, and P. J. Pigram, "Adhesion of polymers," *Progress in polymer science,* vol. 34, no. 9, pp. 948-968, 2009.

[171] H. H. Cornish, K. J. Hahn, and M. L. Barth, "Experimental toxicology of pyrolysis and combustion hazards," *Environmental health perspectives,* vol. 11, pp. 191-196, 1975.

[172] T. J. Carneim and D. J. Green, "Mechanical properties of dry-pressed alumina green bodies," *Journal of the American Ceramic Society,* vol. 84, no. 7, pp. 1405-1410, 2001.

[173] S. Baklouti, T. Chartier, C. Gault, and J. F. Baumard, "The effect of binders on the strength and Young's modulus of dry pressed alumina," *Journal of the European Ceramic Society,* vol. 18, no. 4, pp. 323-328, 1998.

[174] Polymerdatabase. "Polyvinyl alcohol." https://polymerdatabase.com/polymers/polyvinylalcohol.html (accessed.

[175] Polymerdatabase. "Poly(acrylic acid)." https://polymerdatabase.com/polymers/polyacrylicacid.html (accessed.

[176] C. T. Lo and K. H. Tsui, "The dispersion of magnetic nanorods in poly (2-vinylpyridine)," *Polymer international,* vol. 62, no. 11, pp. 1652-1658, 2013.

[177] A. Eisenberg, T. Yokoyama, and E. Sambalido, "Dehydration kinetics and glass transition of poly (acrylic acid)," *Journal of Polymer Science Part A-1: Polymer Chemistry,* vol. 7, no. 7, pp. 1717-1728, 1969.

[178] M. D. P. Buera, G. Levi, and M. Karel, "Glass transition in poly (vinylpyrrolidone): effect of molecular weight and diluents," *Biotechnology progress,* vol. 8, no. 2, pp. 144-148, 1992.

[179] B. Wang *et al.*, "Evaluate the ability of PVP to inhibit crystallization of amorphous solid dispersions by density functional theory and experimental verify," *European Journal of Pharmaceutical Sciences,* vol. 96, pp. 45-52, 2017.

[180] C. H. Chu and B. Berner, "Thermal analysis of Poly (acrylic acid)/Poly (oxyethylene) blends," *Journal of applied polymer science,* vol. 47, no. 6, pp. 1083-1087, 1993.

[181] H. Yamabe, "Stabilization of the polymer-metal interface," *ProgreSs in organic coatings,* vol. 28, no. 1, pp. 9-15, 1996.

[182] M. A. Chen, X. M. Zhang, R. Huang, and X. B. Lu, "Mechanism of adhesion promotion between aluminium sheet and polypropylene with maleic anhydride-grafted polypropylene by γ-aminopropyltriethoxy silane," *Surface and Interface Analysis: An International Journal devoted to the development and application of techniques for the analysis of surfaces, interfaces and thin films,* vol. 40, no. 8, pp. 1209-1218, 2008.

[183] P. J. Bártolo, *Stereolithography: materials, processes and applications*. Springer Science & Business Media, 2011.

[184] J. W. Halloran, M. Griffith, and T.-M. Chu, "Stereolithography resin for rapid prototyping of ceramics and metals," U.S. Patent 6,117,612, 2000.

[185] M. He, Y. Zhao, B. Wang, Q. Xi, J. Zhou, and Z. Liang, "3D printing fabrication of amorphous thermoelectric materials with ultralow thermal conductivity," *Small,* vol. 11, no. 44, pp. 5889-5894, 2015.

[186] J. Gonzalez-Gutierrez, S. Cano, S. Schuschnigg, C. Kukla, J. Sapkota, and C. Holzer, "Additive manufacturing of metallic and ceramic components by the material extrusion of highly-filled polymers: A review and future perspectives," *Materials,* vol. 11, no. 5, p. 840, 2018.

[187] K. Rane and M. Strano, "A comprehensive review of extrusion-based additive manufacturing processes for rapid production of metallic and ceramic parts," *Advances in Manufacturing,* vol. 7, no. 2, pp. 155-173, 2019.

[188] 3DEO. "Metal 3D Printing Processes - Metal Extrusion FFF/FDM." https://news.3deo.co/metal-3d-printing-processes-fdm-fff (accessed June 2nd, 2020).

[189] Y. Idell, N. Watkins, A. Pascall, J. Jeffries, and K. Blobaum, "Microstructural Characterization of Pure Tin Produced by the Drop-on-Demand Technique of Liquid Metal Jetting," *Metallurgical and Materials Transactions A,* vol. 50, no. 9, pp. 4000-4005, 2019.

[190] S. H. Ko, J. Chung, N. Hotz, K. H. Nam, and C. P. Grigoropoulos, "Metal nanoparticle direct inkjet printing for low-temperature 3D micro metal structure fabrication," *Journal of Micromechanics and Microengineering,* vol. 20, no. 12, p. 125010, 2010.

[191] 3DEO. "Intro to Metal Additive Manufacturing (AM) Processes - Material Jetting." https://news.3deo.co/intro-to-metal-additive-manufacturing-am-processes-material-jetting#:~:text=Disadvantages%20of%20Material%20Jetting,appear%20to%20be%20rather%20small. (accessed june 1st, 2020).

[192] D. Godlinski and S. Morvan, "Steel parts with tailored material gradients by 3D-printing using nano-particulate ink," in *Materials Science Forum*, 2005, vol. 492: Trans Tech Publ, pp. 679-684.

[193] 3DEO. "Metal Additive Manufacturing (AM) Processes - Binder Jetting." https://news.3deo.co/metal-additive-manufacturing-am-processes-binder-jetting (accessed.

[194] Y. Zhang *et al.*, "Additive manufacturing of metallic materials: a review," *Journal of Materials Engineering and Performance,* vol. 27, no. 1, pp. 1-13, 2018.

[195] 3Dexperience. "Impression 3D : Additive." https://make.3dexperience.3ds.com/processes/3D-printing (accessed june 6th, 2020).

[196] N. Guo and M. C. Leu, "Additive manufacturing: technology, applications and research needs," *Frontiers of Mechanical Engineering,* vol. 8, no. 3, pp. 215-243, 2013.

[197] W. E. Frazier, "Metal additive manufacturing: a review," *Journal of Materials Engineering and Performance,* vol. 23, no. 6, pp. 1917-1928, 2014.

[198] A. Basak and S. Das, "Epitaxy and Microstructure Evolution in Metal Additive Manufacturing," *Annual Review of Materials Research,* vol. 46, no. 1, pp. 125-149, 2016, doi: 10.1146/annurev-matsci-070115-031728.

[199] I. Wright. "The What, Why and How of 5-Axis CNC Machining." https://www.engineering.com/CAM/ArticleID/11930/The-What-Why-and-How-of-5-Axis-CNC-Machining.aspx (accessed 28 June, 2020).

[200] T. T. Roehling *et al.*, "Modulating laser intensity profile ellipticity for microstructural control during metal additive manufacturing," *Acta Materialia,* vol. 128, pp. 197-206, 2017, doi: 10.1016/j.actamat.2017.02.025.

[201] D. H. St John, S. D. McDonald, M. J. Bermingham, S. Mereddy, A. Prasad, and M. Dargusch, "The Challenges Associated with the Formation of Equiaxed Grains during Additive Manufacturing of Titanium Alloys," *Key Engineering Materials,* vol. 770, pp. 155-164, 2018, doi: 10.4028/www.scientific.net/KEM.770.155.

[202] DigitalAlloys. "Energy Consumption in Metal Additive Manufacturing." https://www.digitalalloys.com/blog/energy-consumption-metal-additive-manufacturing/ (accessed November, 26th, 2020).

[203] J. Liao and D. R. Cooper, "The Environmental Impacts of Metal Powder Bed Additive Manufacturing," *Journal of Manufacturing Science and Engineering,* vol. 143, no. 3, 2020.

[204] AMPower, "Metal Additive Manufacturing Report 2019," 2019. [Online]. Available: https://additive-manufacturing-report.com/additive-manufacturing-technology

[205] K. P. Hapgood, J. D. Litster, S. R. Biggs, and T. Howes, "Drop penetration into porous powder beds," *Journal of Colloid Interface Science,* vol. 253, no. 2, pp. 353-366, 2002.

[206] T. Nguyen, W. Shen, and K. Hapgood, "Drop penetration time in heterogeneous powder beds," *Chemical Engineering Science,* vol. 64, no. 24, pp. 5210-5221, 2009, doi: 10.1016/j.ces.2009.08.038.

[207] M. Ziaee, E. M. Tridas, and N. B. Crane, "Binder-Jet Printing of Fine Stainless Steel Powder with Varied Final Density," *Jom,* vol. 69, no. 3, pp. 592-596, 2016, doi: 10.1007/s11837-016-2177-6.

[208] T. Do, T. J. Bauder, H. Suen, K. Rego, J. Yeom, and P. Kwon, "Additively Manufactured Full-Density Stainless Steel 316L With Binder Jet Printing," in *ASME 2018 13th International Manufacturing Science and Engineering Conference*, 2018: American Society of Mechanical Engineers, pp. V001T01A017-V001T01A017.

[209] S. Kolosov, G. Vansteenkiste, N. Boudeau, J.-C. Gelin, and E. Boillat, "Homogeneity aspects in selective laser sintering (SLS)," *Journal of materials processing technology,* vol. 177, no. 1-3, pp. 348-351, 2006.

[210] A. Budding and T. H. J. Vaneker, "New Strategies for Powder Compaction in Powder-based Rapid Prototyping Techniques," *Procedia CIRP,* vol. 6, pp. 527-532, 2013, doi: 10.1016/j.procir.2013.03.100.

[211] H. Miyanaji, K. M. Rahman, M. Da, and C. B. Williams, "Effect of fine powder particles on quality of binder jetting parts," *Additive Manufacturing,* vol. 36, p. 101587, 2020.

[212] S. J. Lombardo and Z. Feng, "Analytic method for the minimum time for binder removal from three-dimensional porous green bodies," *Journal of materials research,* vol. 18, no. 11, pp. 2717-2723, 2003.

[213] K. Wang *et al.*, "Study on defect-free debinding green body of ceramic formed by DLP technology," *Ceramics International,* vol. 46, no. 2, pp. 2438-2446, 2020.

[214] Y. Wang and Y. F. Zhao, "Investigation of Sintering Shrinkage in Binder Jetting Additive Manufacturing Process," *Procedia Manufacturing,* vol. 10, pp. 779-790, 2017, doi: 10.1016/j.promfg.2017.07.077.

APPENDIX A SUPLEMENTARY LITTERATURE REVIEW

A.1 Families of metallic AM

There are seven families of AM processes [4, 5, 14]: vat photopolymerization, directed energy deposition, powder bed fusion (PBF), material extrusion, material jetting, sheet lamination and BJ. Although 3D printing of metals is principally done with PBF, directed energy deposition, BJ and Sheet lamination [21], techniques of all seven families can print metals [5].

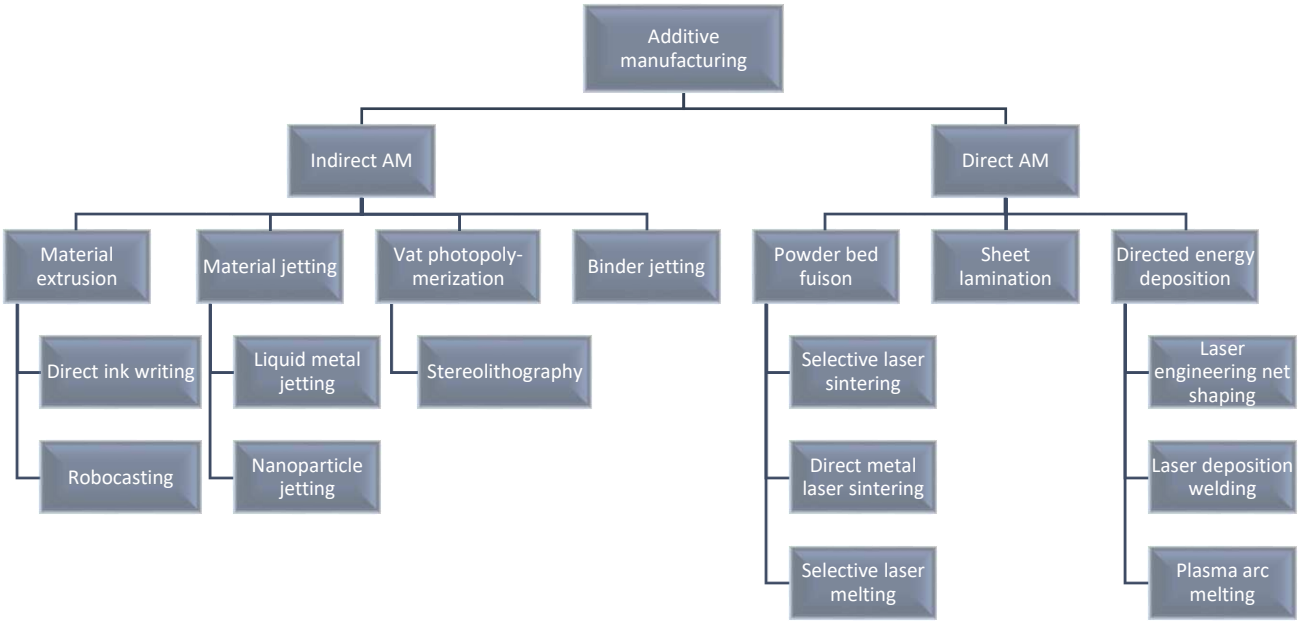

Figure A.1 Metallic AM families

AM techniques can be classified as direct or indirect methods (Figure A.1). Direct methods use lasers or electron beams to directly sinter or melt metallic powder or wires in a layer-by-layer way. Indirect methods use a binder to hold together and carry metal in a powder, nanoparticle or liquid form while successive layers are being printed. Thus, all indirect methods produce green bodies that must be debound and sintered (Figure 1.2) to obtain a pure metallic piece.

A. 1.1 Indirect AM methods

A.1.1.1 Vat photopolymerization

Vat photopolymerization is mostly used for polymer printing and encompasses all the techniques that use light to selectively polymerize a prepolymer in a liquid state through the photodegradation of an initiator [183]. The speed of these techniques is controlled by the movement of the light and the rate of the curing reaction. The resolution is determined by the wavelength of the light beam. For this reason, VP can print at high speeds and high resolutions [183]. Metallic and ceramic 3D printing can be achieved if a metal powder or liquid is added to the photocurable resin [184] (Figure A.2). However, the quantity of filler must be low (30-60 vol % [183-185]) to avoid interference with the photochemical process: the filler can absorb and scatter the light, ruining the print resolution [184]. Additionally, the powder size must be small enough to form stable suspensions in the resin tank. Otherwise, the powder will sediment [18]. Therefore, the final piece in this process is a green body with a high binder concentration. Generally, as the binder content in a green body increases, the debinding and sintering process becomes more difficult to accomplish and leave more carbon residue on the final part, which leads to high-porosity pieces with low mechanical properties. Consequently, this technique is rarely used for metallic 3D printing and is still under development [18, 21, 183].

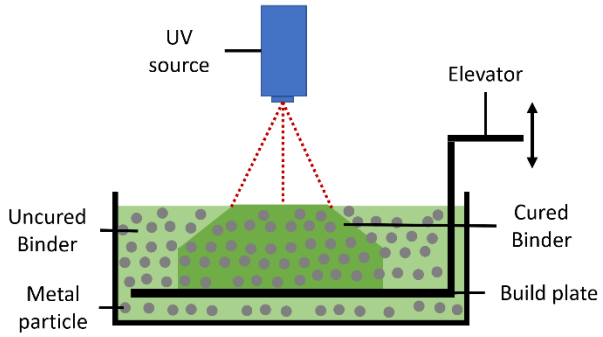

Figure A.2 Vat photopolymerization system schematic.

A.1.1.2 Material extrusion

In the same line of thoughts, material extrusion uses a mixture of metallic powder and a polymeric matrix as feedstock, shaped as a rod or wire. The rod is melted during extrusion and solidified as it reaches a surface [186, 187] (Figure A.3). It is basically the same principle as fused

deposition modeling, the most well-known AM process, widely used for rapid prototyping with polymers. However, the technique is called direct ink-writing or robocasting when it is used to print metals or ceramics. The solid loads of the slurries vary between 50 vol. % and 93 vol %, depending on the powder material and quality [186, 187]. Again, since large quantities of polymer are present in the final green body, the resulting pieces are difficult to debind and sinter [186, 188]. Conversely, this is one of the lower-cost techniques [188]. It is thus mostly used for cost-effective metal prototyping [188].

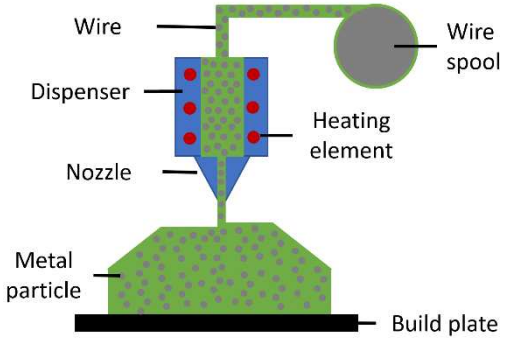

Figure A.3 Material extrusion system schematic.

A.1.1.3 Material jetting

Material jetting encompasses the techniques that use an inkjet technology to jet liquid material on a building platform and solidify it as it touches the surface. In most cases, a photocurable resin is printed and simultaneously cured with UV light [5, 7] (Figure A.4). In this family of techniques, one can also print metals by using a resin with a metallic filler, though the same drawbacks as for vat photopolymerization and material extrusion apply to this method due to the high concentration of polymer on the green bodies: low mechanical properties and high porosities [7]. However, low-melting-point metals can directly be printed with a technique called liquid metal jetting (LMJ) and the final properties of those parts are similar to those obtained in TM [189]. Additionally, a technique called nano particle jetting, allows users to print metals with a special ink that contains metallic nanoparticles [190]. These particles can be melted at temperatures as low as 150 °C. If the building chamber, the area where the pieces are printed, is maintained at that temperature, the nanoparticles will partially melt as they are deposited, and the solvent will be evaporated. To obtain the desired properties, the piece can be further treated in an oven to remove any remaining porosity [5]. The main advantages of this AM family are high

resolution (nano-scale printing) and simple adaptability to multi-material printing: one can simply add more printheads to print different inks [5, 191]. On the other hand, the material choices are low, handling nanoparticles can increase health risks, and nanoparticle inks are expensive [5, 191]. For these reasons, metal material jetting printing is primarily used in the fabrication of low volume parts and it is particularly interesting for circuit printing for the electronics industry [190].

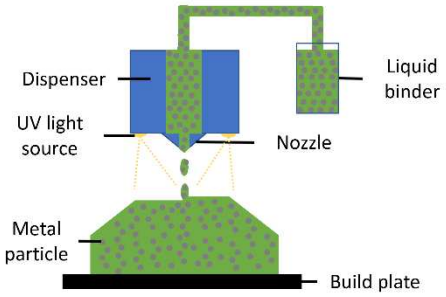

Figure A.4 Material jetting system schematic.

A.1.1.4 Binder jetting (BJ)

The most popular indirect technique for metallic AM is BJ [21]. Similar to the other techniques of this category, it uses a binder to hold powder particles together to shape a green body. However, this technique does not use a mixture of those two components as a feedstock. The binder is used as an ink and it is printed on successive layers of powder (Figure 1.1). The resolution of this technique is dictated by the droplet size, powder size and powder bed thickness, making it a high-resolution AM system [15, 192]. Also, this technique does not need any supporting structure, as opposed to all other AM families [5]. In fact, these structures are generally used to avoid breakage of overhanging parts. In BJ, the piece is already supported by the surrounding lose powder. This means that this technique offers more design freedom to the user. Besides this, the main reasons why this technique is more suitable for metallic 3D printing than other indirect techniques are the larger printing volumes, the higher printing speeds and the lower final binder concentrations in the green bodies (1-10 vol %) [4, 6, 34]. The last point is particularly important as it allows BJ to produce pieces with lower porosities and higher mechanical properties. Consequently, BJ allows to produce higher quality metallic parts and larger production volumes than other indirect AM techniques and it is suitable to compete with the most popular direct techniques [4, 10]. BJ has found its place on almost every industry (automobile, aerospace,

biomedicine, foundry, jewellery, etc), mainly for high complexity, high production volume applications, where moderate mechanical properties are needed [5, 15, 193].

A.1.2 Direct AM methods

A.1.2.1 Sheet lamination

Sheet lamination is a direct AM method that consists of ultrasonic welding of successive sheets of metallic foil. For this, a roller called a "sonotrode" rolls over the building area, applying a moderate mechanical pressure on the foils while vibrating at a high ultrasonic frequency. The vibrations are transmitted to the sheets' interfacial area promoting the sheets' bonding through molecular diffusion. Afterwards, using a milling process, the sheet is shaped according to the 3D model. The foil can also be shaped before welding with any precision cutting tool, such as a laser beam [14, 194] (Figure A.5). This technique is often used for metallic 3D printing since it allows the building of large volumes faster than other techniques, with less expensive raw material [7, 194]. However, due to its subtractive nature, it produces more waste than other AM techniques and does not allow the same geometric freedom, losing two key advantages of AM. Also, the bonds between sheets are weak and cause interface delamination, which gives anisotropic properties to the final pieces. Therefore, this technique is mostly used for prototyping and production of cores for casting, layered composite materials and decorative products [5, 194]. It is thus, the most cost-effective metallic AM technique for simple geometries, large production volumes and applications where high mechanical properties are not desired.

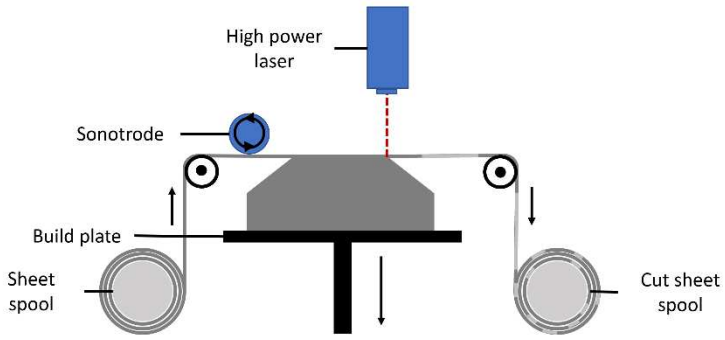

Figure A.5 Sheet lamination system schematic.

A. 1.2.2 Directed energy deposition

Directed energy deposition methods encompass all the techniques that use a high energy electron or laser beams to weld metallic powder or wires that are directly feed under the beam (Figure A.6 a)). In fact, the energy creates a melt pool where the previous layer and the new feedstock are melted and mixed before being solidified, building a new layer. Some examples of this AM family are laser engineered net shaping, laser deposition welding and plasma arc melting [6, 195]. These techniques are mostly used for high volume parts, as they allow the user to print several cubic meters thanks to a 5-axis building system, instead of the regular 3-axis one of other AM techniques [194]. That multi-axis system allows to avoid the use of supporting structures and removes the limitation of building on successive horizontal layers, as structures can be rotated as they are printed [21, 196] (Figure A.6 b)). The main advantages of this technique are that it can be used for part reparation and cladding deposition [6], as it can start building from an existing piece, and it produces fully dense structures [196]. The main drawbacks are the limited resolution (0.5 - 1 mm) and surface finish [4, 5, 21]. Also, residual stresses are left on the pieces due to the cyclic solid liquid transformations of each layer [197, 198]. Compared to PBF, directed energy deposition has higher deposition rates, but it consumes more energy [6]. It is, in fact, the most energy-intensive member of all the AM families. These are thus key techniques for repair cladding deposition and any other large volume part application, where high accuracy is not needed [4].

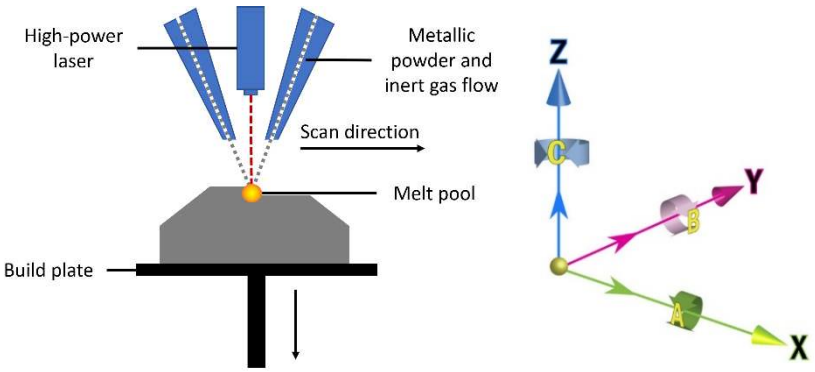

Figure A.6 Directed energy deposition: a) system schematic; b) multi-axis system schematic (adapted from [199]).

A. 1.2.3 Powder bed fusion (PBF)

Finally, PBF, the most used AM family for metallic printing [21], consists of directly melting or sintering specific regions of a powder bed. As in BJ, this technique generally uses the

two-piston system and a counter-rotating roller to deposit the powder layers [198] (Figure A.7). The most common PBF systems are selective laser melting, selective laser sintering and direct metal laser sintering. These techniques give final pieces that are close to full density and show similar mechanical properties to metal pieces made with TM [194]. However, as for direct energy deposition systems, the properties of the pieces are anisotropic and the direction of the anisotropy depends on the printing direction [194]. In fact, PBF parts show a columnar epitaxial grain texture [200]. These columnar grains are several build layers high and are intrinsic to the kinetics of the melt pool and its rapid solidification [200]. Although, this can be an advantage, as the technique could permit to tailor the final piece's grain structure to have better properties than those obtained in TM, it has only been accomplished with certain materials and is still a an active area of research [201]. One important drawback of this AM family of techniques is the need of a controlled printing environment. The printing process must be performed in an inert environment to avoid any oxidation of the powder. Additionally, the build plate must be held between 200 °C to 500 °C to reduce the cooling rate of the printed layers and thusly release residual stresses [10, 194]. Despite these disadvantages, PBF techniques possess the best combination of material versatility, speed, resolution and mechanical properties [10]. This is why they show the most widespread industrial use.

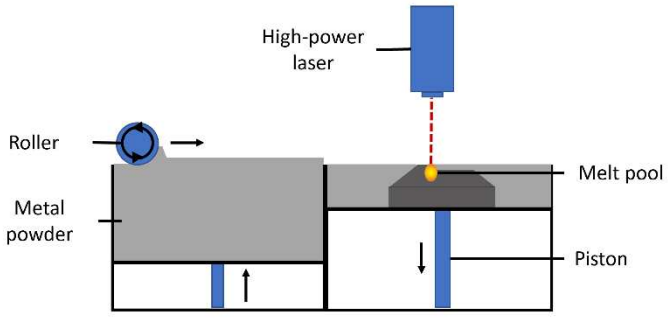

Figure A.7 Powder bed fusion system schematic.

A. 1.3 Metallic AM families: a comparison

As previously stated, sheet lamination, PBF, BJ and directed energy deposition are the most important metallic 3D printing techniques as they have key applications where the other technologies cannot compete. However, there are cases were several of them could be used [10].

Thus, the best AM process for a given application depends on the cost, material, accuracy, final needed properties and lead time [10]. Table A.1 and

Table A.2 present a summary of the main characteristics and applications of the different AM families.

Table A.1 Summary of characteristics of the 7 AM families.

AM family	Build volume	Mechanical properties	Resolution	Speed	Materials choice	Other characteristics
VP	Medium	Low	Highest	High	Limited	Only for photocurable binders
ME	Medium	Low	Medium	Lowest	Broad	Lowest prices
MJ	Small	Low	High	Highest	Limited	This family encompass Indirect and direct AM techniques
BJ	High	Medium	High	High	Broadest	Multi-color printing
SL	High	Medium	Low	Medium	Broad	Limited geometrical freedom
DED	Largest	High	Lowest	High	Broad	Columnar grain growth and residual stress on final parts
PBF	small	High	High	Medium	Broad	Columnar grain growth and residual stress on final parts

Table A.2 Main applications of the 7 AM families

AM family	Metallic AM application
VP	• Metallic prototyping
ME	• Metallic prototyping
MJ	• Circuitry printing • Nanoscale printing
BJ	• Core and moulds • Decorative products • Visual prototyping • High volume, high detail production of non-structural components
SL	• Cores of casting • Layered composite materials • Decorative products
DED	• Reparation • Cladding deposition • Large volume structural and non-structural components
PBF	• Small volume, high detail production of structural and non-structural components

A.1.3.1 Comparing PBF and BJ metallic AM techniques

Compared to PBF, BJ's main drawback is related to the final piece properties. PBF creates more dense parts and it even offers the possibility to tune the properties to make them better than in traditional manufacturing [194]. However, BJ possesses many advantages over PBF. Not only it allows the user to print with higher resolution, it allows him to print over larger volumes with faster rates [6, 194]. This means that for the same piece size, BJ can produce more parts per batch in less time. In fact, the printing process in BJ is much faster than in PBF, as one layer can be printed in a matter of seconds [194]. However, due to the debinding and sintering steps, the two techniques possess similar production speeds, if the larger production volume of BJ is not considered. Additionally, BJ consumes much less energy as it does not require a high energy source, nor a controlled printing environment [6, 202, 203]. According to Liao and Cooper [203], BJ requires 99 MJ/kg to produce steel parts. On the other hand PBF uses between 83 and 588

MJ/kg depending on the material to be printed. As can be noticed from those estimations, the values are sensitive to printing materials and process variations. Another example is the calculations of the company DigitalAlloys. They estimate that BJ consumes 1000.8 MJ/kg contrary to PBF that needs 1292.4 MJ/kg to produce titanium pieces [202].

As previously exposed, PBF techniques need an inert atmosphere during printing to avoid oxygen contamination of the metallic particles [194]. This is also true in BJ for the sintering step. However, during the printing process, BJ occurs at ambient temperature and atmosphere. This gives a considerable advantage to this technique, as it permits the printing of a broader spectrum of materials. In fact, BJ allows the printing of refractory and high reflectivity materials that are difficult to print with a high power beam [5, 23]. Also, brittle materials that can deform or break due to residual stresses in PBF are more easily printed with BJ [10]. Finally, BJ offers a larger spectrum of final products, depending on the desired application: green body, infiltrated green body, infiltrated semi-sintered body, sintered body and infiltrated sintered body. It also offers the possibility of fabricating more types of composite material, as different kinds of powder can be mixed in the powder bed and a broad spectrum of polymers and nanoparticles can be added to the binder. Due to all its advantages, BJ is a very promising technique that is projected to attain a widespread industrial use in less than 2 years, according to its AM maturity index [204].

A.2 Powder properties and bed deposition

The most important factors around the powder bed are the speed of deposition, to print with faster rates, and the homogeneity of the bed, to obtain consistent green and final properties. The properties of the powder bed depend of 3 parameters: layer height, layer compaction and powder properties. The layer height and compaction are directly linked to the resolution, as the layer thickness sets the number of layers forming a piece and compaction influences the binder penetration into the powder bed. In fact, binder penetration is influenced by the drop volume V_0, the viscosity μ, the surface tension γ , the dynamic contact angle θ_d and the powder packing density [25, 205, 206]. Powder packing also impacts the density of the green bodies. With higher packing densities, one obtains higher green densities and thusly, high sintered densities [15, 42, 207].

On their side, powder properties are shape and size distribution. These two characteristics limit the layer parameters, as they play a major role on the flowability and the maximum possible

packing of the powder [34, 208]. Typical particle sizes are between 0.2 and 200 μm [15]. Smaller powders usually lead to higher quality products because they form higher density bodies and they sinter at lower temperatures. However, as particle size decreases, inter-particle interactions and sensitivity to moisture become significant, witch results in non-uniformities on the powder bed [34]. To overcome this, very fine powder beds (~ 1 μm) must be deposited as slurries [36].

There are various models to predict the powder packing in BJ and PBF, but most of them consider the powder to be monosized and spherical, which is rarely the case [34]. In fact, the use of a mix of two powders with different size distributions is gaining popularity. It allows to benefit from the flowability of the coarser particles and the reactivity and density of the smaller ones. The fine particles fill the voids between the larger particles, which results in higher green densities [42]. With respect to the particles' shape, ideally, it should be as spherical as possible with a smooth surface. This ameliorates the powder flowability, as it reduces the friction between particles. However, the impact of the particle shape is less important than that of the particle size [31].

Doctor blade is the classical and simpler way to deposit a powder bed. It consists on a sweeping action on the powder by a blade (Figure A.8 a). Over the years, the shape of the blade has been optimised and it can be used in a vibrating mode to obtain higher compaction. However, the only real parameters of this method are the layer height and the blade speed, as can be seen in Figure A.8 a). This method is not fitted for the deposition of particles smaller than 5μm and the quality of the layers are not high for powders smaller than 20 μm [209]. Also, the defects of the blade are transmitted to the powder bed [210].

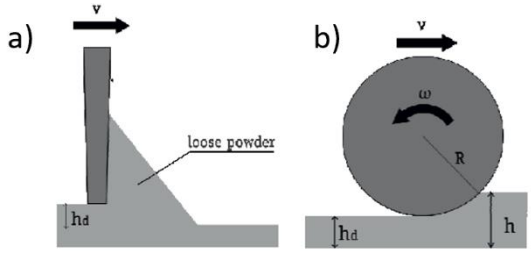

Figure A.8 Schematic representation of a) a doctor blade and b) a roller [210]

On the other hand, the counter-rotation roller deposition is the most common method (Figure A.8 b). As opposed to the doctor blade technique where the powder is simply swept, the

roller imposes a pressure as well as a shear stress on the powder [85]. As a result, the powder gets compacted in the roller gap. The main parameters of this method are speed, powder layer thickness, roller radius, roller contact pressure, roller angle and friction between roller and powder and between powder and powder. It should be noticed that the roller could also be rotated in the forward direction, but it leads to crater formation. In the forward mode, more pressure is applied, which makes the powder stick to the roller [210].

Recently, a hopper has been added to BJ systems and is being used in combination with the counter-rotating roller (Figure A.9) [38, 211]. The hopper is hanged on top of the printing zone and deposits the powder by letting it fall. Then, a roller passes trough the surface to smoothen the area. This allows to deposit uniform layers of very fine powders, as the interparticle interactions are countered by the ultrasonic vibration of the hopper. It also allows to print faster because there is no need to stop the printer to reload powder into the system.

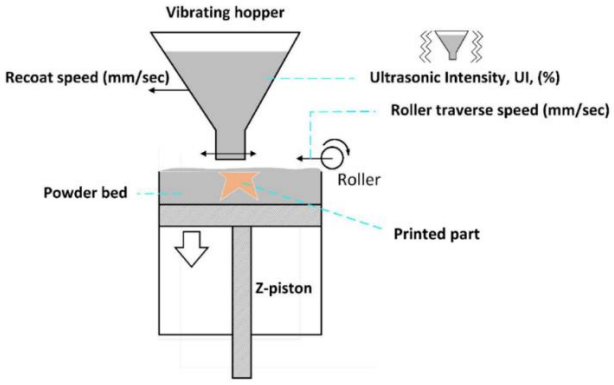

Figure A.9 Powder deposition mechanism with a hopper [211].

A.3 Debinding and Sintering

Although debinding and sintering are very different process they share the same parameters: heating-cooling rates, temperature, time and atmosphere. The goal of debinding is to remove all the binder without leaving any residue on the powder and without creating any harmful products for the health and the environment while maintaining the piece's integrity [212]. Therefore, debinding is closely related to the binder selection. Thermogravimetric analysis coupled with infrared spectroscopy experiments can be accomplished to study the behavior of the binder candidates with respect to temperature and analyse the pyrolysis products under different

atmospheres [17, 42, 192, 213]. Additionally, differential scanning calorimetry experiments show the temperatures at which the binder goes trough the liquid and gas transformations. These experiments are useful to see if the binder decomposition is compatible with the powder material of interest.

On its side, sintering's goal is to fully densify the piece while resulting in the desired final aspect ratio and mechanical properties. Sintering takes place due to the necessity of the system to reduce its surface energy [19, 38]. The higher temperature allows the atoms to move and since the atoms at the surface have pendant bonds (incomplete bonds) that increase their energy, they tend to migrate. This is called the "global" driving sintering mechanism: surface energy reduction. There is also a "local" driving mechanism. It is related to the stability of low curvature surfaces with respect to high curvature ones. The atoms in the high curvature regions, convex particle surfaces, will move towards the lower curvature regions such as necking regions or larger particles.

This process is favored, if the sintering time and temperature are increased [214]. However, longer times result in coarser microstructure, which means poor final mechanical properties [10]. Also, good final density requires an initial green density greater than 50 % [34]. In the presence of binder residues, sintering will cause the mixing of the impurities with the pure metal, causing a change in the composition of the material [34].

APPENDIX B CERTIFICATE OF ANALYSIS OF THE METALIC POWDER

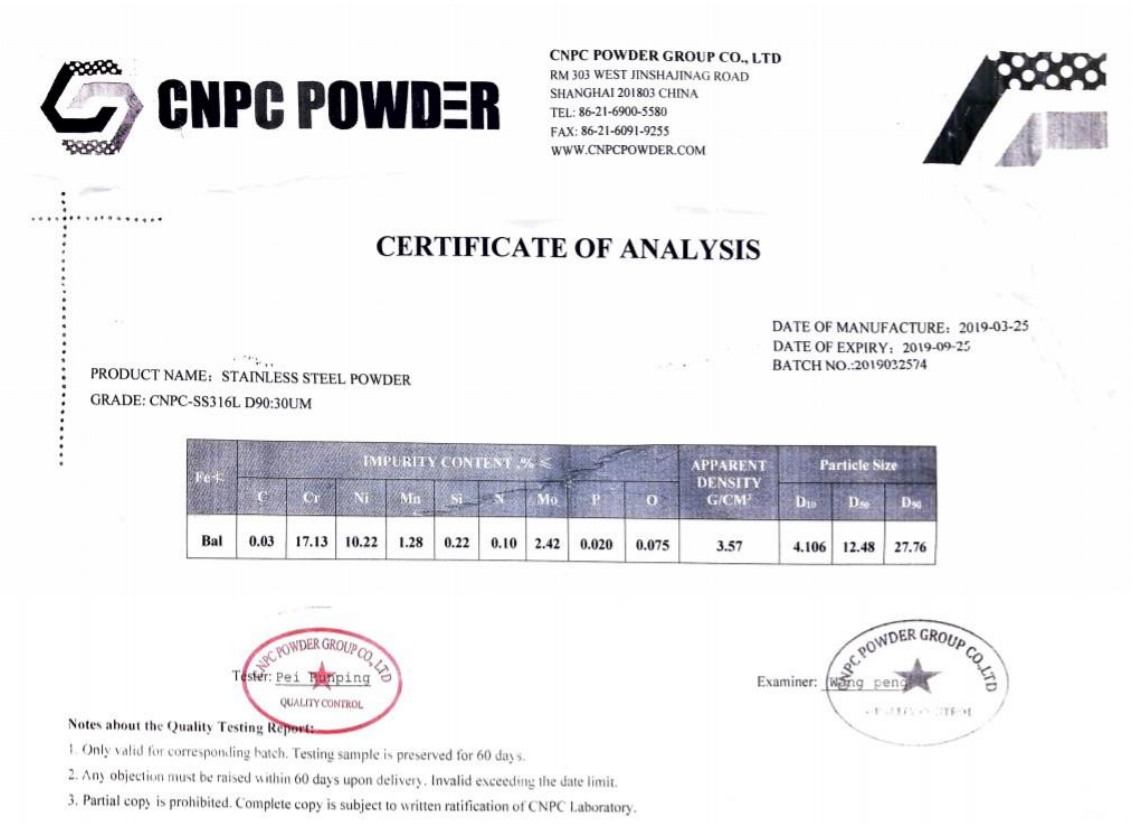

CNPC POWDER

CNPC POWDER GROUP CO., LTD
RM 303 WEST JINSHAJINAG ROAD
SHANGHAI 201803 CHINA
TEL: 86-21-6900-5580
FAX: 86-21-6091-9255
WWW.CNPCPOWDER.COM

CERTIFICATE OF ANALYSIS

DATE OF MANUFACTURE: 2019-03-25
DATE OF EXPIRY: 2019-09-25
BATCH NO.:2019032574

PRODUCT NAME: STAINLESS STEEL POWDER
GRADE: CNPC-SS316L D90:30UM

Fe	IMPURITY CONTENT ,% ≤									APPARENT DENSITY G/CM³	Particle Size		
	C	Cr	Ni	Mn	Si	N	Mo	P	O		D_{10}	D_{50}	D_{90}
Bal	0.03	17.13	10.22	1.28	0.22	0.10	2.42	0.020	0.075	3.57	4.106	12.48	27.76

Tester: Pei Pumping
CNPC POWDER GROUP CO.,LTD QUALITY CONTROL

Examiner: Wang peng
CNPC POWDER GROUP CO.,LTD

Notes about the Quality Testing Report:

1. Only valid for corresponding batch. Testing sample is preserved for 60 days.
2. Any objection must be raised within 60 days upon delivery. Invalid exceeding the date limit.
3. Partial copy is prohibited. Complete copy is subject to written ratification of CNPC Laboratory.

Figure B.1 Certificate of analysis of the 316L powder.

APPENDIX C BINDER IDENTIFICATION IN SEM IMAGES

In Figure C.1 one can confirm that the black phase in the SEM images is polymer, as it is mainly composed of carbon (red image). With the help of image analysis, the presence of binder is more easily identifiable in the micrographs.

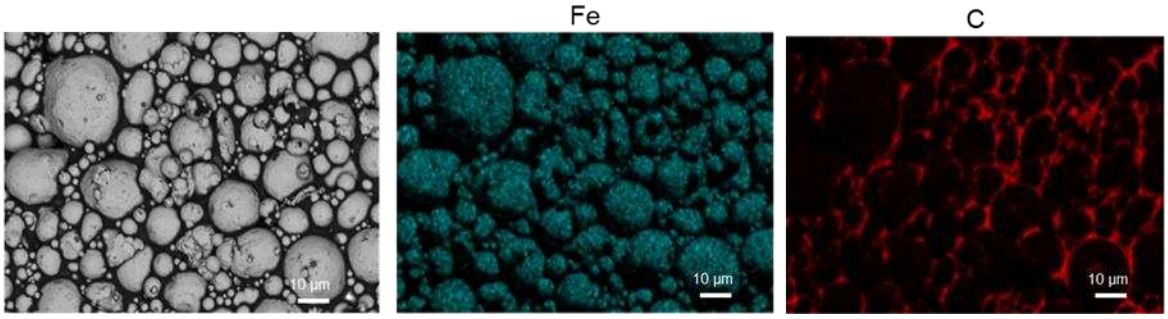

Figure C.1 SEM and EDX images of a saturated PVA green body.

Ilastik is an open-source image segmentation tool that uses machine learning to treat images. It was used in combination with ImageJ to evaluate the percentage of binder on the SEM images. The process is illustrated on Figure C.2. First, three images are used to train the random forest algorithm of Ilastik. Then it produces a prediction on the images used for the training process as well as for new images. From Ilastik, one gets an image where the binder is clearly identified by pixel segmentation. Finally, this image is treated with ImageJ to obtain the pixel % of the image occupied by the Binder.

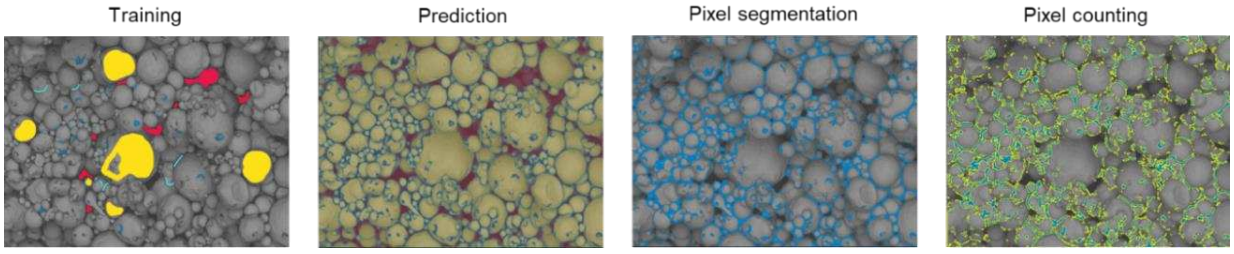

Figure C.2 Ilastik and ImageJ image treatment steps for the SEM images of green bodies.

Using this method the images of Figure C.3 were analysed. Thanks to the pixel segmentation, it is easer to see the difference between the images of samples with different concentrations. As expected, the pixel count increases with concentration. It can serve as a quantitative characterisation of binder concentration in the green bodies.

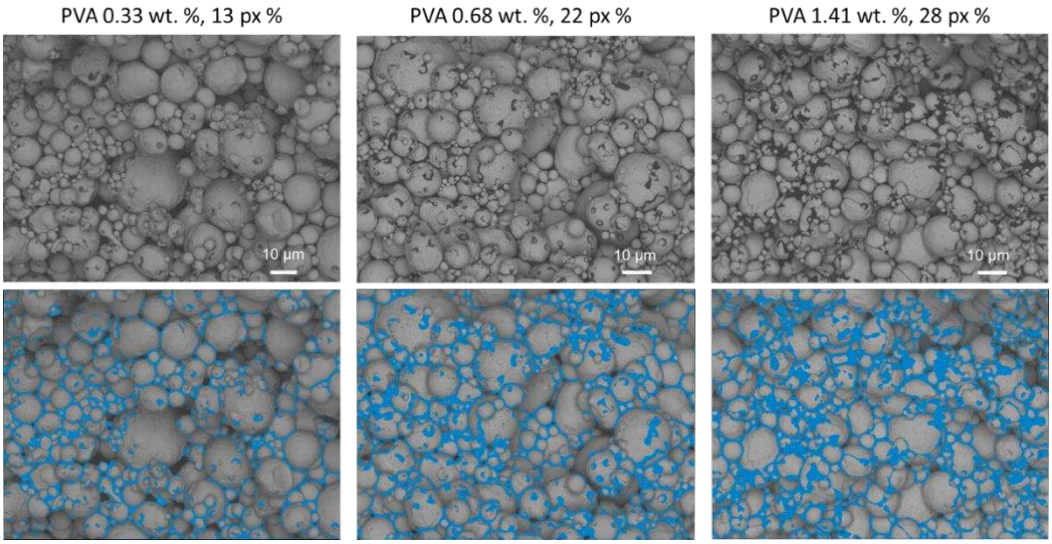

Figure C.3 Binder area pixel counting. Top: BSE SEM images of PVA green bodies with different concentrations (dry binder mass/green body mass). Bottom: binder pixel segregation results from Ilastik.

APPENDIX D BINDER INTERONNECTIONS

Figure D.1 presents the extent of the binder interconnections in PVA green bodies. The binder slim lines go through several particles.

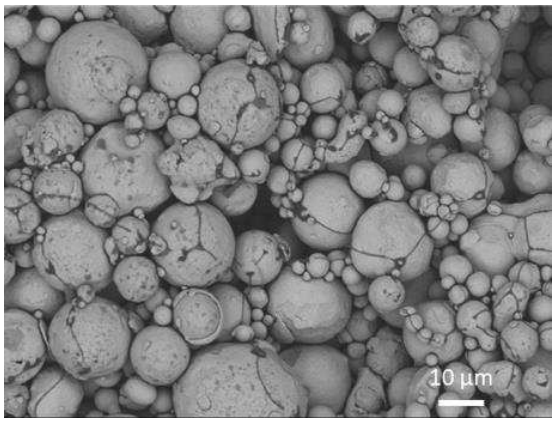

Figure D.1 Low magnification SEM BSE image of a 0.68 wt. % (dry binder mass/green body mass) PVA green body.

APPENDIX E EFFECT OF MOLECULAR WEIGHT: SEM IMAGES

According to Figure E.1, there are not significant variations between the PVP samples made with different molecular weights. The binder distribution is the same in the three cases (pendular regime). The only difference is that the binder marks on the 360 kg/mol are darker. In fact, the polymer chains are much larger, so they attenuate more the signal.

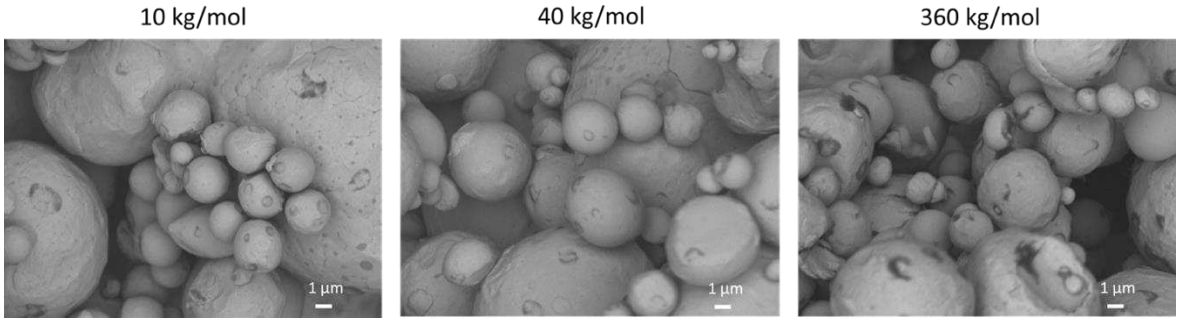

Figure E.1 BSE SEM images of green bodies made with different PVP 5 wt. % binders with different molecular weights.

APPENDIX F FILL FACTOR OF PVA SAMPLES WITH INK

The fill factor increase with concentration can be observed in Figure F.1. Similar to the case without ink, the binder occupies more interstitial space as the binder concentration rises.

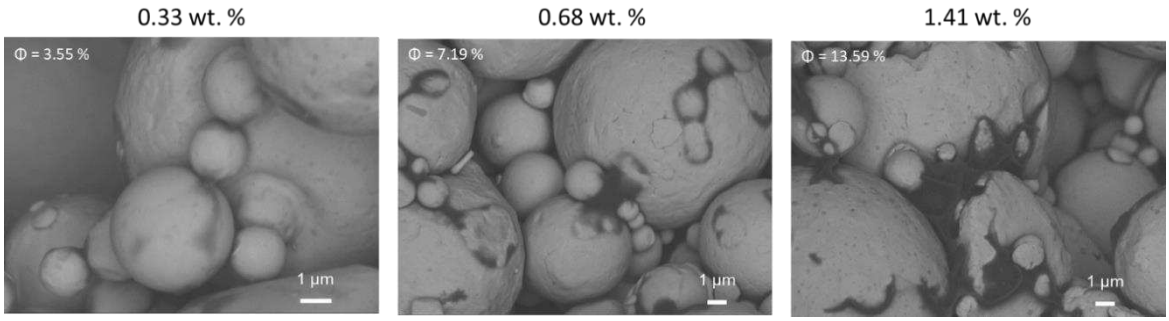

Figure F.1 BSE SEM images of PVA green bodies with ink and increasing fill factor. The concentrations indicated in the top of the images are dry binder mass/green body mass ratios.

APPENDIX G EFFECT OF HYDROLYSIS PERCENTAGE

PVA 13-23k (87-89 % hydrolyzed) and PVA 13-23k (98 % hydrolyzed) were used to assess the impact of the hydrolysis percentage of the polymer on the green strength. The two polymers were purchased at Sigma Aldrich and were used as received. Figure G.1 shows that higher hydrolysis percentages result in higher strengths. Visually, PVA 98% hydrolyzed granules are opaquer and take longer to dissolve. This suggests that the higher hydrolysis PVA is more crystalline, therefore it is stronger [131]. This means that a polymer with higher crystallinity will give better strength to the green bodies.

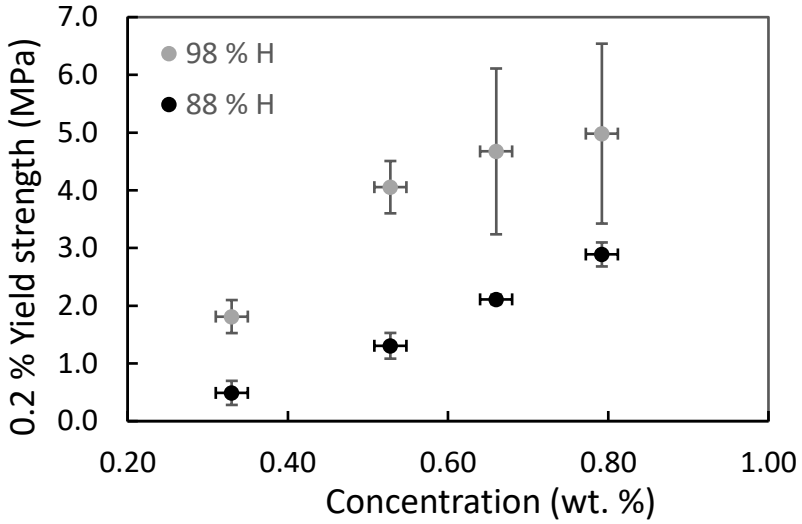

Figure G.1 0.2 % yield strength of PVA green bodies for two hydrolysis percentages.